



Improved Dynamic Load Modeling Using Power System Measurements for Enhanced Transmission and Distribution System Operation and Planning

Final Project Report

S-80

Power Systems Engineering Research Center
*Empowering Minds to Engineer
the Future Electric Energy System*



Improved Dynamic Load Modeling Using Power System Measurements for Enhanced Transmission and Distribution System Operation and Planning

Final Project Report

Project Team

Vijay Vittal, Project Leader
Arizona State University

Le Xie
Texas A&M University

Graduate Students

Sameer Nekkhalapu
Arizona State University

Xinbo Geng
Athindra Venkatraman
Texas A&M University

PSERC Publication 21-04

February 2021

For information about this project, contact:

Vijay Vittal
Arizona State University
School of Electrical, Computer and Energy Engineering
P.O. Box 875706
Tempe, AZ, 85287-5706
Phone: 480-965-1879
Fax: 480-965-0745
Email: vijay.vittal@asu.edu

Power Systems Engineering Research Center

The Power Systems Engineering Research Center (PSERC) is a multi-university Center conducting research on challenges facing the electric power industry and educating the next generation of power engineers. More information about PSERC can be found at the Center's website: <http://www.pserc.org>.

For additional information, contact:

Power Systems Engineering Research Center
Arizona State University
527 Engineering Research Center
Tempe, Arizona 85287-5706
Phone: 480-965-1643
Fax: 480-727-2052

Notice Concerning Copyright Material

PSERC members are given permission to copy without fee all or part of this publication for internal use if appropriate attribution is given to this document as the source material. This report is available for downloading from the PSERC website.

© 2021 Arizona State University. All rights reserved.

Acknowledgements

We acknowledge the technical feedback from project advisors. We thank Professor Leigh Tesfatsion for her insightful feedback to Chapter 3 of Part 2.

Executive Summary

The project uses point on wave measurements made in power system following disturbances of different types and severity to first determine accurate three-phase load composition along distribution feeders. Based on the detailed three-phase load composition characterization obtained, more accurate load compositions for conducting positive-sequence time domain simulations will be developed. The operational and planning benefits of more detailed load compositions in making electric utilities more competitive will be quantitatively evaluated.

This project is collaboration between Arizona State University and Texas A&M University. The project report is composed of contributions from both universities. The first part of this project, title “Load Synthesis in Distribution Feeders Using Point on Wave Measurements”, is presented from Chapter 1 through Chapter 5. The second part, title “Enhanced Transmission and Distribution System Operation and Planning with Improved Dynamic Load Modeling”, demonstrates the benefits and applications of the advanced load models established in the first part of this project.

With the increasing penetration of renewables in the distribution systems, the need to address the challenges of load modeling is becoming essential. Some of these challenges include obtaining an accurate and a realistic representation of the aggregated load model parameters and the load composition to represent the feeder and load models in grid studies. With an emphasis on tackling these issues in the topic of load modeling, this report presents the following intermediary steps in developing accurate load models:

1. Synthesis of a three-phase standard feeder and load model using the measured voltages and currents, for events such as faults and feeder pickup cases, obtained at the head of the feeder.
2. Synthesis of more accurate three-phase feeder and load models at different substations using the standard feeder and load model developed in Step 1.
3. Investigated issues relate to motor stalling phenomenon in positive sequence software packages (such as PSLF) and proposed an analytical approach to estimate the motor stalling in PSLF.

In the first phase of this project, a standard feeder and load model had been synthesized by capturing the current transients when three-phase voltage measurements (obtained from a local electric utility) are played-in as input to the synthesized model. The comparison between the measured currents and the simulated currents obtained using an electromagnetic transient analysis software (PSCAD) are made at the head of the designed feeder. The synthesized load model has a load composition which includes impedance loads, single-phase induction motor loads and three-phase induction motor loads. The parameters of the motor models are adjusted to obtain a good correspondence between measured three-phase currents and simulated current responses at the head of the feeder when subjected to events under which measurements were obtained on the feeder. These events include faults which occurred upstream of the feeder at a higher voltage level and a feeder pickup event that occurred downstream from the head of the feeder. Two different

load compositions have been obtained for this feeder and load model, depending on the types of load present in the surrounding area (residential or industrial/commercial).

The second phase of this project develops a more systematic algorithmic approach to obtain better feeder and load model based on the substation it originates from and at different loading conditions (in summer and winter). The standard feeder and load model obtained from the first phase of this project is used as the starting point to apply the proposed algorithmic approach to obtain more accurate feeder and load models. Like the first phase of this project, both load parameters and load composition have been determined for these feeder and load models depending on their physical location and the nature of the load supported by these feeders.

In the third phase of this project, the impact of feeder and load modeling studies in positive sequence time domain simulation environments such as PSLF has been investigated. One of the feeder and load models obtained from the second phase of this project has been used to study the motor stalling phenomenon issues in PSLF. An analytical approach based on multi-variable linear regression has also been proposed in this work to estimate motor stalling in PSLF accurately.

In the remaining phase of this project, we study the enhanced transmission and distribution operations and planning due to improved dynamic load modeling. In particular, Chapter 1 of Part 2 studies the enhanced operation in distribution grid with more accurate three-phase load composition information. Chapter 2 of Part 2 presents an enhanced transmission operation by look-ahead coordination reactive power support devices. Chapter 3 of Part 2 proposes a new business model for the future distribution utilities by explicitly accounting for the “grid-friendliness” of individual customers.

This team is grateful for the encouragement and support received from the list of industry advisors. The PSERC staff members have also provided enormous support during the progress of this project.

Industry Advisors

Brian Keel	Salt River Project	brian.keel@srpnet.com
Mahendra Patel	EPRI	mpatel@epri.com
Anish Gaikwad	EPRI	agaikwad@epri.com
Bजारंग Agrawal	APS	bजारंग.agrawal@epri.com
Eugene Litvinov	ISO-NE	elitvinov@iso-ne.com
Jianzhong Tong	PJM	jianzhong.tong@pjm.com
Melvin Shoech	CenterPoint	melvin.shoech@centerpointenergy.com
Di Shi	GEIRI North America Inc.	di.shi@geirina.net
Xing Wang	Centrica	xing.wang@directenergy.com
Hung-Ming Chou	Dominion Energy	hung-ming.chou@dominionenergy.com
Anupam Thatte	MISO	athatte@misoenergy.org

Part I

Load Synthesis in Distribution Feeders Using Point on Wave Measurement

Vijay Vittal
Sameer Nekkhalapu, Graduate Student

Arizona State University

For information about this project, contact

Vijay Vittal
Arizona State University
School of Electrical, Computer, and Energy Engineering
P.O. BOX 875706
Tempe, AZ 85287-5706
Phone: 480-965-1879
Fax: 480-727-2052
Email: Vijay.Vittal@asu.edu

Power Systems Engineering Research Center

The Power Systems Engineering Research Center (PSERC) is a multi-university Center conducting research on challenges facing the electric power industry and educating the next generation of power engineers. More information about PSERC can be found at the Center's website: <http://www.pserc.org>.

For additional information, contact:

Power Systems Engineering Research Center
Arizona State University
527 Engineering Research Center
Tempe, Arizona 85287-5706
Phone: 480-965-1643
Fax: 480-727-2052

Notice Concerning Copyright Material

PSERC members are given permission to copy without fee all or part of this publication for internal use if appropriate attribution is given to this document as the source material. This report is available for downloading from the PSERC website.

© 2021 Arizona State University. All rights reserved.

Table of Contents

1. Introduction.....	1
1.1 Project Goals and Overview	1
1.2 Organization of the Report.....	2
2. Manual Tuning Method to Synthesize Feeder and Load Models	3
2.1 Introduction.....	3
2.2 Individual Components Configuration of the Feeder Models	3
2.2.1 Overhead Lines	5
2.2.2 Three-Phase Induction Motors.....	5
2.2.3 Single-Phase Induction Motors.....	6
2.2.4 Distribution Transformers.....	7
2.3 Case 1: Substation A Summer Event	7
2.3.1 Introduction and Case Setup	7
2.3.2 Load Composition.....	8
2.3.3 Parameter Sensitivity Analysis	10
2.3.4 Case 1: Results and discussion	16
2.4 Case 2: Substation A Winter Event	16
2.4.1 Introduction.....	16
2.4.2 Substation A Winter: Load composition.....	18
2.4.3 Substation A Winter: Critical Parameters and parameter sensitivity analysis.....	18
2.4.4 Substation A Winter: Results and Discussion	19
2.5 Case 3: Substation B Summer Event	20
2.5.1 Introduction.....	20
2.5.2 Critical Parameters of Distribution Transformers.....	22
2.5.3 Case 3: Load Composition.....	23
2.5.4 Results and Discussion	24
3. Algorithmic Approach to Synthesizing Feeder and Load Models.....	28
3.1 Introduction.....	28
3.2 Gauss-Newton Approach: Implementation.....	31
3.2.1 Objective Function.....	31
3.2.2 Jacobian, Step Length and Parameter Updates	31
3.2.3 Choosing Parameter Bounds.....	32

3.2.4 Implementing Parameter Bounds.....	34
3.2.5 Convergence Criterion.....	35
3.3 Results and Discussion	35
4. Positive Sequence Feeder and Load Models	43
4.1 Introduction.....	43
4.2 PSLF Simulations	43
4.2.1 Positive Sequence Voltage Generation.....	43
4.2.2 Feeder and Load Models in PSLF	46
4.3 Regression Model to Predict SPIM Stalling in PSLF.....	48
4.3.1 Step 1: Generate Random Test Cases in PSCAD.....	50
4.3.2 Step 2: Data extraction from PSCAD.....	51
4.3.3 Step 3: Positive sequence voltage generation in ‘Matlab’	52
4.3.4 Step 4: Data Generation in PSLF.....	52
4.3.5 Step 5: Training the Regression Model	54
4.3.6 Step 6: Regression Model Output Interpretation	54
4.3.7 Step 7: Testing results of the regression model	54
5. Conclusions and future work	56
5.1 Conclusions.....	56
5.2 Future Work.....	57
References.....	58

List of Figures

Figure 2.1 Feeder and Load Model used in Case 1, Case 2, Case 3, and Case 4	4
Figure 2.2 2 Load Torque Profile for SPIM [4].....	6
Figure 2.3 Case 1 RMS Three-Phase Voltage Profiles.....	8
Figure 2.4 POW Played-in Phase-A Voltage Measurement for Case 1	9
Figure 2.5 Simulation vs Actual System Representation.....	9
Figure 2.6 Phase A Faulted Current at Substation A for Case 1.....	11
Figure 2.7 Phase B Non-Faulted Current at Substation A for Case 1.....	12
Figure 2.8 Phase C Non-Faulted Current at Substation A for Case 1.....	12
Figure 2.9 SPIM Speeds at Three Different Segments Across the Feeder in Phase A.....	14
Figure 2.10 SPIM Speeds at Three Different Segments Across the Feeder in Phase B.....	15
Figure 2.11 SPIM Speeds at Three Different Segments Across the Feeder in Phase C.....	15
Figure 2.12 Phase A Current Comparison for Summer Case	16
Figure 2.13 Phase B Current Comparison for Summer Case	17
Figure 2.14 Phase C Current Comparison for Summer Case	17
Figure 2.15 Three-Phase RMS Voltage Profiles for Case 2	18
Figure 2.16 Phase A Current Comparison for Winter Case.....	19
Figure 2.17 Phase B Current Comparison for Winter Case.....	19
Figure 2.18 Phase C Current Comparison for Winter Case.....	20
Figure 2.19 Single Line Diagram of the Substation B Area.....	21
Figure 2.20 Three-Phase RMS Voltage profiles for Case 3	21
Figure 2.21 Transformer Knee Curve Characteristic [3].....	22
Figure 2.22 Phase-A Currents Comparison	25
Figure 2.23 Phase-B Currents Comparison	25
Figure 2.24 Phase-C Currents Comparison	26
Figure 2.25 Phase-A Current Comparison for Different Knee Voltages.....	27
Figure 2.26 Phase-A Current Comparison for Different Load Conditions.....	27
Figure 3.1 Played-in Voltage Measurements for Case 4	29
Figure 3.2 POW Played-in Phase A Voltage of Case 4.....	30
Figure 3.3 Flow Chart Describing the Optimization Process Implemented in PSCAD and the Fortran Script	36
Figure 3.4 Impact of Optimization Approach on Phase A Current of Case 4	41

Figure 3.5 Impact of Optimization Approach on Phase B Current of Case 4	41
Figure 3.6 Impact of Optimization Approach on Phase C Current of Case 4	42
Figure 4.1 Un-Filtered Positive Sequence Voltage Obtained for Case 1	44
Figure 4.2 Filtered Played-in Positive Sequence Voltage Obtained for Case 1	44
Figure 4.3 Un-Filtered Positive Sequence Voltage Obtained for Case 2	45
Figure 4.4 Filtered Played-in Positive Sequence Voltage Obtained for Case 2	45
Figure 4.5 Active Power Comparison for Case 1	46
Figure 4.6 Reactive Power Comparison for Case 1	47
Figure 4.7 Active Power Comparison for Case 2	47
Figure 4.8 Reactive Power Comparison for Case 2	48
Figure 4.9 Motor Speeds Comparison for Case 1	49
Figure 4.10 Motor Speeds Comparison for Case 2	49
Figure 4.11 Circuit Schematic in PSCAD to Generate the Test Cases	50
Figure 4.12 Circuit Schematic in PSLF	53

List of Tables

Table 2.1 Line Impedances considered in the model.....	5
Table 2.2 Three-phase Induction Motor Parameters.....	6
Table 2.3 Initial Single-Phase Motor Parameters [4].....	7
Table 2.4 Load Composition for Substtion A Summer Case Feeder Model	10
Table 2.5 Load Composition Across Three Segments of the Feeder Per Phase.....	10
Table 2.6 Residential Feeder and Laod Model Composition	10
Table 2.7 Single-phase Motor Parameters	14
Table 2.8 Single-phase Distribution Transformers Parameters	23
Table 2.9 Load Composition for Substation B In-service Feeder	24
Table 2.10 Load Composition for Substation B Reclosed Feeder.....	24
Table 2.11 Feeder and Load Composition depending on location	24
Table 3.1 SPIM Parameter Bounds.....	33
Table 3.2 Three-Phase Motor Parameters Bounds	33
Table 3.3 Final SPIM Parameters for Case 1.....	37
Table 3.4 Final SPIM Parameters for Case 2.....	37
Table 3.5 Final SPIM Parameters for Case 4.....	37
Table 3.6 Final Three-Phase Motor Parameters for Case 1, Case 2 and Case 4.....	38
Table 3.7 Final Load Compositiong for Case 1, Case 2 and Case 4.....	38
Table 3.8 Effectiveness of the Optimization Approach When Optimizing SPIM Parameters	39
Table 3.9 Effectiveness of the Optimization Approach When Optimizing Three-Phase Motor Parameters for Overall Current Vector	39
Table 3.10 Effectiveness of the Optimization Approach after Optimizing all the Load Parameters and ‘Scale’ Parameter	40
Table 4.1 Critical Parameters Bounds	51
Table 4.2 Final Coefficients obtained for the Regression Models.....	55
Table 4.3 Effectiveness of the Regression Models in the Testing.....	55

1. Introduction

1.1 Project Goals and Overview

The primary objective of this project is to synthesize distribution feeder and load models to study the effects of events such as faults and feeder pick-up events at the distribution and sub-transmission levels of a local utility in Arizona. The feeder and load model proposed in this work is comprised of single-phase induction motors, three-phase induction motors, impedance loads, distribution line segments and distribution transformers. It should also be noted that the following project objectives have been achieved in this work:

Case 1: A fault induced delayed voltage recovery (FIDVR) event, which is a 69 kV Phase A fault at a substation K, has been investigated in detail using the proposed feeder and load model by using the measured voltages and currents at the head of a 69/12.47 kV substation (substation A). This event occurred during summer conditions.

Case 2: The same model obtained in Case1 has been used to investigate another fault event at the 69-kV voltage level on phase A, which occurred during the winter season. The only change made in this model compared to the model used in summer case is that the load composition of the model in Case1 is scaled appropriately (by exactly a factor of 0.4) to match the pre-fault and post-fault measured steady state current values in this case. Similarly, the measurements of voltages and currents at the same 69/12.47 kV substation A (as used in summer case) has been used for this case.

Case 3: A feeder pick-up case, at another 69/12.47 kV substation (substation B), has been investigated using the same feeder and load model used in Case1 and Case2 except for the variation in the ratio of single-phase to three-phase induction motor load composition. This different ratio of motor load composition is accounted for by considering the types of load present in substation B area. From discussions with the local utility engineers, it has been determined that the load present on the substation B feeder is predominantly industrial/commercial type. For this reason, more three-phase induction motors loads compared to single-phase induction motor loads have been considered for this case. This event also occurred during summer conditions.

Case 4: The same event, that was investigated in Case 1, which is a 69 kV Phase A fault at a substation K, has been investigated in detail using the proposed feeder and load model, that was obtained from Case 3, by using the measured voltages and currents at the head of a different 69/12.47 kV substation (substation C). As mentioned before, this event occurred during summer conditions. In the cases mentioned above, Case1, Case2, Case3 have been analyzed by comparing the simulated current responses obtained in PSCAD to the measured current responses. In these cases, the measured voltages for all three-phases are played-in to the developed standard model in PSCAD to obtain the simulated current responses. This procedure is useful in obtaining two standard feeder and load models with a fixed set of load parameters (in all three phases and all the cases) and varying load composition according to its location.

Additionally, using Case 1, Case 2 and Case 4, the feeder and load models obtained using the above approach have been improved using an algorithmic (Gauss-Newton) approach to obtain the final set of parameters (varying in all three phases and in all cases) and varied load composition for each case. An application of the developed feeder and load models in positive sequence software packages, such as PSLF, has also been discussed in this report.

1.2 Organization of the Report

This report is organized into five chapters. The first chapter presents the objectives of this work. Chapter 2 mainly deals with developing a manual tuning approach to obtain different types of feeder and load models depending on its geographical location and load class. This chapter also contains the details of the individual components used to make up these feeder and load models. Chapter 3 provides a systematic analytical approach to obtain the parameters and the load composition of the feeder and load models using the measurements of voltages and currents from a 69-kV bus fault event in both summer and winter conditions at different locations. Chapter 4 presents the development of a linear regression model used to predict single-phase induction motor stalling in PSLF. The conclusions from this work has been provided in the Chapter 5 of this report. Possible future works based on the obtained standard feeder and load models and the proposed approaches has also been discussed in this chapter.

2. Manual Tuning Method to Synthesize Feeder and Load Models Using Voltage and Current Measurements

2.1 Introduction

To obtain a clear understanding of the load composition in the local utility system, a close consultation was held with its engineers. From this discussion, by analyzing three test cases as described below, efforts were made to obtain two standard three-phase feeder and load models with a fixed set of parameters (in all three phases and across all three cases) and according to its load class.

Two of these cases dealt with disturbances for which measurements at substation A were obtained and one case for which measurements at the substation B were obtained. The feeders at the substation A primarily supplied residential loads (for example: a large number of single-Phase air conditioner units) and the feeders at the substation B primarily supplied commercial and industrial loads (for example: large three-phase air-conditioner units in commercial buildings). This information provided the basis to design the load model composition depending on the substation at which measurements were obtained. It should also be noted that the main objective of this Chapter is to obtain a consistent set of parameters for a standard load model irrespective of the type of loads supplied by the feeders. However, varying the load composition by adjusting the percentage of different types of loads components depending on the nature of the load supplied is critical in capturing the transient behavior of the feeder and load model.

A systematic analytical approach, non-linear least squares Gauss-Newton method, has been pre-sented in Chapter 3 to obtain the load composition and the parameters of the considered feeder and load models. However, it is important to have a good initial condition to implement this analytical approach. Therefore, in this chapter, a manually tuned approach has been presented to obtain a good set of initial conditions (for both load composition and load parameters).

2.2 Individual Components Configuration of the Feeder Models

The feeder and load model used in this work is shown in Fig. 2.1. The loads and feeder components that makeup this feeder model, to recreate the fault and feeder pick-up events at substation A and substation B respectively, are:

- Single-phase induction motor loads.
- Three-phase induction motor loads.
- Impedance loads.
- Distribution line segments
- Distribution transformers

The details of the individual components that are part of the considered feeder and load model are presented below:

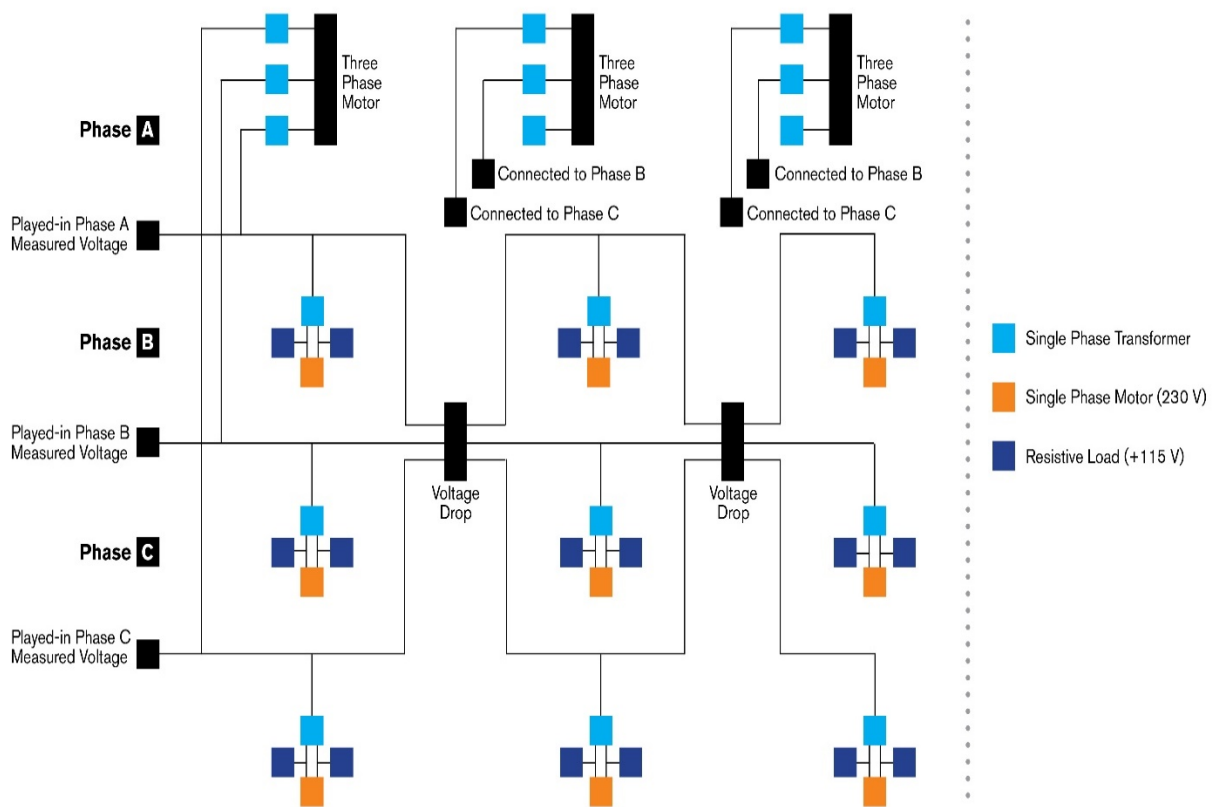


Figure 2.1: Feeder and Load Model used in Case 1, Case 2, Case 3 and Case 4

Table 2.1: Line Impedances considered in the model

Impedance Type	Positive Sequence Impedance Value	Negative Sequence Impedance Value	Zero Sequence Impedance Value
Resistance (ohm/mile)	0.3	0.3	0.798
Inductive Reactance (ohm/mile)	0.64	0.64	2.04
Capacitive Reactance (Mohm/mile)	0.01	0.01	0.01

2.2.1 Overhead Lines

The feeder model is assumed to have a total of less than 5% voltage drop across its length, in accordance with the recommendation provided by National Electrical Code (NEC) [1]. From Fig. 2.1, it can be clearly seen that the proposed feeder is divided into three parts of equal length. In the PSCAD model, this line is represented using a short length coupled pi-section between each segment. It should also be noted that in this model the distribution lines are represented as overhead lines. The line data for this pi model is provided in terms of positive, negative and zero sequence data per mile [2]. Therefore, the length of each coupled pi-section has been obtained for each case to ensure a maximum drop of 5% is achieved across the feeder. The impedance data used to represent these overhead lines, from [2], are shown in Table 2.1.

2.2.2 Three-Phase Induction Motors

The three-phase induction motor model considered is the squirrel cage type because of its ubiquitous presence in most of the motors present in practical distribution feeders. For this model, in PSCAD/EMTDC [3], torque control mode is used to operate the three-phase induction motors. These are motors which are typically rated at 460 V line-line RMS. Table 2.2 provides the data for the standard parameters considered for this model.

This motor model is available in the PSCAD library. The mechanical torque, in pu, of this motor is modeled using the following equation:

$$T_{\text{mechanical}} = k \quad (2.1)$$

Where, k is the initial load percentage pickup factor (0.65 in this case)

ω is the speed of the motor in pu

Table 2.2: Three-phase Induction Motor Parameters

Parameter	Values
Voltage Rating (line-line RMS)	460 V
H (Inertia Constant)	0.3 s
Stator Resistance	0.013 pu
Inner Rotor Resistance	0.009 pu
Outer Rotor Resistance	0.15 pu
Stator Leakage Inductance	0.067 pu
Inner Rotor Leakage Inductance	0.17 pu
Outer Rotor Leakage Inductance	0.225 pu
Magnetizing Inductance	3.8 pu
Initial Load Percentage Pickup	65%
Type of Mechanical Load	D =1
Power Factor	0.88

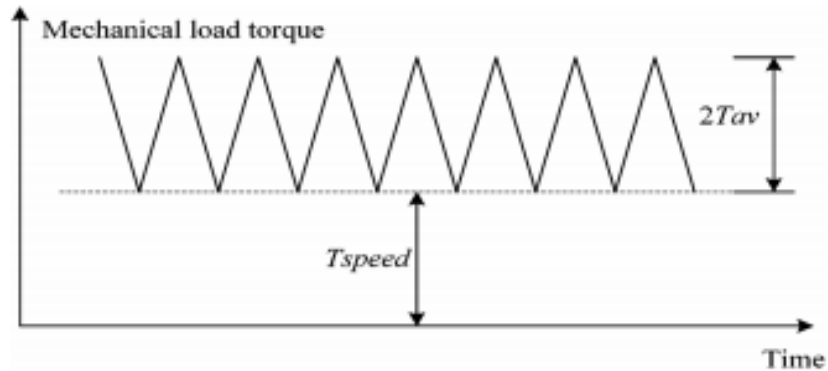


Figure 2.2: 2 Load Torque Profile for SPIM [4]

2.2.3 Single-Phase Induction Motors

The single-phase loads in the feeder model developed are represented as aggregated loads. For example, to represent 100 single-phase induction motors (SPIMs) at a particular location on the feeder, a single aggregated motor rated at 450 kVA is deployed (The rating of each SPIM is of 4.5 kVA rating).

The most predominant type of load that needs to be considered in the residential areas are the single-phase air conditioner compressor motors. It should be noted that this model is not available in the PSCAD library. For this reason, a user-defined single-phase induction motor (SPIM) model developed in [4] has been used for this work. From Fig. 2.2, it can be clearly seen that the load torque of the single-phase induction motor is represented in the form of a saw-tooth wave which includes both speed dependent load torque and angle dependent load torque.

The parameters of this model are obtained from [4] and are shown in Table 2.3.

Table 2.3: Initial Single-phase Motor Parameters [4]

Parameter	Values
Voltage Rating (line-line RMS)	230 V
Rotor Diameter	0.065 m
Stator Resistance	0.3 ohm
Main to auxiliary winding turns	1.4
Rotor Resistance	0.3 ohm
Stator Leakage reactance	0.5 ohm
Rotor Leakage reactance	0.2 ohm
Speed dependent load torque	8 N-m
Angle dependent load torque	6 N-m
Magnetizing reactance	30 ohm

The terminal resistance of a single SPIM is considered to be 5 μohm . This terminal resistance represents the line resistance between the distribution transformer and the SPIM. Similarly, the run capacitor of a single SPIM is assumed to be 80 μF . It should be noted that in this model, if the SPIM is scaled by a factor ‘ x ’ to represent the aggregated load, then the terminal resistance and the run capacitor should be scaled by the same factor ‘ x ’ to represent their equivalent values for the aggregated SPIM load.

2.2.4 Distribution Transformers

The modeling of the distribution transformers has been discussed in detail in the later sections of this chapter to investigate the effects of transformer saturation on feeder pick-up currents transients.

2.3 Case 1: Substation A Summer Event

2.3.1 Introduction and Case Setup

To obtain a novel residential feeder and load model, efforts are directed towards estimating appropriate (when compared to corresponding measured responses) current responses, for a FIDVR event, when measured three-phase voltages are played-in to the model. The details of this FIDVR event are given below:

Event type: Phase A line to ground fault at substation K on a 69-kV circuit breaker.

Event time of occurrence: 10:33 AM on 8th August 2016.

Available DFR measurements: Voltages, Currents point on wave data at substation A (12.47 kV – low voltage side of the substation)

For this feeder analysis, the available three-phase voltage measurements are played into a three-7

phase feeder model in PSCAD. The three-phase played-in voltages for this event are presented below in Fig. 2.3.

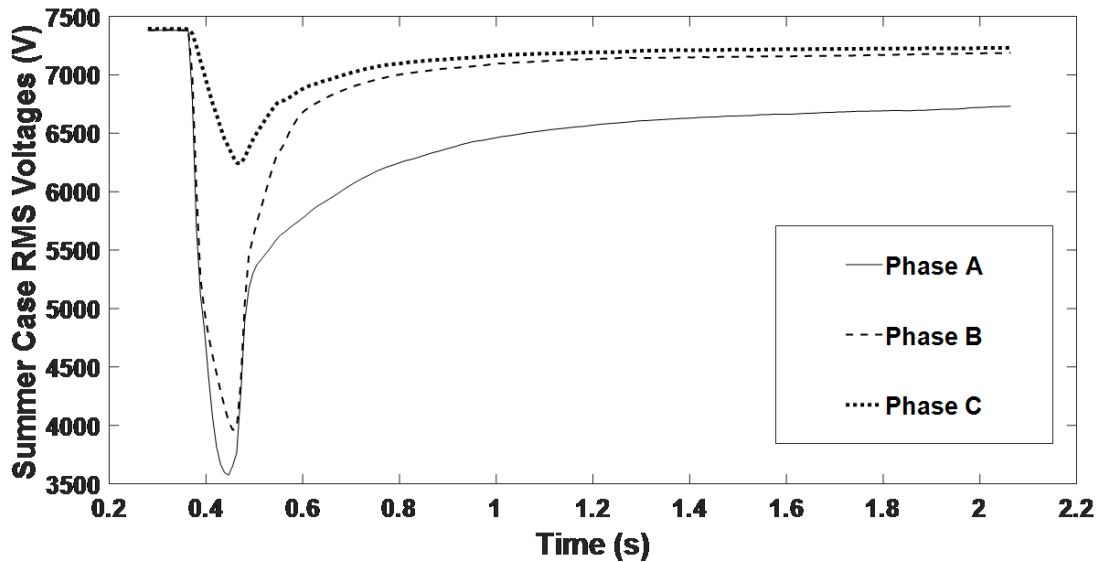


Figure 2.3: Case 1 RMS Three-Phase Voltage Profiles

Note1: Although only phase-A is faulted, phase-B voltage also seems to be severely affected due to the Delta-Wye configuration of the transformers between the sub-transmission level and the distribution level

From Fig. 2.3, it can be clearly seen that the voltage plot characterizes a FIDVR event because the phase A voltage takes a long time to recover to the nominal state after the fault is cleared. Although, Fig. 2.3, shows the RMS voltage waveforms, corresponding POW three-phase voltage waveforms have been played-in to the model. The POW played-in voltage of Phase A is presented in Fig. 2.4.

It should be noted that in this work, Case 1, Case 2, Case 3 and Case 4 have been represented in PSCAD, using the schematic shown in Fig. 2.5.

2.3.2 Load composition

After consulting with the local utility engineers, it was determined that the substation A feeders are located in residential areas and primarily serve residential load. This information was used as a starting point to formulate the load model composition.

A large percentage of the load is assumed to be SPIM because residential areas usually have a large percentage of load which comprises of air conditioners, ceiling fans, refrigerators and other appliances driven by SPIMs. A smaller portion of three-phase motor loads has been assumed to represent a few commercial buildings or offices with air conditioners driven by three-phase motors. An even smaller amount of lighting loads has also been represented in the model. The load compositions for this FIDVR case was determined after iterating using a simple

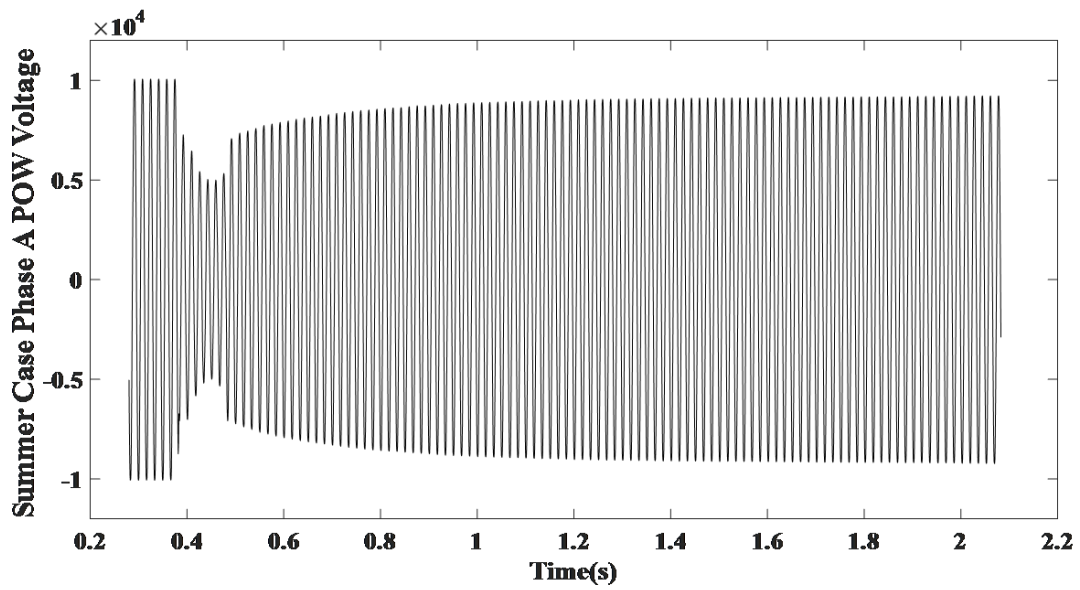


Figure 2.4: POW Played-in Phase-A Voltage Measurement for Case 1

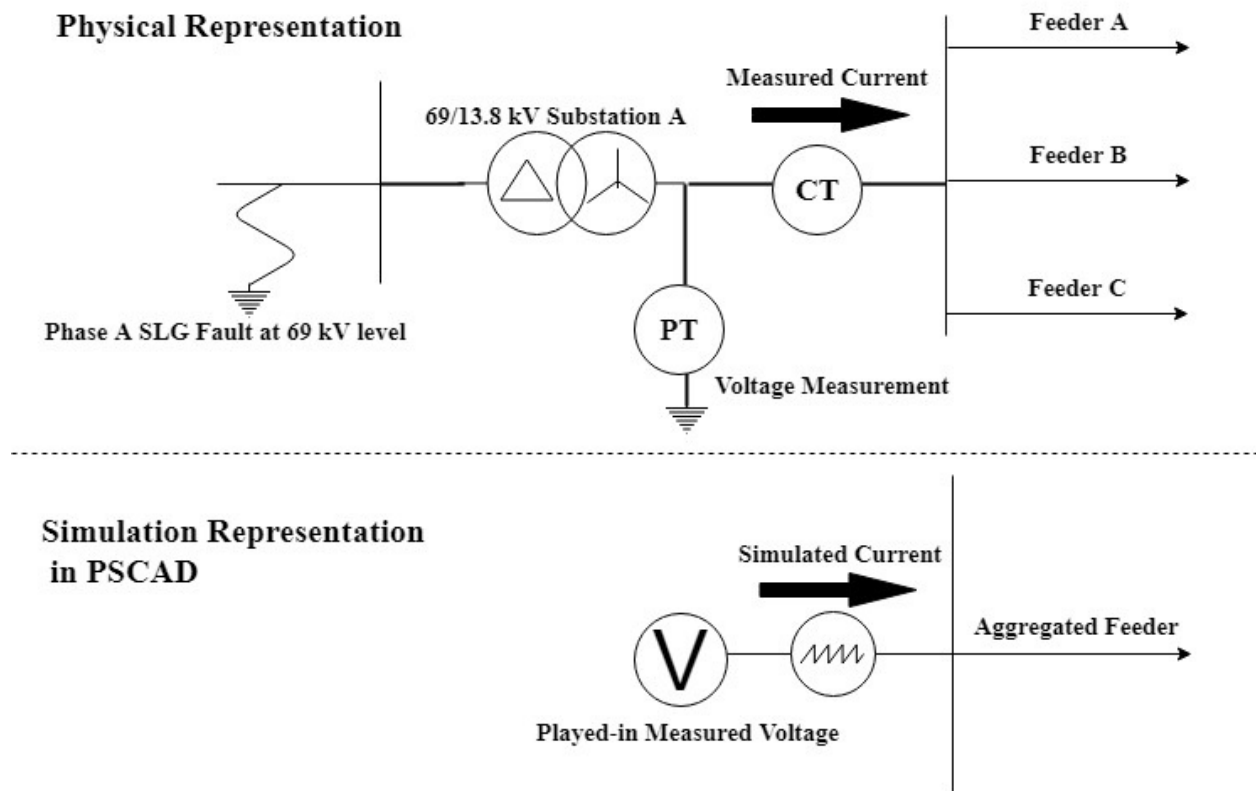


Figure 2.5: Simulation vs Actual System Representation

trial and error process to obtain the best match between the simulated current obtained from PSCAD with the played-in measured voltage and the actual measured current is presented in Table 2.4.

Table 2.4: Load Composition for Substation A Summer Case Feeder Model

Type of load	Phase A	Phase B	Phase C
Lighting Load	0.594 MW	0.594 MW	0.594 MW
Single-Phase Load	4.56 MVA	4.56 MVA	4.56 MVA
Three-Phase Load (1/3 Total Load)	1.14 MVA	1.14 MVA	1.14 MVA

The load composition across the three segments of the feeder is shown in Table 2.5.

Table 2.5: Load Composition Across Three Segments of the Feeder Per Phase

Type of load	Segment 1	Segment 2	Segment 3
Lighting Load	0.2 MW	0.2 MW	0.2 MW
Single-Phase Load	1.2 MVA	1.68 MVA	1.68 MVA
Three-Phase Load	0.38 MVA	0.38 MVA	0.38 MVA

From Table 2.5, it can be observed that both lighting loads and three-phase loads are distributed equally along each segment of the feeder in each phase. Whereas, the single-phase loads are distributed in the ratio of 1:1.4:1.4 along the three segments of the feeder in each phase. The primary reason for choosing this ratio of SPIM loads across the three segments is to capture the FIDVR phenomenon observed in the measured voltages and is known to occur due to the stalling of SPIMS. It should also be noted that during this process to determine the load composition in this feeder model, the parameters of SPIM obtained from Table 2.3 are used as the starting point of this analysis.

Based on Table 2.4 and Table 2.5, the final percentages of all the loads in the considered residential feeder and load model are presented in Table 2.6.

Table 2.6: Residential Feeder and Load Model Composition

Feeder Type (Geographical)	Single-phase Load	Three-phase Load	Impedance Load
Residential	72%	18%	10%

Therefore, motor load comprising of 90% of the total load has been obtained in this model. It should be noted that the same percentage of motor loads (90%) and lighting loads (10%) as used in this case are used in both Case2 (substation A winter case), Case3 (substation B feeder pick-up case).

2.3.3 Parameter Sensitivity Analysis

As shown in Fig. 2.5, the POW voltages corresponding to their RMS waveforms, in Fig. 2.3, are played-in to this feeder and load model to capture accurate simulated current responses. For

this reason, parameter sensitivity analysis has been done in this work. The feeder current profiles of all three-phases, in this case, have been presented in Fig. 2.6, Fig. 2.7 and Fig. 2.8. A vertical line has been shown in Fig. 2.6, Fig. 2.7, Fig. 2.8 to represent the instant of fault initiation in all the three-phases.

From Fig. 2.6, it can be clearly observed that the post-fault current in Fig. 2.6 is higher than the pre-fault current by around 300 Amps. This indicates stalling of motors, where the stalled motors draw locked rotor current until they are tripped due to internal protection. Since, in the available data obtained from Schneider ION 7650 and Schneider ION 8650A meters, the time span after the fault is cleared is only about 1 sec, the locked rotor current does not die away in the observed time span. It should also be noted that this phenomenon is not observed in Fig. 2.7, Fig. 2.8. Hence, efforts have been concentrated on making motors stall (after the fault is applied) in only phase A of the feeder.

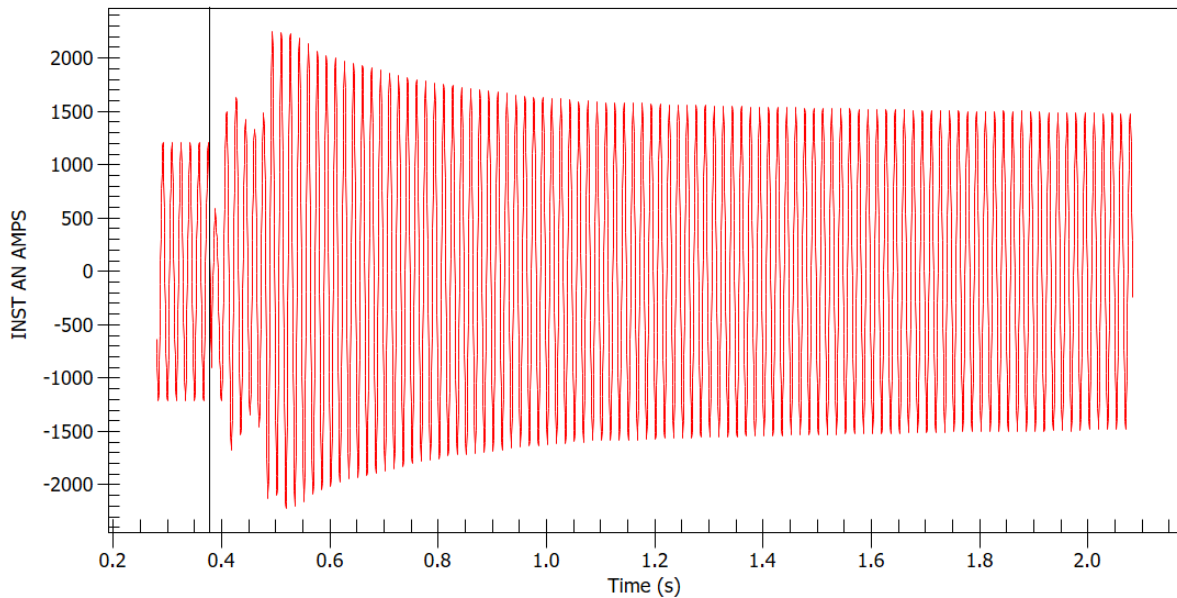


Figure 2.6: Phase A Faulted Current at Substation A for Case 1

The procedure to match the pre-fault simulated three-phase currents at the head of the feeder with their corresponding measured responses has been documented in detail in [5]. After obtaining the pre-fault currents, as mentioned earlier, load composition has been determined for this feeder model. Thereafter, parameter sensitivity analysis has been done to get a close match of the fault transients as seen from Fig. 2.6. This is because, the FIDVR phenomenon is observed in the Phase A (faulted phase) and it is important to capture the post-fault steady state current in the faulted phase in the PSCAD simulations using this feeder and load model.

Critical Parameters:

The following parameters of the SPIM are tuned in the sensitivity analysis to obtain a good match of the post-fault steady state simulated current in the faulted phase, Phase A, when compared to its corresponding measured post-fault steady state current:

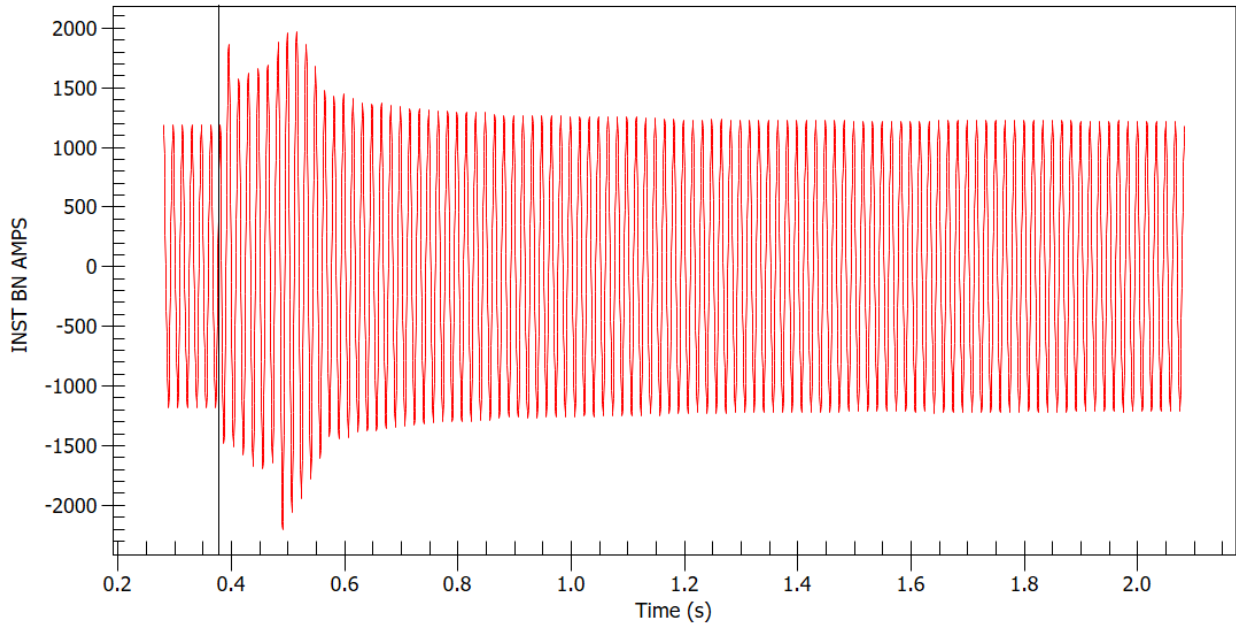


Figure 2.7: Phase B Non-Faulted Current at Substation A for Case 1

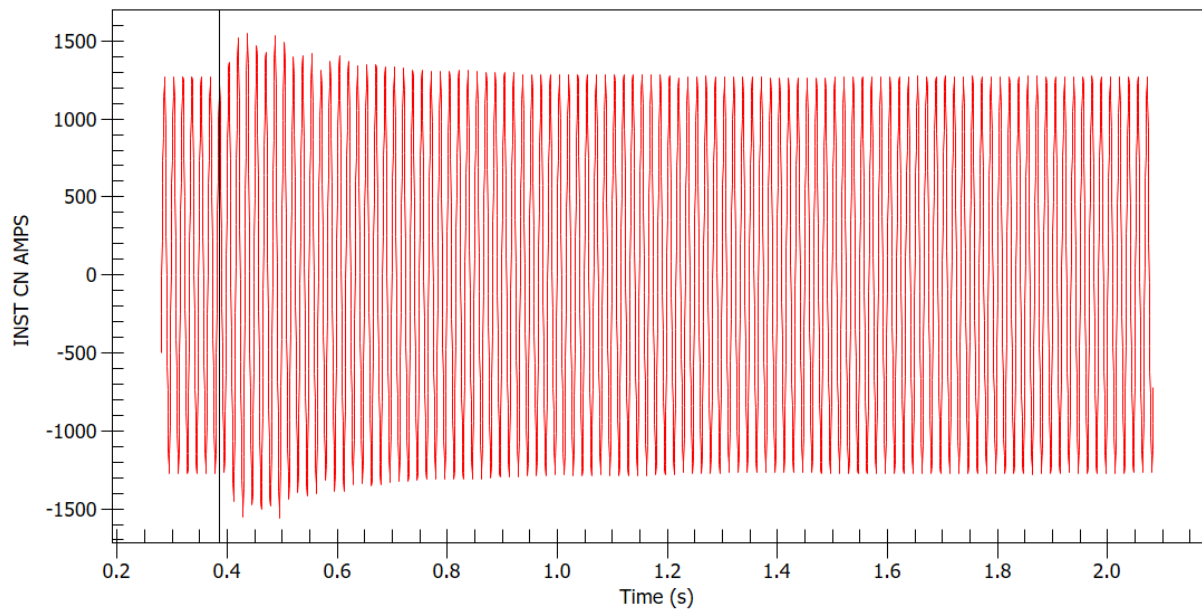


Figure 2.8: Phase C Non-Faulted Current at Substation A for Case 1

Number of SPIMs: It is known that during the fault, the voltage level in the system decreases. Due to this, the speeds of the SPIM motors reduce until the fault is cleared. After the fault is cleared, the SPIMs require more reactive power to get back to the nominal speed. This indicates that more the number of motors in an aggregated motor, the more probable it is to stall (thereby all the individual motors stall) because the aggregated motor requires reactive power to re-accelerate to the nominal speed. From this observation, it can be concluded that this parameter (number of motors) is very important in the sensitivity analysis. The final value of this parameter has been obtained from the load composition as mentioned earlier in this chapter.

Rotor Resistance: The slip of an induction motor is directly affected by the rotor resistance. Since, slip is a function of the rotor speed this is another parameter which is found to be the most sensitive in the sensitivity analysis. This parameter is especially important in matching the current during the faulted condition (before the fault is cleared).

Inertia of SPIMs: It was observed that, after the rotor resistance, the inertia of the motors was found to be the most sensitive parameter in the simulations conducted. It played an important role in determining at what time the SPIMs reach the nominal speed after a fault clearance. The inertia of the motor is closely related to its rotor diameter. Therefore, using a base value of 6.5 cm from Table 2.3 the sensitivity analysis from 6 cm to 8 cm has been considered for different SPIM motors. It was observed that at 7 cm, the desired results (to get a good match between the post-fault simulated and measured current responses in the faulted phase) has been obtained.

It should be noted that the above sensitivity analysis has also been performed on the other parameters of SPIM and their sensitivity order has been presented below:

$$\text{Rotor resistance} > \text{Inertia} > \text{Stator resistance} > \text{Rotor reactance} > \text{Stator reactance} \quad (2.2)$$

Using the obtained sensitivity order, as shown in (2.2), the SPIM parameters are tuned manually by changing them individually to ensure that a good match between the post-fault simulated steady state current and its corresponding measured response has been obtained in the faulted phase.

Note: The magnetizing reactance of the SPIMs barely had any impact on the simulated feeder currents and therefore, was not manually tuned using the sensitivity approach mentioned in the above paragraph.

In PSCAD simulations, it is observed from the plots of the speeds of the motors, that after a fault is applied, the SPIMs are the most affected by the fault whereas the three-phase motors are the least affected. This impact on SPIMs seems to be logical considering that the inertia of the SPIMs is very low whereas the three-phase motors have a higher inertia. Another reason for this impact on SPIMs might also be due to the fact that only one phase is faulted. Hence, the two other phases are supporting the three-phase motors. For these reasons, the sensitivity analysis and the manual tuning of the parameters for this substation A case has been conducted only for SPIMs.

Figs. 9-11 depict the end-result of the sensitivity investigation. These figures show the speeds of the nine blocks of single-phase motors (see Fig. 2.1) from a single simulation conducted using the final parameter values of SPIMs as shown in Table 2.7.

Table 2.7: Single-phase Motor Parameters

Parameter	Values
Voltage Rating (line-line RMS)	230 V
Rotor Diameter	0.07 m
Stator Resistance	0.3 ohm
Main to auxiliary winding turns	1.4
Rotor Resistance	0.5 ohm
Stator Leakage reactance	0.6 ohm
Rotor Leakage reactance	0.4 ohm
Speed dependent load torque	7.1 N-m
Angle dependent load torque	5.1 N-m
Magnetizing reactance	30 ohm

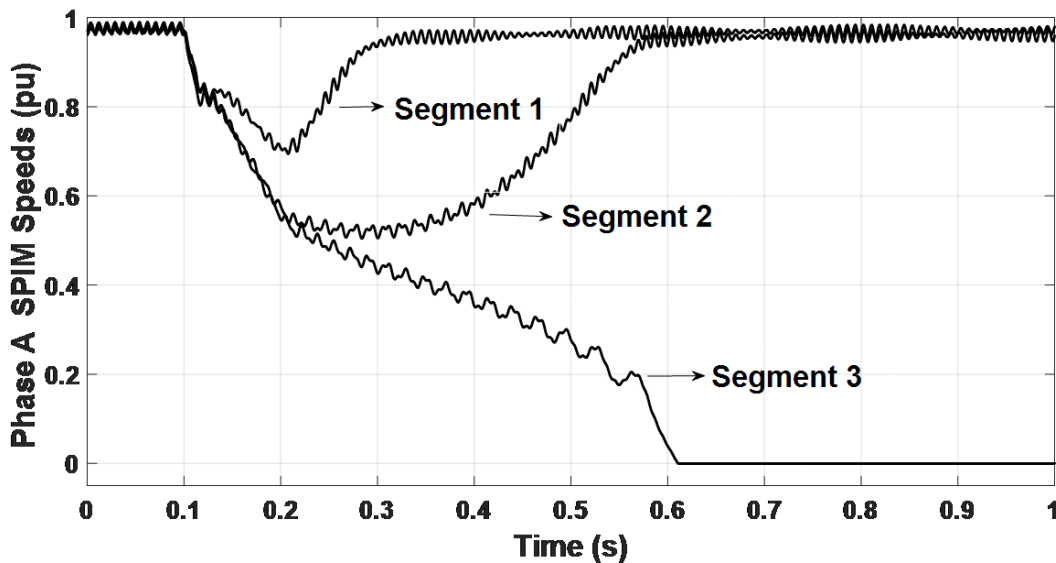


Figure 2.9: SPIM Speeds at Three Different Segments Across the Feeder in Phase A

From Fig. 2.10, it can be clearly observed that the speeds of the SPIMs are not as affected as observed in phase A from Fig. 2.9. This is to be expected because phase B is not the faulted phase. The speeds of SPIMs in Fig. 2.11 (phase C) are even less affected due to the phase A fault. This is because as mentioned earlier in Note1, the voltage in phase B has a dip similar to phase A due to the Y-Delta transformers whereas voltage in phase C sees the least dip as it is not the faulted phase nor is affected by the Y-Delta transformers in the 69-kV network.

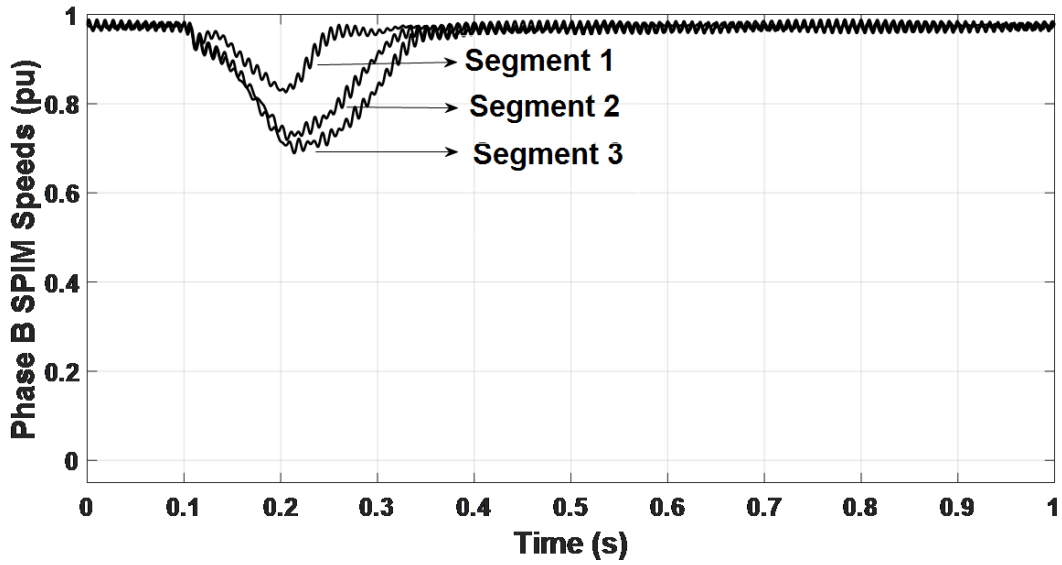


Figure 2.10: SPIM Speeds at Three Different Segments Across the Feeder in Phase B

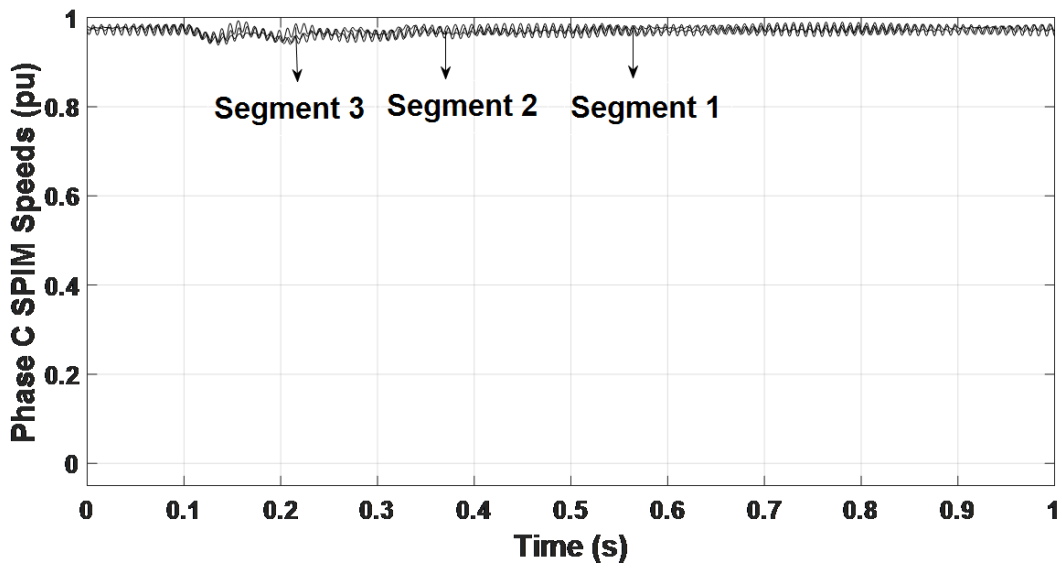


Figure 2.11: SPIM Speeds at Three Different Segments Across the Feeder in Phase C

2.3.4 Case 1: Results and discussion

The final simulated currents at the head of the feeder are as shown below in Fig. 2.12, Fig. 2.13, Fig. 2.14. From Fig. 2.12, it can be clearly seen that for the faulted phase A current, a good match between the simulated current and measured current has been obtained. This is a clear indication that stalling occurred in the SPIM's of this phase due to this FIDVR event.

From Fig. 2.13, it can be observed that apart from the time period of 0.25 sec to 0.35 sec a very good match between the simulated current and measured current for phase B is obtained. From sensitivity analysis, it is observed that mismatch from 0.25 sec to 0.35 sec can be reduced by changing the inertia of SPIM's from chosen rotor diameter value of 7 cm to 8 cm. However, to keep the parameters for all the motors in all phases to be same the final result for rotor diameter of 7 cm is presented here.

From Fig. 2.14, it can be concluded that even for the least affected phase the simulated current obtained has a very good match with the measured current of phase C.

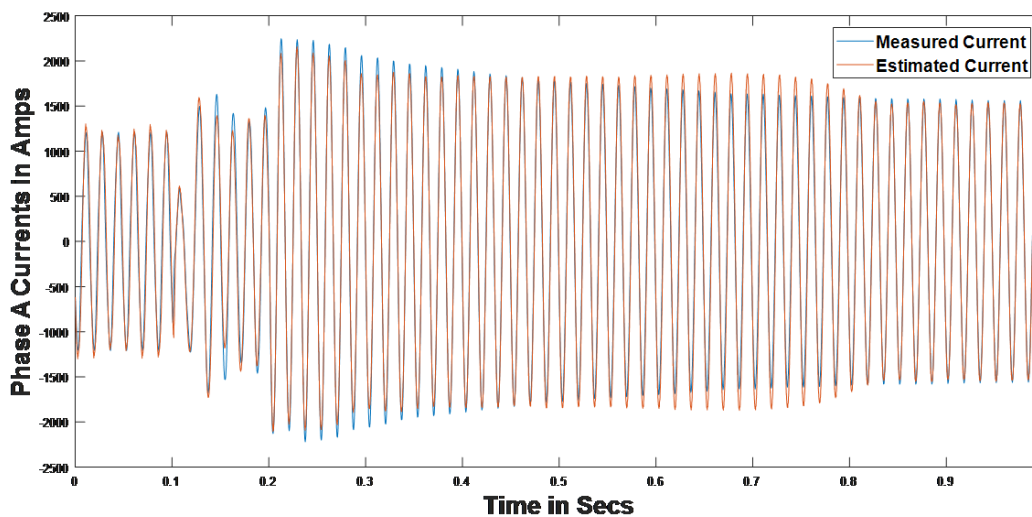


Figure 2.12: Phase A Current Comparison for Summer Case

2.4 Case 2: Substation A Winter Event

2.4.1 Introduction

In this case, the same feeder and load model used in the substation A summer case (Case 1) has been used to verify the validity of the model during winter conditions. As shown below, the only difference in this case (compared to Case 1) being the sub-transmission SLG fault occurred during winter conditions (very low loading conditions).

Event Details:

Event type: Phase A line to ground fault at substation K 69 kV bus.

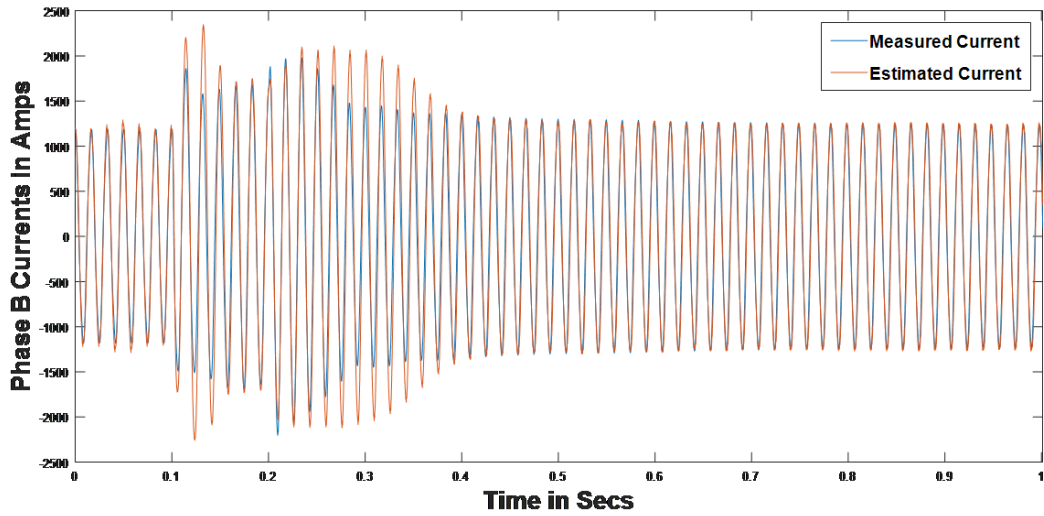


Figure 2.13: Phase B Current Comparison for Summer Case

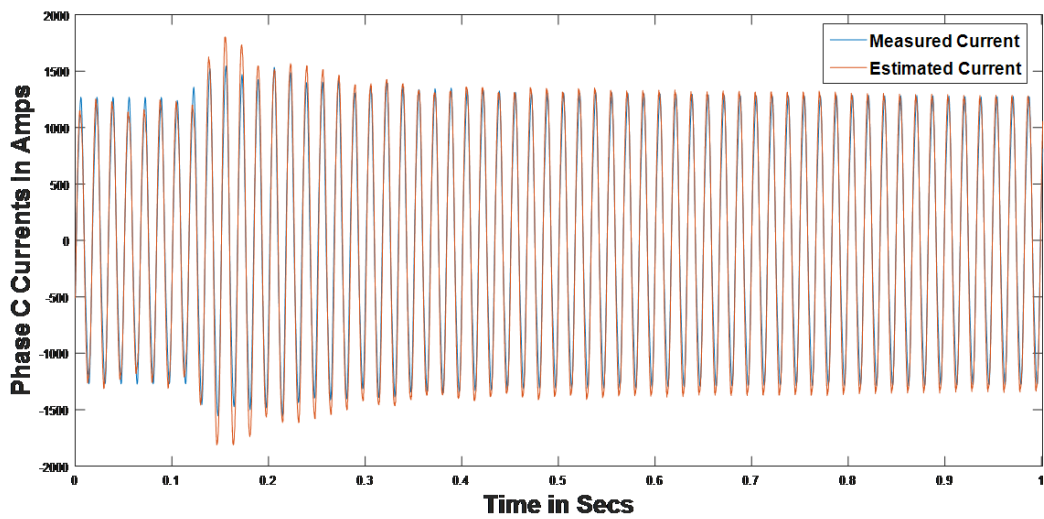


Figure 2.14: Phase C Current Comparison for Summer Case

Event time of occurrence: 5:36 PM on 11th November 2016.

Available DFR measurements: Voltages, Currents point on wave data at substation A (12.47 kV –low voltage side of the substation)

Fig. 2.15 shows the measured voltages that are played into this model to obtain the simulated currents at the head of the feeder.

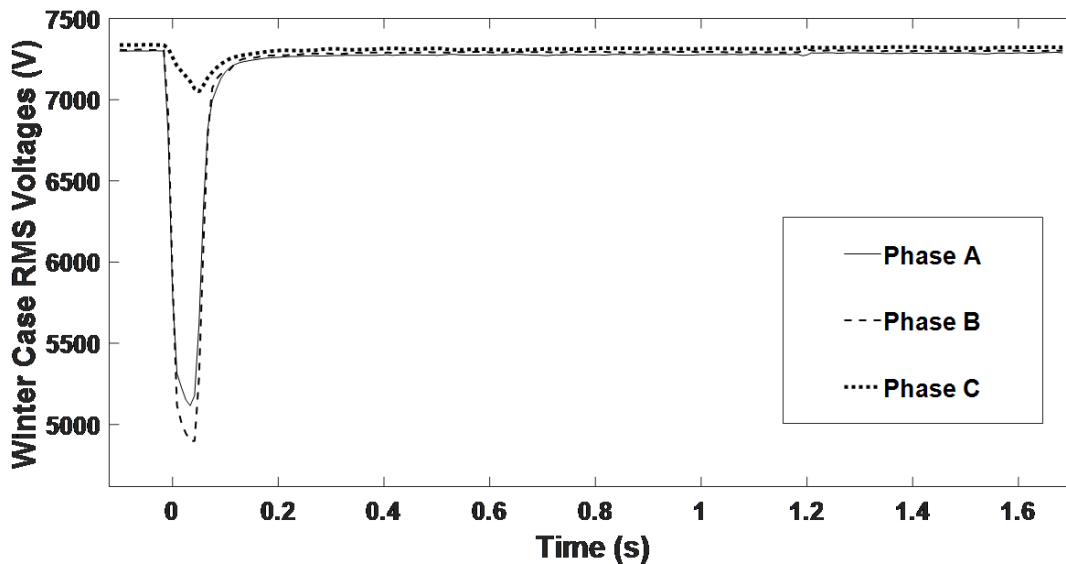


Figure 2.15: Three-Phase RMS Voltage Profiles for Case 2

From Fig. 2.15, it can be seen that all three voltages recover to the nominal voltage (after the fault is cleared) very quickly compared to the phase A voltage response of Case 1: Substation A Summer case. From this, it should be expected that there would be no stalling of SPIMs being involved in this case. It should also be noted that the three-phase POW voltage waveforms corresponding to the RMS voltage waveforms in Fig. 2.15 are played-in to this feeder and load model.

2.4.2 Substation A Winter: Load composition

The load composition from Table 2.4, Table 2.5 are scaled by exactly a factor of 0.4 to obtain the load composition for this case. This scaling is done to match the pre-fault current measured values from the obtained simulated responses. Although, the total load from the substation A summer case (Case 1) is scaled down by 0.4 the ratio between the single-phase motor load to three-phase motor load and the lighting load percentage composition is kept constant for these two cases.

2.4.3 Substation A Winter: Critical parameters and parameter sensitivity analysis

The same parameters for the feeder and load used in substation A summer model have been used for this case. Hence, sensitivity analysis and manual tuning of the parameters is not required.

2.4.4 Substation A Winter: Results and Discussion

Fig. 2.16, Fig. 2.17, Fig. 2.18 show that a very good correspondence has been achieved between simulated and measured currents by using the same feeder and load model from substation A summer case in winter conditions. These results also illustrate that this residential feeder and load model is able to capture the transient fault characteristics for both summer and winter conditions consistently.

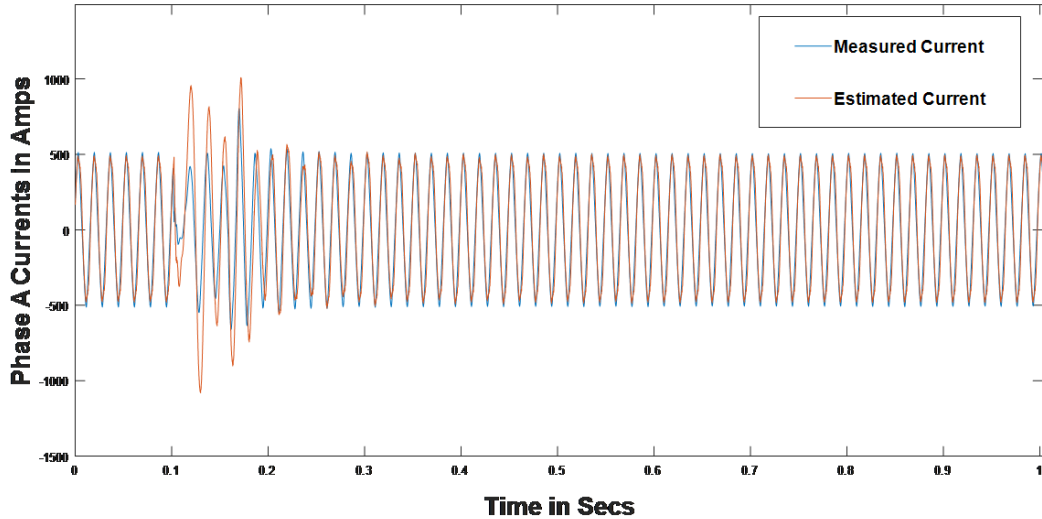


Figure 2.16: Phase A Current Comparison for Winter Case

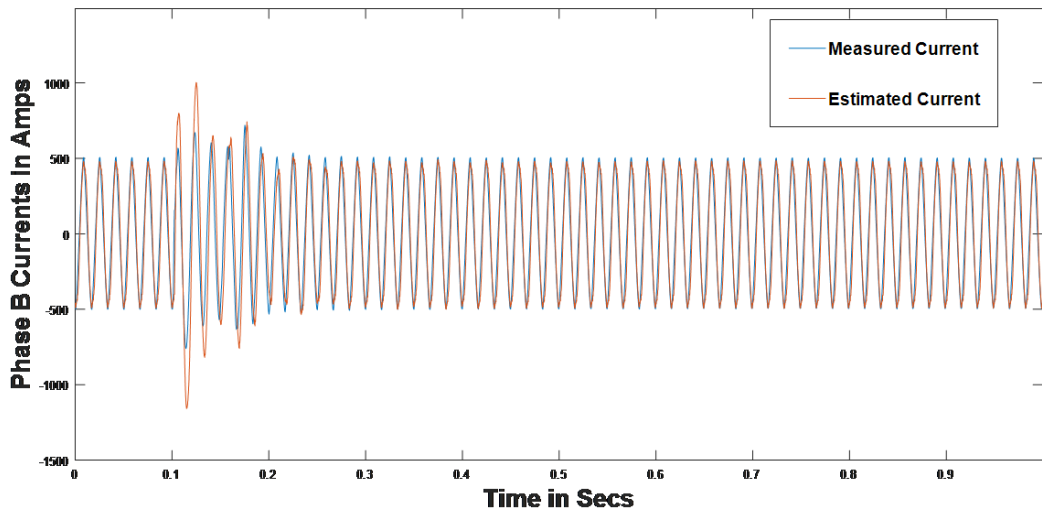


Figure 2.17: Phase B Current Comparison for Winter Case

It should also be noted that as expected, it was observed from the simulations conducted that no stalling of SPIMs is involved in this case.

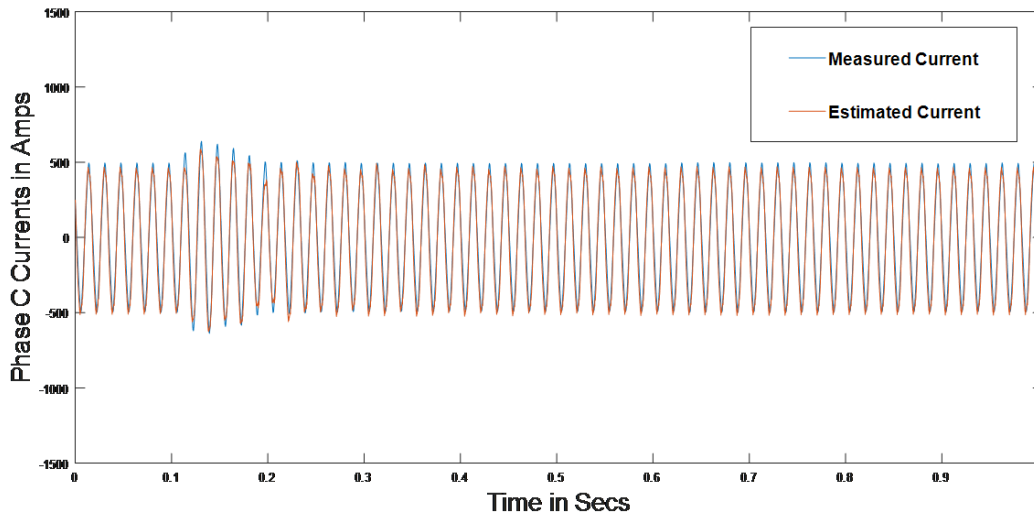


Figure 2.18: Phase C Current Comparison for Winter Case

2.5 Case 3: Substation B Summer Event

2.5.1 Introduction

This section details the procedure for obtaining a novel feeder model to estimate accurate current responses, for a three-phase feeder pick-up event at the substation B, when measured three-phase voltages are played-in to the model. From the information provided by the local utility engineers, it was identified that the major load composition near substation B primarily consists of commercial buildings and industrial loads dominated by three-phase loads. The one-line diagram of substation B and its downstream feeders is presented in Fig. 2.19.

Event Details:

Event type: Three-phase feeder pick-up

Event time of occurrence: 8:59 PM on 29th July 2016.

Available DFR measurements: Voltages, Currents point on wave data at substation B (12.47 kV – low voltage side of the substation)

It should be noted that a storm was present in this area and a fault was cleared on Feeder 3 by tripping the feeder. The event considered in Case 3, from Table 2.1, is the pick-up of this feeder 27 minutes after the feeder was tripped (during this interval the feeder had been completely deenergized).

For this event, the three-phase POW measured voltages, corresponding to the RMS voltages as shown in Fig. 2.20, are played-in to this model. The parameters of the distribution transformers considered for this model are presented in Table 2.5. It should also be noted that the same distribution transformer model is used for the residential feeder and load model in Case 1 and Case 2.

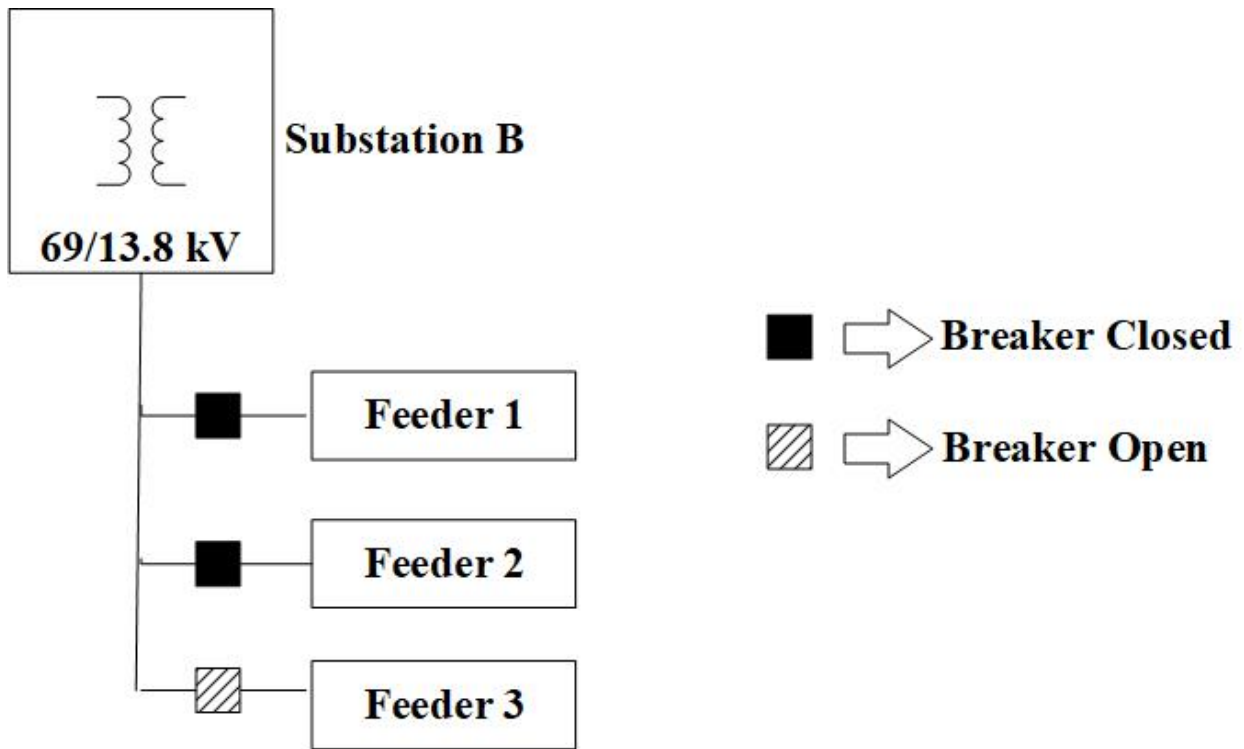


Figure 2.19: Single Line Diagram of the Substation B Area

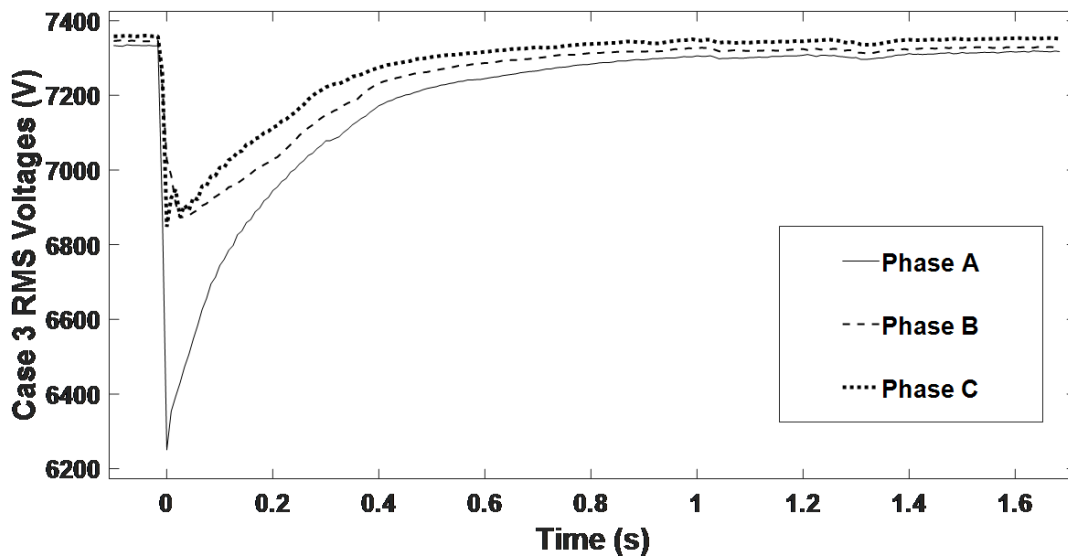


Figure 2.20: Three-Phase RMS Voltage profiles for Case 3

Note2: Similar to Case1, Case2, the voltages played into this feeder model are instantaneous representations of Fig. 2.20.

Similar to Case1 and Case2, the primary objective of this chapter is to obtain an accurate estimate of the feeder currents measured at the head of the substation B feeder.

2.5.2 Critical Parameters of Distribution Transformers

From the simulations conducted, it is observed that the transformer saturation is the major contributor in obtaining the desired simulated currents at the head of the feeder for this feeder pick-up event. In PSCAD [3], the transformer knee curve characteristic to represent saturation in a transformer is shown in Fig. 2.21. From Fig. 2.21, it can be observed that the air core reactance is given by the slope of the asymptote. From Table 2.8, it is seen that the air core reactance is assumed to be the same as the leakage reactance of the transformer. To ensure that the voltage regulation in the transformer is kept minimal, the leakage reactance is assumed to be 2%.

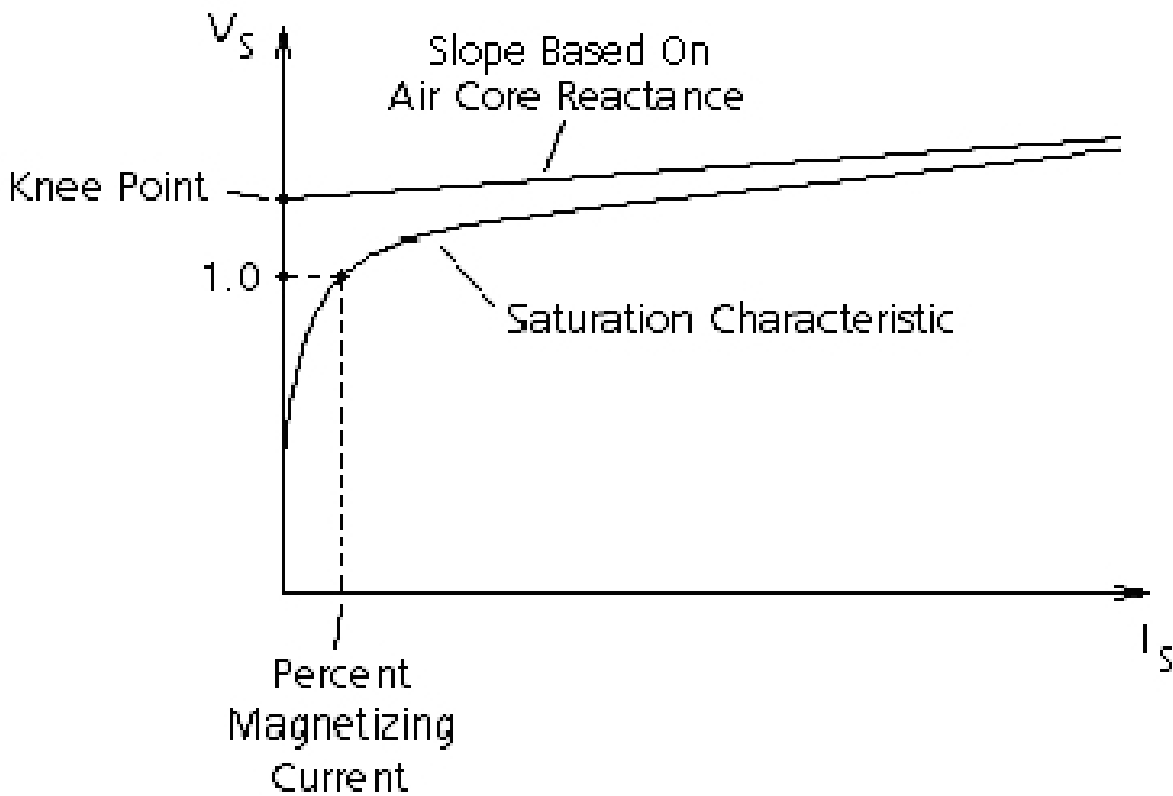


Figure 2.21: Transformer Knee Curve Characteristic [3]

Additionally, from Fig. 2.21, the magnetizing current characterizes the degree of nonlinearity of the flux-current characteristic of the transformer and the knee point represents the y-intercept of the asymptote. From [6], it is seen that the magnetizing current for a typical 1 MVA transformer is about 1-2 %. Using these critical parameter values, it is observed that at a knee voltage of 1.17 pu

a good match between the simulated currents and the measured currents is achieved for the starting transient in the three phases as shown in Fig. 2.22, 2.23 and 2.24.

It should also be noted that the three-phase transformers, in this feeder and load model, are represented using three single-phase transformers (equivalent to Y-Y configuration in three-phase transformers). Table 2.8 shows the parameters obtained for these single-phase distributed transformers.

Apart from these parameters, the critical parameters used to obtain a good match between the measured currents and the simulated currents are given below:

Series Resistance: A resistance in series with the primary winding of the single-phase transformer plays an important role in ensuring that the transformer saturation dies out after first few cycles of the transient. The optimum value of this resistance is found to be 0.5 ohm. This resistance signifies the distance of the distribution transformer from each segment of the feeder model.

Switch Closing Instant: The instant the circuit breaker closes has a huge impact on the DC offset present in the starting transient of the simulated currents. In this case, the instant of breaker closing for Phase A is the closest to voltage zero crossing. Therefore, the highest DC offset is observed in Phase A current transient.

Table 2.8: Single-phase Distribution Transformers Parameters

MVA Rating	1 MVA
Leakage Reactance	0.02 pu
Air Core Reactance	0.02 pu
Inrush Decay Constant	0.25 sec
Magnetizing Current	2 %
Knee Voltage	1.17 pu
Saturation Enabled	Yes
Voltage Ratio (line to neutral RMS)	7.96 kV/ 265 V

2.5.3 Case 3: Load Composition

From the geographical information provided by the local utility near substation B, it is known that most of the loads located near substation B, are of industrial/commercial type. For this reason, the load composition for this feeder model has been modified, using the same procedure mentioned in Case 1 load composition analysis, from the feeder model used in substation A summer and winter cases. This modification can be seen in Table 2.9 and Table 2.10:

From Table 2.10, Table 2.11 it can be clearly observed that the following proportions, as shown in Table 2.11 of loads has been used to match the pre-event measured P, Q values:

It should also be noted that in the load compositions shown in Table 2.9, Table 2.10 the ratio of load composition across the three segments of the feeder is as shown below:

Table 2.9: Load Composition for Substation B In-service Feeder

Type of load	Phase A	Phase B	Phase C
Impedance Load	0.283 MW	0.283 MW	0.283 MW
Single-phase Load	0.8 MVA	0.8 MVA	0.8 MVA
Three-phase Load (1/3 Total Load)	2.06 MVA	2.06 MVA	2.06 MVA

Table 2.10: Load Composition for Substation B Reclosed Feeder

Type of load	Phase A	Phase B	Phase C
Impedance Load	0.08 MW	0.08 MW	0.08 MW
Single-phase Load	0.225 MVA	0.225 MVA	0.225 MVA
Three-phase Load (1/3 Total Load)	0.588 MVA	0.588 MVA	0.588 MVA

- Resistive Load – 1:1:1
- Three-phase Load – 1:1:1
- Single-phase Load – 1: 1.4: 1.4

The key point to be noted here is that the above proportions are the same as the proportions used to represent the load composition across the three segments of the substation A summer and winter case feeder and load models.

2.5.4 Results and Discussions

The simulated currents at the head of the substation B are compared with their corresponding measured currents as shown in Fig. 2.22, Fig. 2.23, Fig. 2.24:

From Fig. 2.22, Fig. 2.23, Fig. 2.24 it can be observed that a good approximation of the starting inrush characteristic of the three-phases of the measured currents has been achieved from this substation B feeder and load model.

From Fig. 2.25, it can be observed that at high knee voltage values (transformer saturation is not present) the initial cycles of the simulated current transient do not have good correspondence with the corresponding measured current transient. However, at a low knee voltage value (final obtained value) the desired effect has been achieved.

Table 2.11: Feeder and Load Composition depending on location

Feeder Type (Geographical)	Single-phase Load	Three-phase Load	Impedance Load
Industrial/Commercial	25%	65%	10%

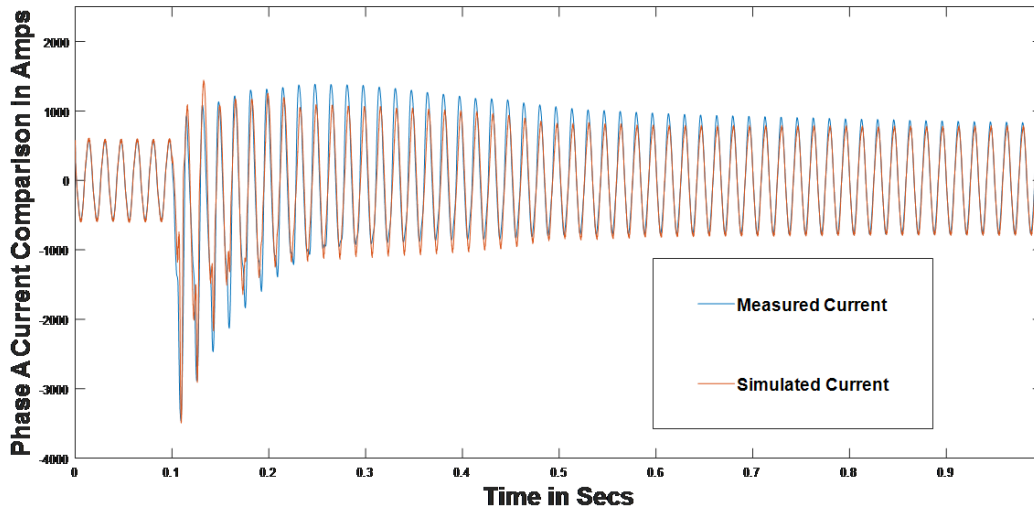


Figure 2.22: Phase-A Currents Comparison

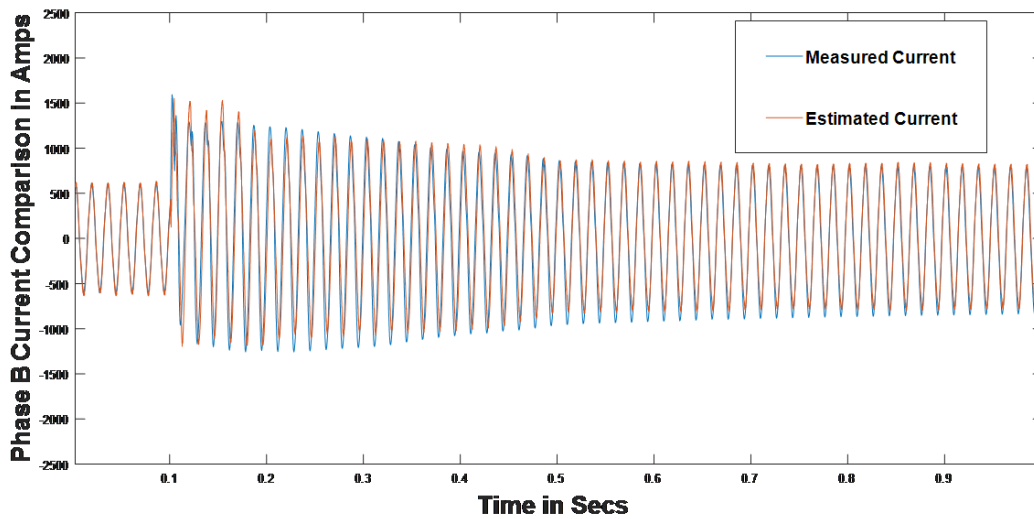


Figure 2.23: Phase-B Currents Comparison

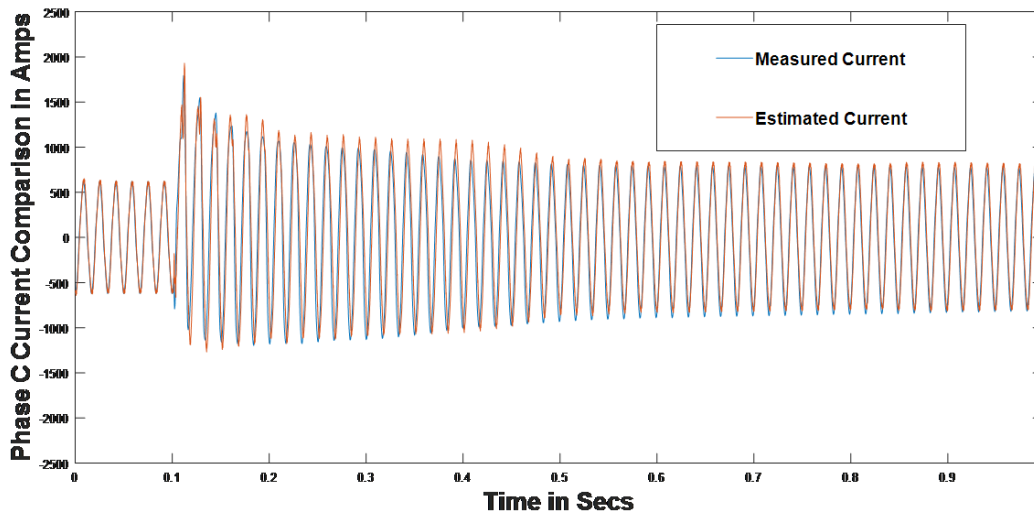


Figure 2.24: Phase-C Currents Comparison

Additionally, from Fig. 2.26, it can be observed that the starting cycles of the transient is not affected with the reduction of load (total load of 1.08 MVA in the picked-up feeder is reduced) and the difference can only be observed in the latter cycles by which time the transformer saturation has died out. From this observation, it can be inferred that the first few cycles of the current inrush characteristics do not depend primarily on the type of load present on the feeder and is mainly dependent on the distribution transformer saturation characteristics.

It should also be noted that the load parameters for the standard feeder and load model (see Fig. 2.1) are obtained using Case 1 and Case 2 as the distribution transformers are already energized at the time of fault initiation and hence its parameters on the current transient response is negligible. However, in this case, for the feeder pick-up event, the starting characteristic of the transformers played a significant role in the transient response of the current whereas the load parameters didn't have much impact on it. Therefore, the combination of these three cases (Case 1, Case 2 and Case 3) have been useful in obtaining the load compositions and the feeder and load model parameters for a standard feeder and load model.

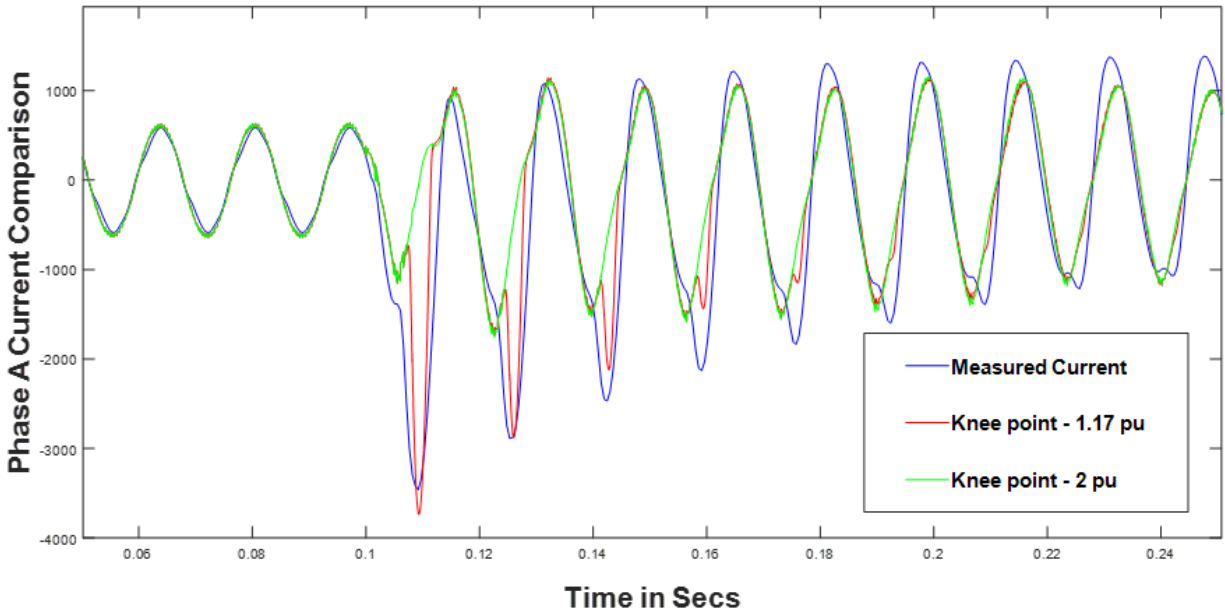


Figure 2.25: Phase-A Current Comparison for Different Knee Voltages

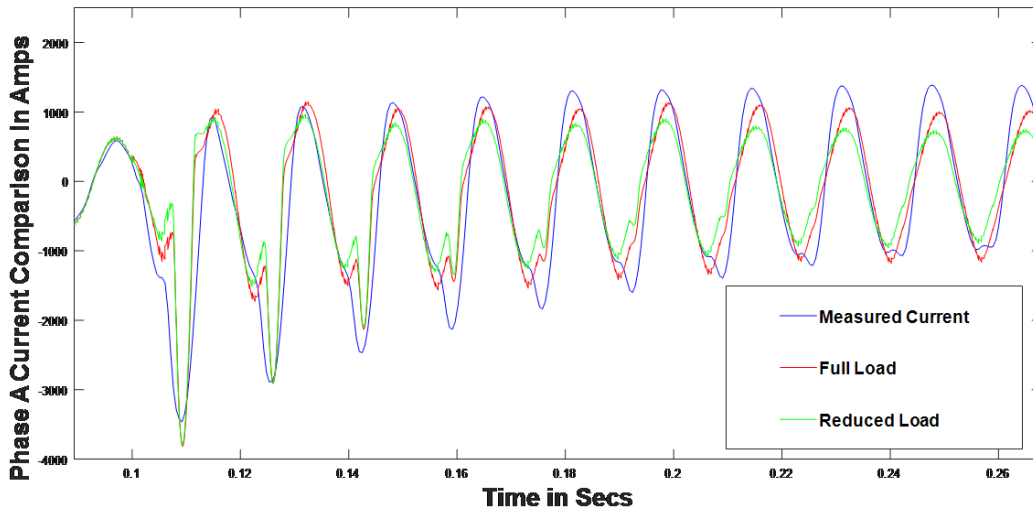


Figure 2.26: Phase-A Current Comparison for Different Load Conditions

3. Algorithmic Approach to Synthesize Feeder and Load Models Using Voltage and Current Measurements

3.1 Introduction

As discussed in Chapter 2, two standard feeder and load models, depending on their geographical location with a fixed set of feeder and load parameters, have been obtained. Although, the residential feeder and load model obtained from Case 1 (in summer conditions) has been validated in Case 2 (in winter conditions), there is no guarantee that these feeder and load models would give the best match possible between the simulated and measured current responses at the head of the feeder at any general substation. Therefore, a systematic analytical approach has been proposed in this Chapter to estimate the load composition and the load parameters of the two feeder and load models obtained from Chapter 2.

This approach has been implemented on Case 1, Case 2 and Case 4 (whose details are presented below).

Case 4 Event Details:

Event type: Phase A line to ground fault at substation K 69 kV bus.

Event time of occurrence: 10:33 AM on 8th August 2016.

Available DFR measurements: Voltages, Currents point on wave data at substation C (12.47 kV –low voltage side of the substation)

It should be noted that this approach has not been implemented on Case 3 because, as mentioned in Chapter 2, the parameters of the load didn't have much impact (almost negligible) on the simulated current responses at the head of the industrial feeder and load model in Case 3. Therefore, another case (Case 4) has been chosen for this approach, whose feeders are located in predominantly industrial and commercial areas (this information was obtained from the local utility engineers) and the event in this case is the same as in Case 1. Hence, the impact of the load parameters on the current transient responses would be significant in Case 4 and would also be useful to test the efficacy of the proposed algorithmic approach on both residential and industrial/commercial type feeder and load models.

The POW voltage measurements utilized in Case 4 is presented in Fig. 3.1 and Fig. 3.2. It should be noted that the POW voltages corresponding to the RMS voltages presented in Fig. 3.1 are played-in to the Case 4 feeder and load model.

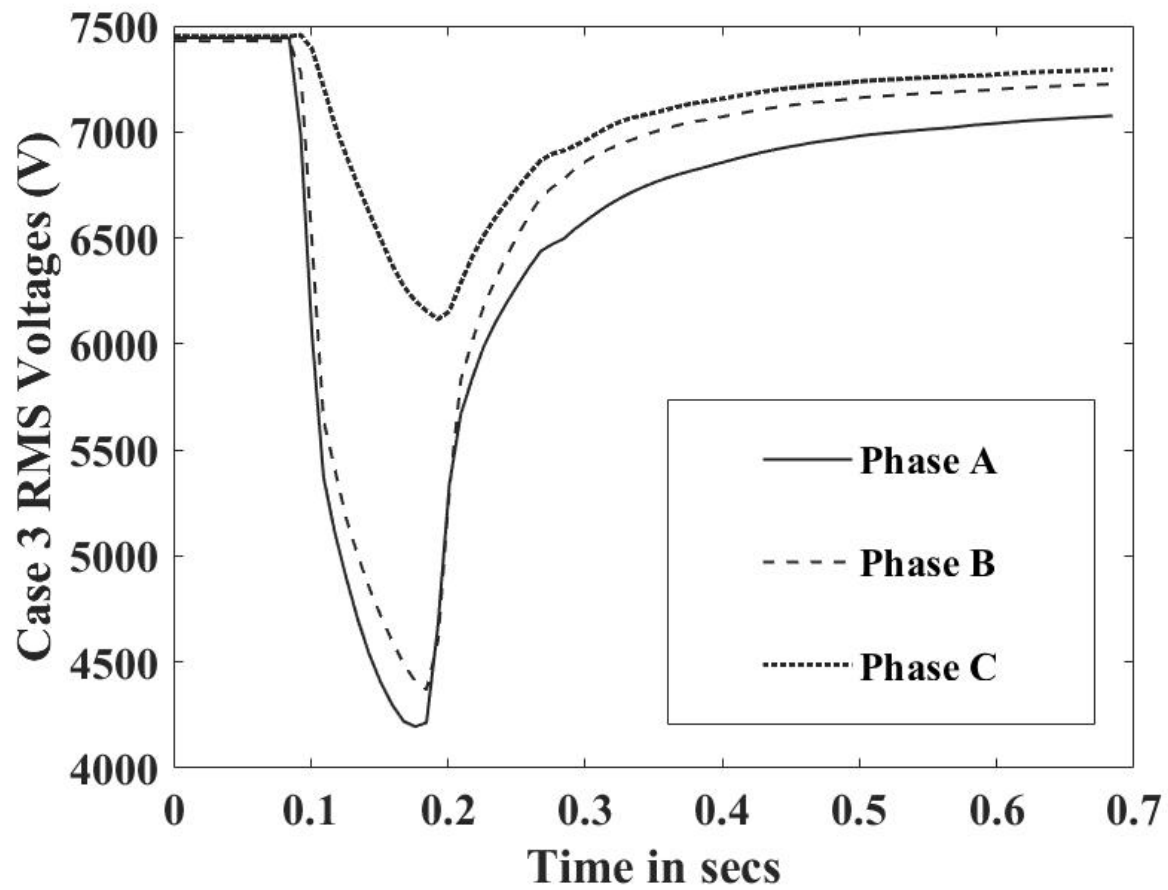


Figure 3.1: Played-in Voltage Measurements for Case 4

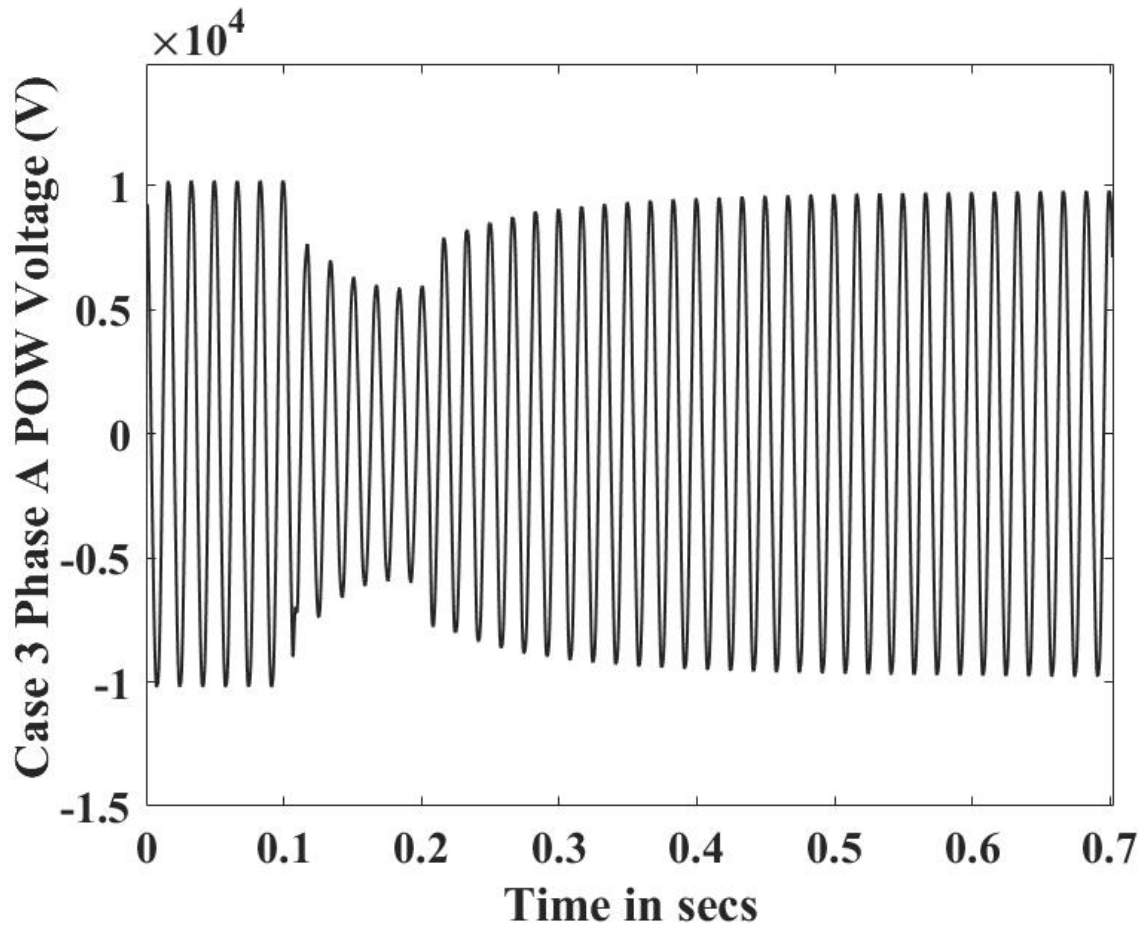


Figure 3.2: POW Played-in Phase A Voltage of Case 4

3.2 Gauss-Newton Approach: Implementation

3.2.1 Objective Function

In this work, a Gauss-Newton, non-linear least squares optimization [7] is used to determine the parameters of the motor loads and the load composition of the two feeder and load models obtained in Chapter 2. This is done by reducing the root mean square (RMS) error between the measured POW three-phase currents and simulated POW three-phase currents at the head of the feeder when three-phase POW voltage measurements are played-in to the feeder and load models. The objective function for this approach is defined as shown in (3.1):

$$\arg \min_{\mu} \mathbb{E}_{\mu}[(\mathbf{I}_m - I(\mu))^{\top}(\mathbf{I}_m - I(\mu))] \quad (3.1)$$

In (3.1), \mathbf{I}_m is the measured current vector at the head of the feeder and $I(\mu)$ is the simulated current, for a set of μ parameters, generated in PSCAD by playing-in the POW measured voltages at the head of the feeder. $E(\mu)$ is the objective function that needs to be minimized by updating the μ vector, containing parametric variables, after each iteration.

The structure of the current vectors \mathbf{I}_m and $I(\mu)$ varies according to the load model and the load composition in consideration and is discussed in detail below:

Single-phase induction motors (SPIMs): The parameters of the SPIMs of each phase are optimized with respect to its corresponding phase current individually. To compute phase A SPIM parameters, $\mathbf{I}_m = \mathbf{I}_{m_a}$ and $I(\mu) = I_a(\mu)$ are considered. Where, \mathbf{I}_{m_a} is the phase A measured current and $I_a(\mu)$ is the phase A simulated current at the head of the feeder. The same procedure is applied for phase B and phase C SPIM parameters, respectively.

Three-Phase Motors: In this case, all the three phase currents are augmented into a single vector as shown below in (3.2). This is because the change in the parameter of three-phase motors would have a significant impact on all three-phase currents at the head of the feeder.

$$[\mathbf{I}_m = \mathbf{I}_{m_a} \ \mathbf{I}_{m_b} \ \mathbf{I}_{m_c}]^{\top}, I(\mu) = [I_a(\mu) \ I_b(\mu) \ I_c(\mu)] \quad (3.2)$$

Load Composition: Similar to three-phase motors, in this case, all the three phase currents are augmented into a single vector as shown in (3.2). This is because, to obtain the load composition, the optimization procedure is applied on the ‘Scale’ parameter of three-phase motors which is dependent on all three-phase currents. More description about the ‘Scale’ parameter has been presented in the later sections of this Chapter.

3.2.2 Jacobian, Step length and Parameter Updates

The considered Gauss-Newton approach is applied to one parameter at a time for the SPIMs and the three phase motors using (3.3), (3.4) and (3.5). It should be noted that representing

simulated currents and the measured currents by an analytical function is not possible for this work. This is because these currents are in the form of sinusoidal waves with a transient that is difficult to represent as an analytical function. Therefore, the first order differential Jacobian function has been calculated numerically by calculating the first order forward difference as shown in (3.3).

$$J(\mu_0) = \frac{I(\mu_0 + \beta) - I(\mu_0)}{\beta} \quad (3.3)$$

Where, $J(\mu_0)$ is the Jacobian column vector corresponding to parameter μ_0 , whose dimension is the number of samples of the measured current. β is a small perturbation value whose value is chosen for each parameter accordingly using engineering judgement. Values such as 0.05, 0.2 and 0.4 are found to be good choices for β .

Additionally, backward difference and central difference methods have been tested, in this work, to compute the Jacobian vector numerically. However, these methods did not significantly change or improve the results of this algorithm when compared to the forward difference method.

The increment in parameter μ_0 , at each iteration is evaluated using (3.4).

$$\Delta\mu_0 = (J^T J)^{-1} J^T (\text{Im} - I(\mu_0)) \quad (3.4)$$

Where, J is the Jacobian vector obtained from (3.3).

Another important feature, along with the search direction, to consider in this approach is the step length of the update of the parameters at each step. The parameters, at the end of each iteration, are updated using (3.5).

$$\mu_{\text{final}} = \mu_{\text{prev}} + \alpha \Delta\mu_0 \quad (3.5)$$

Where, μ_{final} is the new parameter obtained at the end of the iteration, μ_{prev} is the value of the parameter from previous iteration, α is the step length and $\Delta\mu$ is obtained from (3.4). Typical values of α used in this work are 0.25, 0.5 and 1.

3.2.3 Choosing Parameter Bounds

While implementing this algorithm, it is important that appropriate bounds are considered for the parameters of the motor models to ensure that the parameters obtained after convergence are realistic. The upper and lower bounds considered for SPIMs and three-phase motors are shown in Table 3.1 and Table 3.2. A voltage behind reactance (VBR) based dual-rotor squirrel cage induction motor model has been considered in this work to represent the three-phase motors.

The bounds of SPIM parameters, as shown in Table 3.1, are obtained using the following criteria:

- Efficiency of SPIM is assumed to be between 90-95%
- Total motor losses at the rated conditions are calculated for the assumed efficiency range.

- Copper losses are assumed to be 60% of the total losses (25% stator copper losses and 35% copper rotor losses).
- Typically, combination of stator reactance and rotor reactance is approximately equal to the sub-transient reactance of the motor. Additionally, sub-transient reactance is usually in the range of 5% - 15% for a SPIM. Using this assumption, the bounds on rotor and stator reactances has been chosen in this work.

Table 3.1: SPIM Parameter Bounds

Parameter	Lower Bound	Upper Bound
Rotor Resistance	0.3 ohm	0.6 ohm
Inertia Constant	0.0313 s	0.1 s
Stator Resistance	0.2 ohm	0.4 ohm
Rotor Reactance	0.3 ohm	0.7 ohm
Stator Reactance	0.3 ohm	0.7 ohm

Table 3.2: Three-Phase Motor Parameters Bounds

Parameter	Lower Bound	Upper Bound
Inner Rotor Resistance	0.002 pu	0.02 pu
Outer Rotor Resistance	0.1 pu	0.2 pu
Inertia Constant	0.1 s	0.35 s
Stator Resistance	0.002 pu	0.05 pu
Inner Rotor Reactance	0.05 pu	0.2 pu
Outer Rotor Reactance	0.05 pu	0.25 pu
Stator Reactance	0.05 pu	0.15 pu

The SPIM's considered in this work are used to represent the air-conditioner compressor motors which have very small inertia. Therefore, 6 cm – 8 cm bounds on rotor diameter has been chosen to represent small induction motors in the air conditioners. The inertia constant values corresponding to the chosen rotor diameter bounds are presented in Table 3.1.

There are several references available in the literature that provide the parameters of the three-phase motors. Using [8] and [9], the bounds in Table 3.2, for a 460 V dual rotor three-phase induction motor [10], has been chosen in this work.

It is also important to have bounds on the load composition distribution between the three-phase motor load and the SPIM load. The following points are used to choose the bounds on the load composition of the loads:

1. The constraint used in this approach is that the total load is always comprised of 90% of motor load and 10% impedance load.

2. The optimization approach is applied on the scale parameter of 3PHIM's ('Scale1') which is defined as follows:

- If 'Scale' = 1 for 3PHIM, it corresponds to 3PHIM consuming 50 kVA.
- Similarly, If 'Scale' = 1 for SPIMs, then it corresponds to 3PHIM consuming 3.83 kVA.
- For Example: $\text{Scale1} \cdot 0.05 + \text{Scale2} \cdot 0.00383 = 2.17 \text{ MVA}$ (in Phase A of Case 2), where, 'Scale1' corresponds to 3PHIMs and 'Scale2' corresponds to SPIMs. Similarly, 0.05 corresponds to the rating of the three-phase motors (50 kVA) and 0.00383 corresponds to the rating of the single-phase motors (3.83 kVA)

3. Therefore, the bounds on the 'Scale 1' are calculated for each case based on the following distribution between the three-phase motor load and the SPIM load:

- Upper bound on three-phase motor load: 85%
- Lower bound on three-phase motor load: 5%

3.2.4 Implementing Parameter Bounds

The bounds on the considered parameters cannot be applied as a hard constraint in the Gauss-Newton algorithm. The bounds are implemented, in an interactive environment consisting of a Fortran script and PSCAD, in this work. Therefore, the logit transformation has been used in this paper to implement bounds on the parameters. In this transformation, the parameter of interest with bounds, is transformed into a new parameter with no bounds using (3.6) as shown below.

$$\Omega_0 = \log\left(\frac{\mu_0 - \mu_{0,\text{lower bound}}}{\mu_{0,\text{upper bound}} - \mu_0}\right) \quad (3.6)$$

Where, μ_0 is the original parameter, $\mu_{0,\text{lower bound}}$ is the lower bound of the original parameter, $\mu_{0,\text{upper bound}}$ is the upper bound of the original parameter and Ω_0 is the new transformed parameter and has limits $(-\infty, +\infty)$.

After the transformation, (3.1) becomes a function of Ω (vector of transformed parameters) as shown in (3.7), which is free of the bounded constraints on the parameters.

$$\arg \min_{\Omega} \mathbb{E}_{\Omega}[(\text{Im} - I(\mu))^T (\text{Im} - I(\mu))] \quad (3.7)$$

After the convergence criterion is met, the transformed parameter vector Ω is transformed back to the original parameter vector μ using (3.6).

3.2.5 Convergence Criterion

The main objective of this work is to obtain a close match between the measured currents and the simulated currents. Hence, a small tolerance for the difference in parameters between two

consecutive iterations has been chosen as the convergence criterion as shown in (3.8).

$$\Omega_k - \Omega_{k-1} < 10^{-2} \quad (3.8)$$

Where, Ω_k is the transformed parameter in the current iteration k and Ω_{k-1} is the transformed parameter in the previous iteration k-1. The convergence criterion used in (3.8) is equivalent to having a tolerance of less than 10^{-3} for the original parameter μ_0 between two successive iterations.

3.3 Results and Discussion

An interactive setup comprising of PSCAD (generates simulated currents) and a Fortran script (conducts the optimization procedure) has been implemented in this work. The flow chart describing this process has been presented in detail in Fig. 3.3.

In this algorithmic approach, it is important to have a good initial estimate of the parameters of SPIMs and three-phase motors as mentioned in Chapter 2. The parameters of SPIMs and three-phase motors that are obtained using the manually tuned technique in Chapter 2, for the same considered feeder and load models in this work are used as the initial values in this work as shown in Table 2.2 and Table 2.7. Similarly, the final load compositions obtained for the residential feeder and load model (from Case 1 and Case 2 in Chapter 2) and the final load compositions obtained for the industrial feeder and load model (from Case 3 in Chapter 2) are used as the initial conditions to estimate the load composition using the Gauss-Newton algorithm.

Based on the sensitivity analysis conducted in Chapter 2, the order of parameters given (from top to bottom) for SPIMs and three-phase motors, in (2.2) are used to conduct the optimization procedure in this work.

As mentioned earlier, a residential feeder and load model has been considered for Case 1 and Case 2 whose load is predominantly single-phase motor load. However, an industrial and commercial feeder and load model has been considered for Case 4 which is mainly comprised of three-phase motor loads. Therefore, in Case 1 and Case 2, the proposed optimization procedure has been applied initially to the SPIM parameters assuming SPIMs would have the most impact on the total current at the head of the feeder. After updating the SPIM parameters with their converged optimized parameters, the optimization procedure has been implemented for three-phase motor 'Scale' parameter. However, for Case 4, the optimization approach is first applied to the three-phase motors and then the single-phase motors due to the dominant presence of the three-phase motor loads in the considered industrial feeder and load model before applying the optimization approach to estimate the load composition of the feeder and load model.

It should be noted that once the converged parameters are obtained for all the loads, in the order mentioned above, the optimization procedure is implemented to estimate the load composition in Case 1, Case 2 and Case 4.

The final converged parameters of the SPIM for Case 1, Case 2 and Case 4 is presented in Table 3.3, Table 3.4 and Table 3.5 respectively.

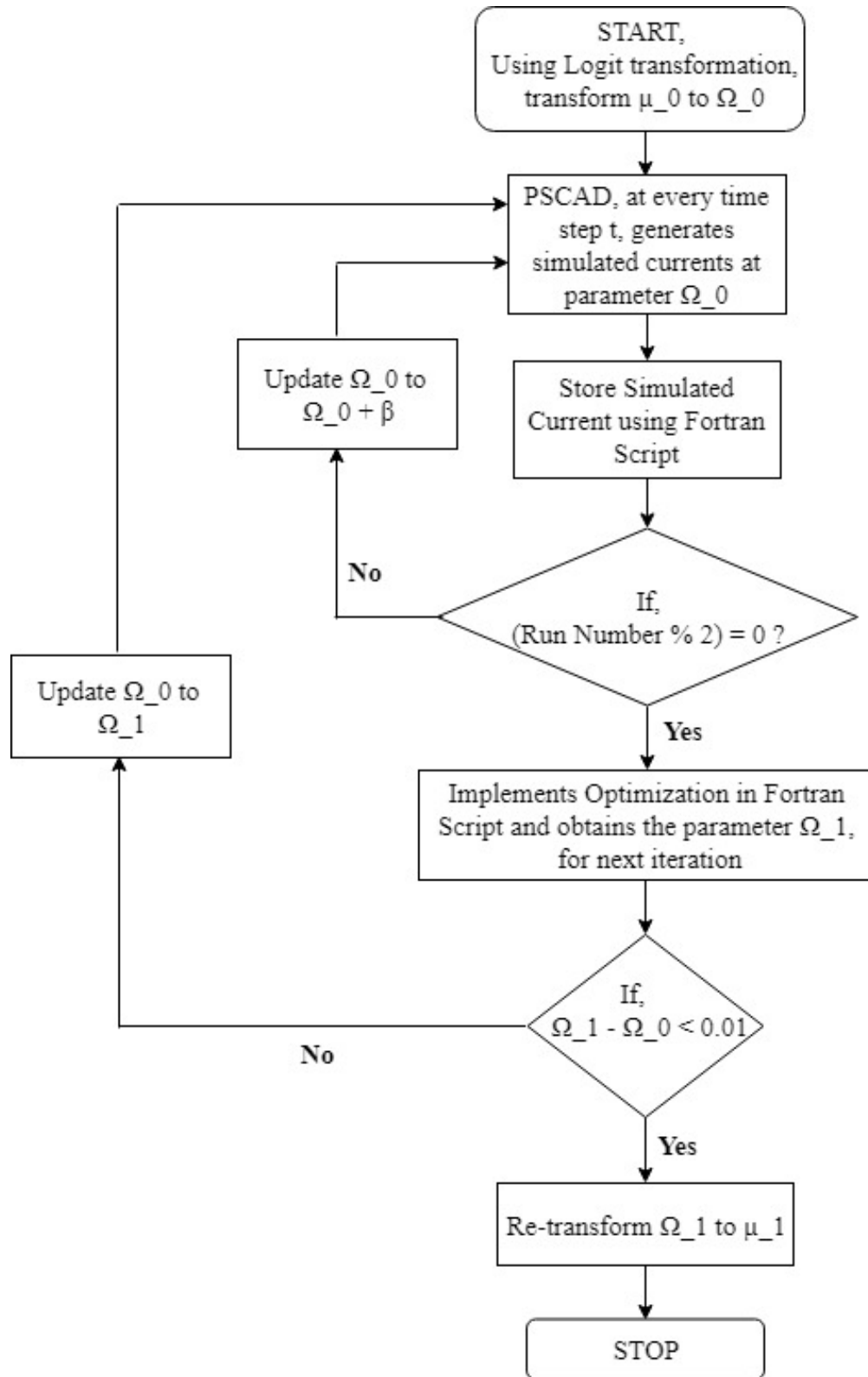


Figure 3.3: Flow Chart Describing the Optimization Process Implemented in PSCAD and the Fortran Script

Table 3.3: Final SPIM Parameters for Case 1

Parameter	Phase A	Phase B	Phase C
Rotor Resistance	0.487 ohm	0.6 ohm	0.531 ohm
Inertia Constant	0.066 s	0.086 s	0.044 s
Stator Resistance	0.297 ohm	0.2 ohm	0.2 ohm
Rotor Reactance	0.408 ohm	0.416 ohm	0.3 ohm
Stator Reactance	0.653 ohm	0.62 ohm	0.61 ohm

Table 3.4: Final SPIM Parameters for Case 2

Parameter	Phase A	Phase B	Phase C
Rotor Resistance	0.6 ohm	0.577 ohm	0.52 ohm
Inertia Constant	0.058 s	0.057 s	0.054 s
Stator Resistance	0.289 ohm	0.2 ohm	0.4 ohm
Rotor Reactance	0.497 ohm	0.7 ohm	0.3 ohm
Stator Reactance	0.6 ohm	0.7 ohm	0.443 ohm

Table 3.5: Final SPIM Parameters for Case 4

Parameter	Phase A	Phase B	Phase C
Rotor Resistance	0.385 ohm	0.436 ohm	0.6 ohm
Inertia Constant	0.1 s	0.053 s	0.065 s
Stator Resistance	0.4 ohm	0.4 ohm	0.3 ohm
Rotor Reactance	0.479 ohm	0.309 ohm	0.3 ohm
Stator Reactance	0.6 ohm	0.61 ohm	0.3 ohm

The final converged parameters for the three-phase motors for Case 1, Case 2 and Case 4 are shown in Table 3.6.

Table 3.6: Final Three-Phase Motor Parameters for Case 1, Case 2 and Case 4

Parameter	Case 1	Case 2	Case 4
Inner Rotor Resistance	0.02 pu	0.002 pu	0.02 pu
Outer Rotor Resistance	0.2 pu	0.2 pu	0.2 pu
Inertia Constant	0.1 s	0.1 s	0.35 s
Stator Resistance	0.048 pu	0.015 pu	0.045 pu
Inner Rotor Reactance	0.171 pu	0.2 pu	0.2 pu
Outer Rotor Reactance	0.226 pu	0.05 pu	0.05 pu
Stator Reactance	0.065 pu	0.119 pu	0.15 pu

From Table 3.6, it is observed that the final obtained inertia parameter for the three-phase motors are low for Case 1 and Case 2 and much higher for Case 4. This is to be expected because the three-phase motors in a typical industrial area are much larger compared to the three-phase motors present in residential areas.

In Table 3.7, the final load compositions obtained for all the cases are presented. It can clearly be observed that the amount of three-phase motor load is much higher in Case 4 when compared to the single-phase motor load in an industrial/commercial area which is to be expected. Similarly, for Case 1 and Case 2, the single-phase motor load is much higher when compared to three-phase motor load for the residential feeder and load model.

Table 3.7: Final Load Composition for Case 1, Case 2 and Case 4

	Three-Phase Motor Load	Single-Phase Motor Load	Impedance Load
Initial Condition (Case 1 and Case 2)	18%	72%	10%
Initial Condition (Case 4)	65%	25%	10%
Case 1 (after optimization)	26%	64%	10%
Case 2 (after optimization)	35%	55%	10%
Case 4 (after optimization)	69%	21%	10%

While optimizing the SPIM parameters, the error between the measured currents and the simulated currents reduces phase by phase as shown in Table 3.8. However, as discussed earlier, while optimizing the three-phase motor parameters all the three phase currents are augmented into a single vector in (3.2). The reduction of RMS error per sample for this single current vector using this approach is presented in Table 3.9.

Table 3.8: Effectiveness of the Optimization Approach When Optimizing SPIM Parameters

Phase	Test Case	RMS Error per sample (with initial values of parameters)	RMS Error per sample (after optimizing parameters)	Improvement
A	Case 1	161.87	144.68	+ 11%
B	Case 1	140.25	119.38	+ 15%
C	Case 1	97.03	87.64	+ 10%
A	Case 2	74.23	61.9	+ 17%
B	Case 2	77.57	69.74	+ 10%
C	Case 2	35.82	35.45	+ 1%
A	Case 3	143.29	111.78	+ 22%
B	Case 3	155.9	153.3	+ 2%
C	Case 3	177.38	173.20	+ 2%

Table 3.9: Effectiveness of the Optimization Approach When Optimizing Three-Phase Motor Parameters for Overall Current Vector

Test Case	RMS Error per sample (with initial values of parameters)	RMS Error per sample (after optimizing parameters)	Improvement
Case 1	184.99	145.67	+ 22%
Case 2	59.36	58.23	+ 2%
Case 3	220.58	159.51	+ 28%

In Table 3.10, the total decrease of the RMS error per sample between the measured currents and the simulated currents after applying the optimization approach to all the motor loads (both parameters and composition) is presented in detail. It can be observed that the proposed optimization approach has made the maximum impact on Case 4 currents. Although, in Case 1 and Case 4, the same SLG fault event at 69 kV level is considered, and both the cases have very close pre-fault nominal currents, this approach seems to work more efficiently on the industrial feeder and load model (Case 4) with pre-dominantly three-phase motor loads when compared to the residential feeder and load model (Case 1) with pre-dominantly SPIM loads. Additionally, in Chapter 2, the same set of parameters (initial values in this work for all three cases) of the motor load models are manually tuned in such a way that a good fit is obtained between the measured currents and the simulated currents in Case 1 and Case 2. The parameters of loads obtained in those cases have not been tuned by considering Case 4. This could be another factor contributing to major improvement of currents in all three phases in Case 4 using the proposed optimization procedure.

Table 3.10: Effectiveness of the Optimization Approach after Optimizing all the Load Parameters and ‘Scale’ Parameter

Phase	Test Case	RMS Error per sample (with initial values of parameters)	RMS Error per sample (after optimizing parameters)	Improvement
A	Case 1	161.87	100.2	+ 38%
B	Case 1	140.25	121.81	+ 13%
C	Case 1	97.03	89.85	+ 7%
A	Case 2	74.23	58.54	+ 20%
B	Case 2	77.57	65.72	+ 16%
C	Case 2	35.82	35.1	+ 2%
A	Case 3	161.17	107.98	+ 33%
B	Case 3	215.15	154.49	+ 30%
C	Case 3	273.56	172.15	+ 38%

In Fig. 3.4, Fig. 3.5 and Fig. 3.6 the comparison of the three-phase simulated currents with their corresponding measured currents, at the head of the feeder, has been presented for Case 4. These plots demonstrate the qualitative improvement in the matching of simulated currents with their respective measured currents when the optimization algorithm is employed to estimate the parameters of the load models.

In Fig. 3.4, Fig. 3.5 and Fig. 3.6, when the fault occurs, at the 20000th sample, and when the fault is cleared, at the 40000th sample, it can be observed that there is a significant improvement in the simulated current response in all three phases when the optimization approach is used. However, in the steady state, after 70000 samples, there does not seem to be much impact of the optimization algorithm on the simulated current responses. This is to be expected because parameters such as rotor resistance and motor inertia have a significant role on the transient response during a fault and after a fault is cleared respectively. However, in steady state, the impact of parameter sensitivity is much less pronounced.

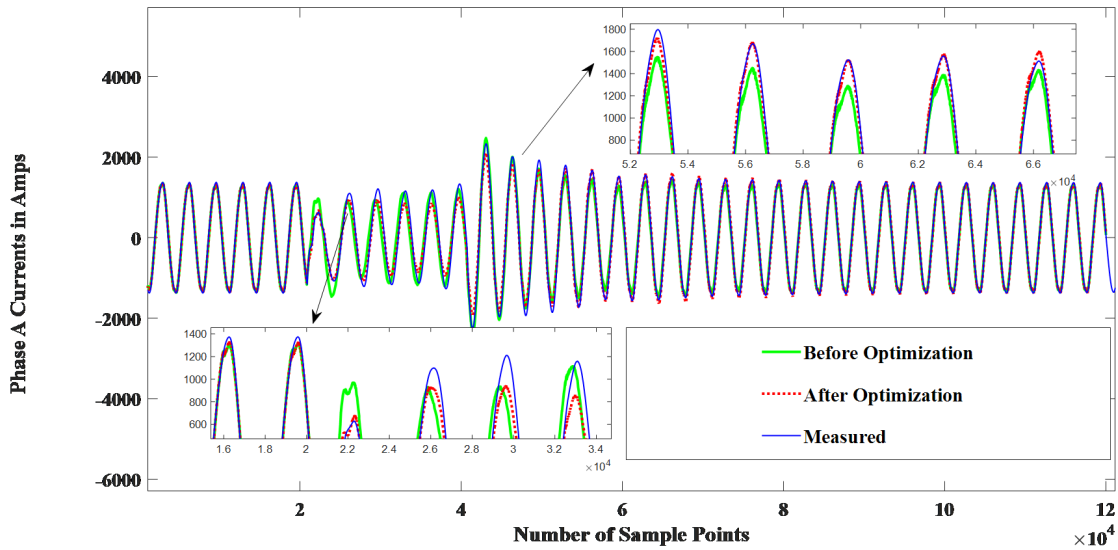


Figure 3.4: Impact of Optimization Approach on Phase A Current of Case 4

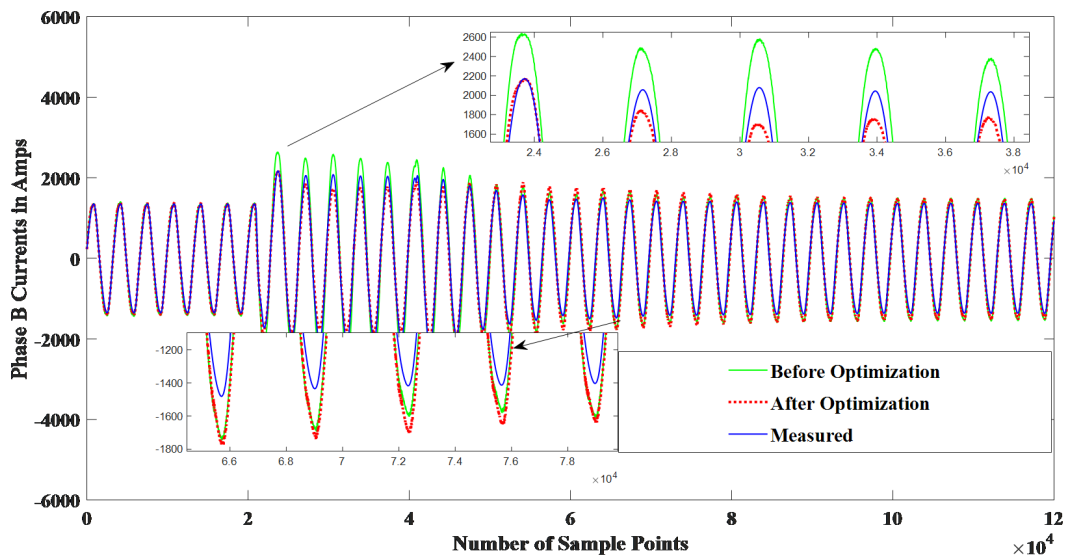


Figure 3.5: Impact of Optimization Approach on Phase B Current of Case 4

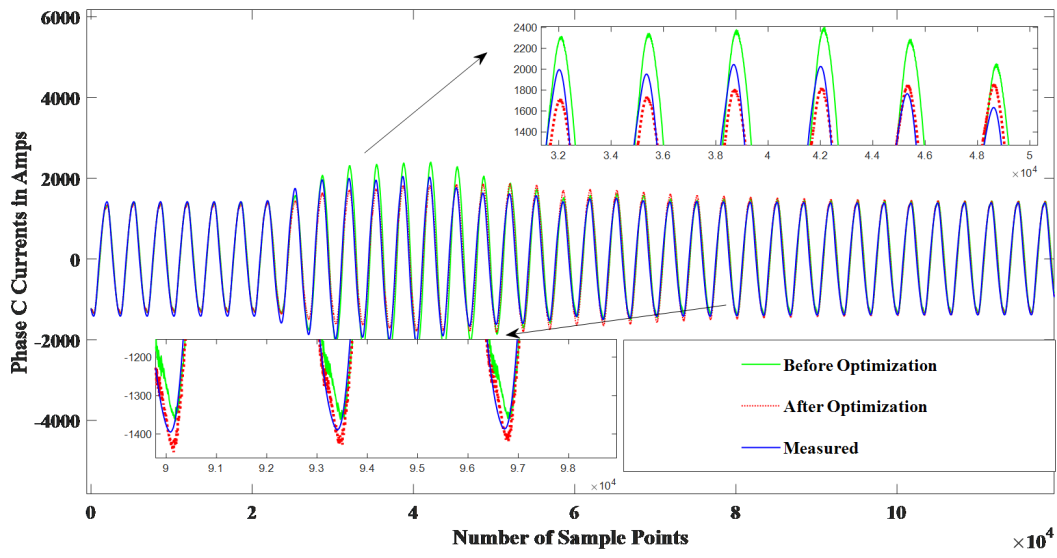


Figure 3.6: Impact of Optimization Approach on Phase C Current of Case 4

4. Application of Synthesized Feeder and Load Models in Positive Sequence Software Packages

4.1 Introduction

The feeder and load models developed in Chapter 2 and Chapter 3 can be utilized only in EMTP environment software packages to analyze the power system. However, in the planning studies [11] the positive sequence software packages such as PSLF [12], PSSE [13] are used to conduct the simulations on the bulk power system. Therefore, in this Chapter, an application of the synthesized three-phase feeder and load models in the PSLF environment has been presented in detail.

Efforts have been made, in this work, to study the impact of playing-in the voltage measurements of Case 1 and Case 2 into the load models of PSLF. Based on the simulations conducted, it was observed that the SPIM stalling phenomenon that was observed in Case 1 (in Chapter 2) in a FIDVR type event, is not captured in the PSLF simulations. Therefore, the main objective of this chapter is to present a systematic approach to estimate SPIM stalling in PSLF for fault type events.

4.2 PSLF Simulations

4.2.1 Positive Sequence Voltage Generation

To conduct the feeder and load model studies in PSLF, the three-phase measured voltages from Case 1 and Case 2 are transformed into their respective positive sequence voltages by calculating their d-q components, using Park's transformation in 'Matlab'. It should be noted that these measured three-phase voltages are not perfectly balanced in all conditions (pre-fault, during the fault and post-fault). This unbalance between the three-phase voltages leads to a 120 Hz component, within the positive sequence voltages calculated from 'Matlab', which would not be captured by the PSLF (it only captures the 60 Hz voltage component). Therefore, a first order low pass filter has been used to filter out the 120 Hz component in the evaluated positive sequence voltages in Case 1 and Case 2.

The positive sequence voltages obtained for Case 1, without filtering the 120 Hz component and with filtering the 120 Hz component are presented in Fig. 4.1 and Fig. 4.2 respectively.

Similarly, the positive sequence voltages obtained for Case 2, without filtering the 120 Hz component and with filtering the 120 Hz component are presented in Fig. 4.3 and Fig. 4.4 respectively.

The voltages obtained in Fig. 4.2 and Fig. 4.4 are played-in to a positive sequence feeder and load model (whose details are mentioned in detail in the next sub-section of this chapter) in PSLF. It should also be noted that the voltage nadir in Fig. 4.2 (Case 1) is significantly lower

compared to the voltage nadir in Fig. 4.4 (Case 2). Similarly, the time taken for the post-fault voltage to reach the nominal voltage is much higher in Case 1 when compared to Case 2. This is to be expected because Case 1 is a severe FIDVR type event whereas Case 2 is a much less severe non-FIDVR type event.

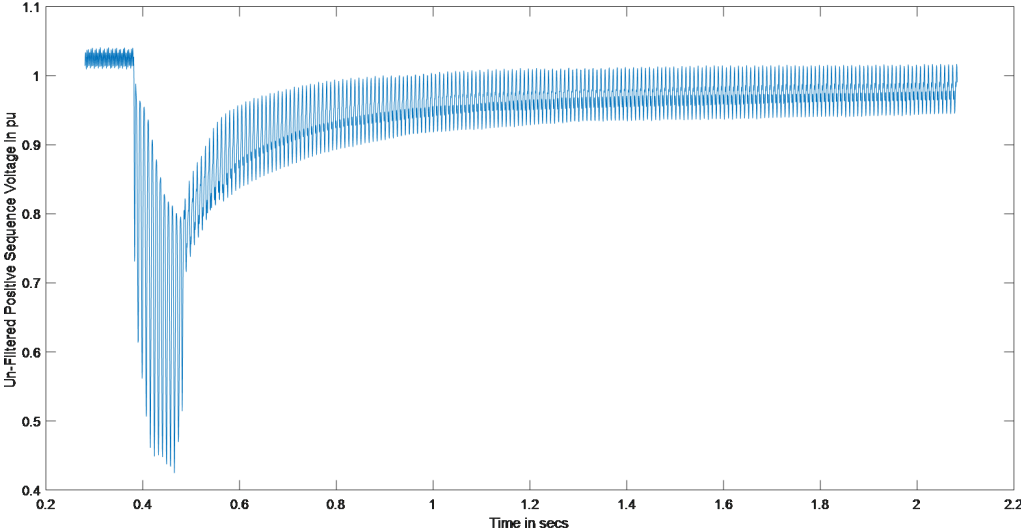


Figure 4.1: Un-Filtered Positive Sequence Voltage Obtained for Case 1

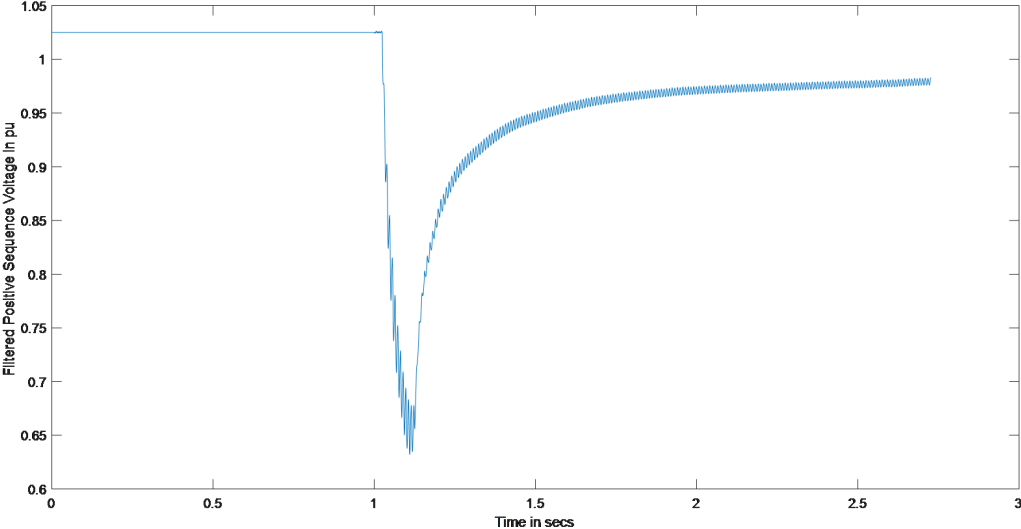


Figure 4.2: Filtered Played-in Positive Sequence Voltage Obtained for Case 1

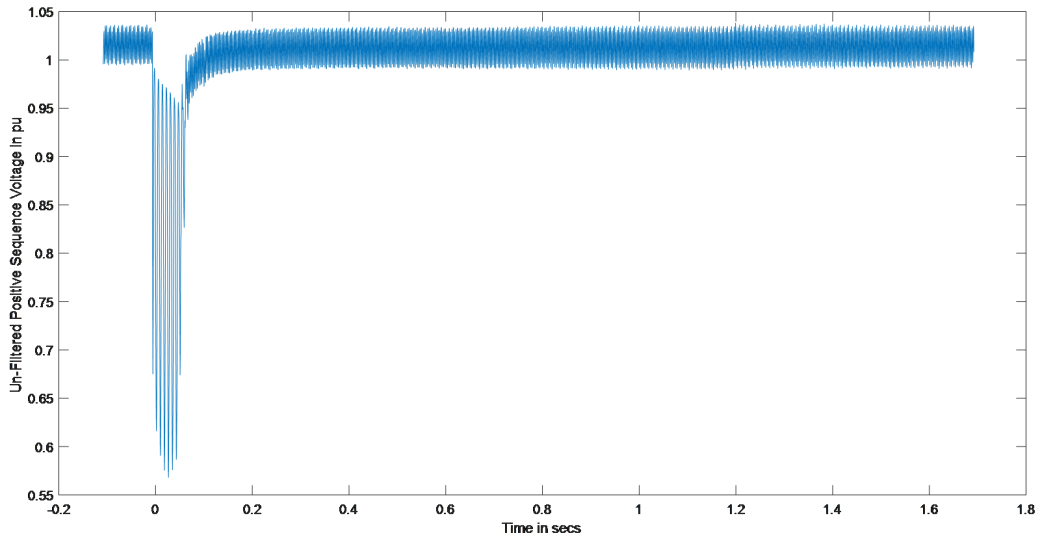


Figure 4.3: Un-Filtered Positive Sequence Voltage Obtained for Case 2

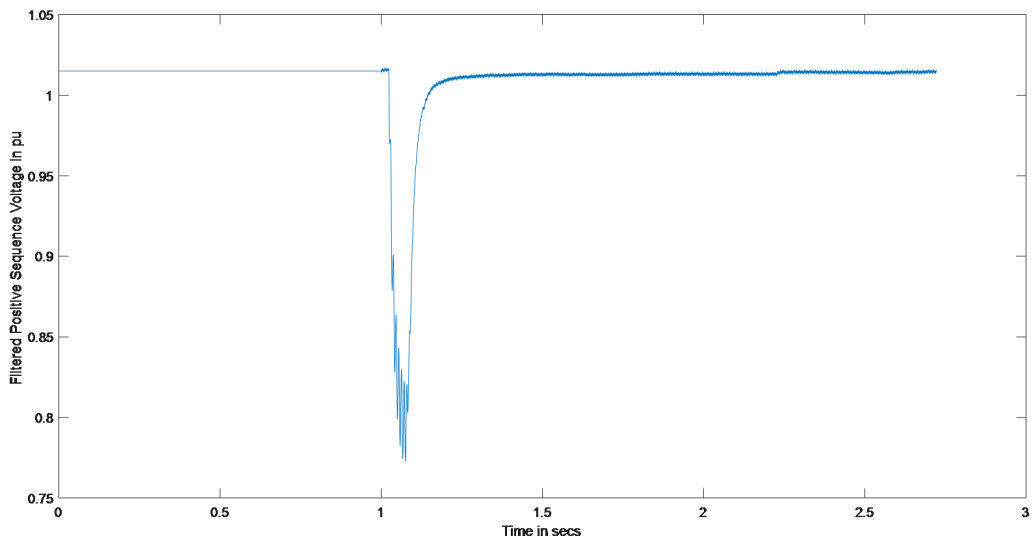


Figure 4.4: Filtered Played-in Positive Sequence Voltage Obtained for Case 2

4.2.2 Feeder and Load Models in PSLF

It is important to accurately represent the SPIMs and three-phase motors, used in the EMTP type simulations, in PSLF feeder and load models. Therefore, ‘Motor1’ model [12] is used to represent three-phase motors. The type ‘D’ SPIM model in PSLF [12] is a performance-based model which is made up of a set of algebraic equations to estimate if the motor stalls or not depending on the voltage at its terminals. Therefore, a user-defined custom built ‘Motorc’ [12] model is used to represent the SPIMs in PSLF. It should be noted that unlike, the type ‘D’ motor model in composite load model ‘Cmpldw’, the ‘Motorc’ is a differential equations-based model which is equivalent to a set of balanced number of SPIMs in all three phases.

The comparison of active power plots and reactive power plots at the head of the feeder when positive sequence voltages generated for Case 1 are played-in to ‘Motor1’ and ‘Motorc’ loads separately, with their corresponding measured values are presented in Fig. 4.5, Fig. 4.6. Similarly, the corresponding plots for Case 2 are presented in Fig. 4.7 and Fig. 4.8 respectively.

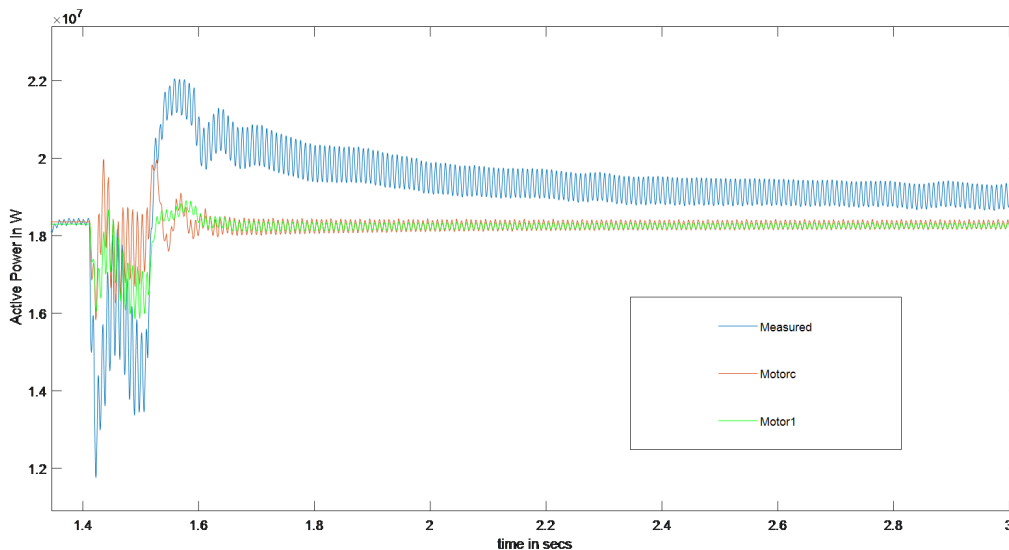


Figure 4.5: Active Power Comparison for Case 1

From Fig. 4.5 and Fig. 4.6, it can be seen that both ‘Motorc’ and ‘Motor1’ load models seems to produce a good match between the transient response in the simulated P (active power) and simulated Q (reactive power) and their corresponding measured responses. However, in the post-fault steady state, both measured P and measured Q values are much higher compared to their corresponding simulated values. Additionally, the post-fault P and Q simulated values are same as their corresponding pre-fault simulated values. This clearly indicates that even at 100% motor load penetration in the feeder model, the motors (both SPIMs and three-phase motors) in PSLF do not stall for this FIDVR type event. This phenomenon can be clearly seen in Fig. 4.9 where the motors do not stall and re-accelerate to their nominal speed after the fault is cleared at 1.2 secs. At this 100% penetration level of motors, the parameters of the motors for both ‘Motor1’ and ‘Motorc’ are manually tuned to check if they would stall for Case 1 played-in voltages. However, in all the scenarios it was observed that the motors

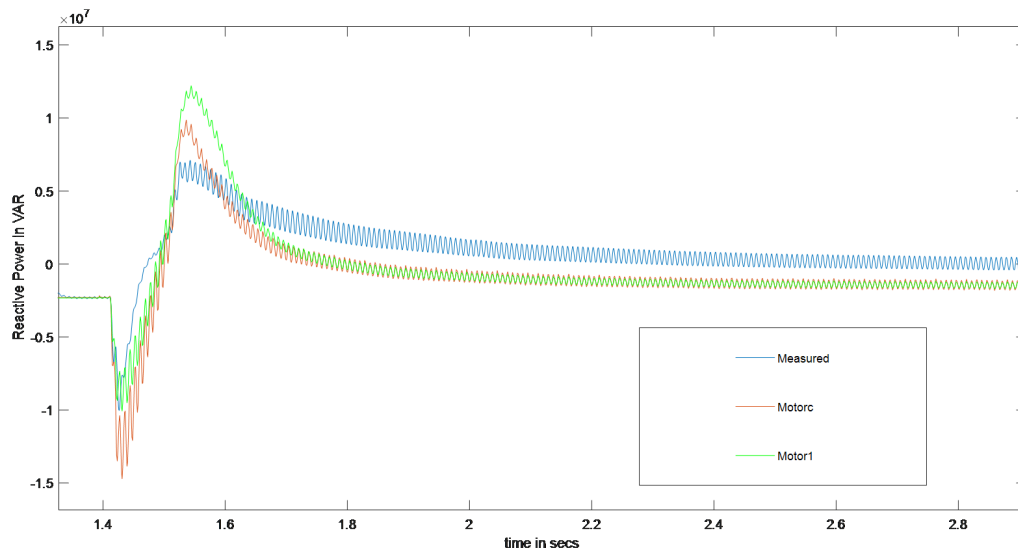


Figure 4.6: Reactive Power Comparison for Case 1

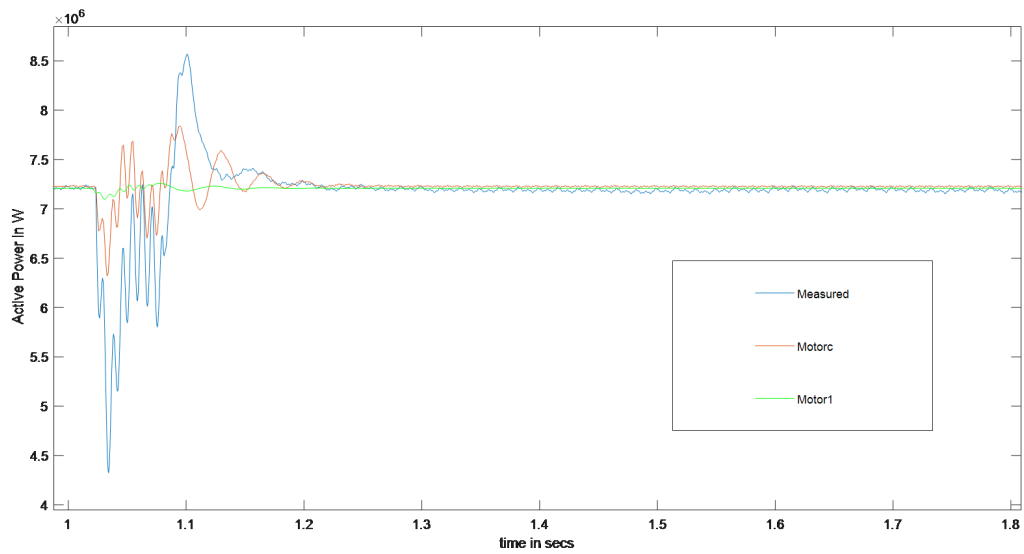


Figure 4.7: Active Power Comparison for Case 2

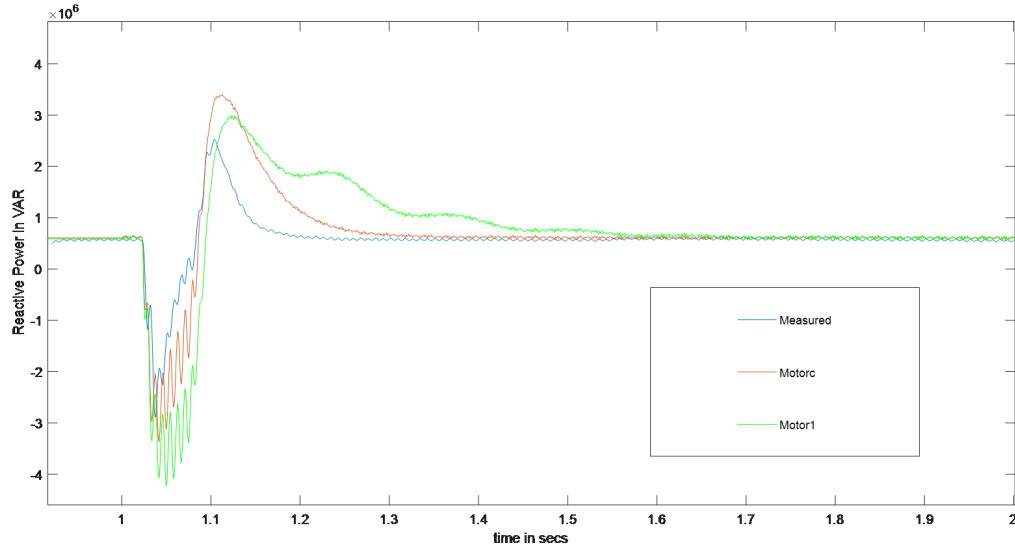


Figure 4.8: Reactive Power Comparison for Case 2

would not stall. This is to be expected as the PSLF does not capture the unidirectional component of the SPIM current that occurs at the time of the fault. This unidirectional component of the current is dependent on the point on the voltage wave (at the terminals of the motor) at which the fault is initiated. However, the POW phenomenon is not captured in PSLF. Therefore, it is important to develop an approach to predict motor (SPIM) stalling in PSLF for FIDVR type events.

Similarly, from Fig. 4.7 and Fig. 4.8 it can be seen that both ‘Motorc’ and ‘Motor1’ load models seems to produce a good match between the transient response in the simulated P (active power) and simulated Q (reactive power) and their corresponding measured responses during the fault and after the fault is cleared (during post-fault steady state condition). This is to be expected because as mentioned in Chapter 2, Case 2 is a less severe fault event (compared to Case 1) and no SPIM stalling was observed for this case in PSCAD. This phenomenon is also captured in Fig. 4.10 where both the motors (‘Motor1’ and ‘Motorc’) do not stall.

4.3 Regression Model to Predict SPIM Stalling in PSLF

As discussed in the previous section, positive sequence software packages such as PSLF do not capture the point on wave effects which is essential to capture the SPIM stalling phenomenon in a FIDVR type event such as Case 1. Therefore, a multi-variable linear regression model has been developed to predict SPIM stalling and has been presented in detail in this section. The following steps are used to develop this regression model:

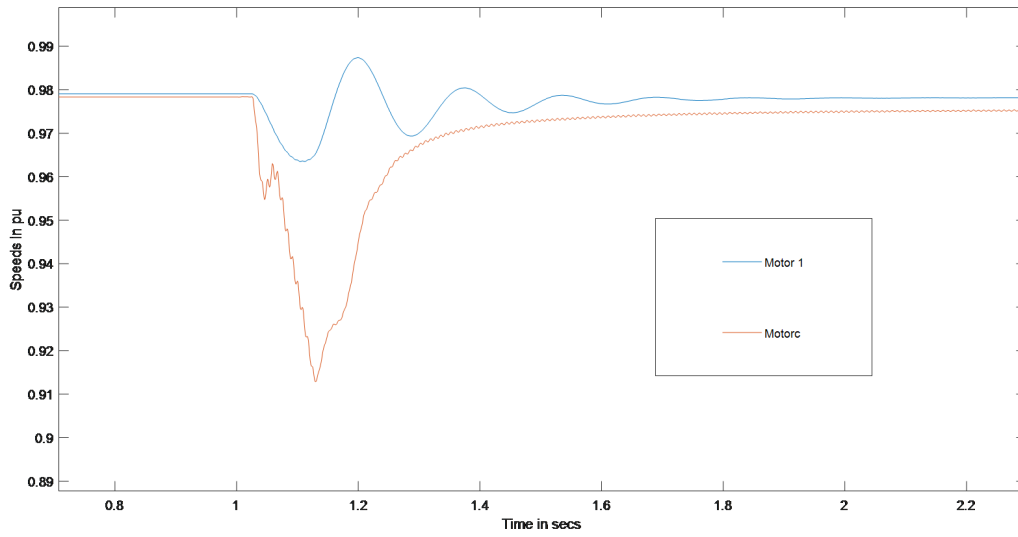


Figure 4.9: Motor Speeds Comparison for Case 1

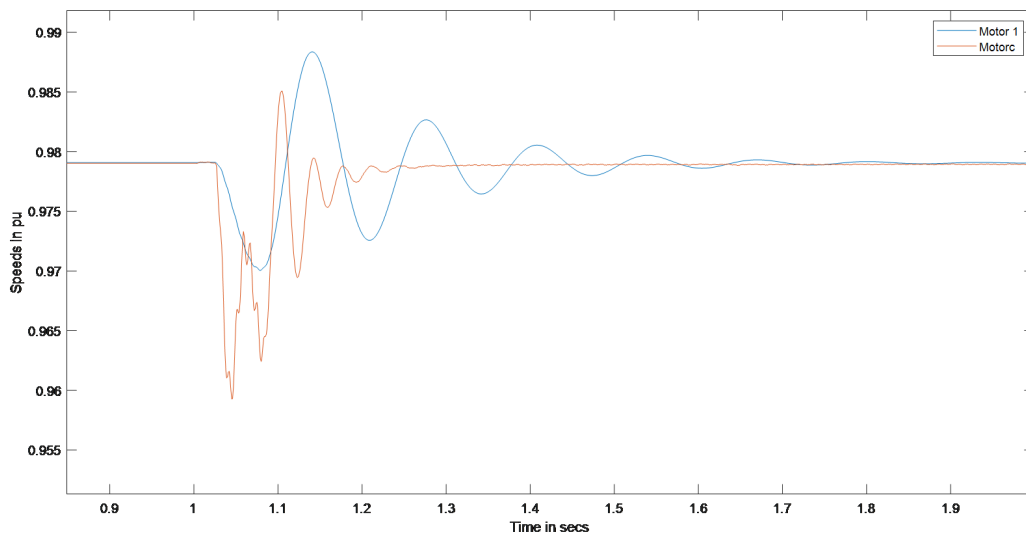


Figure 4.10: Motor Speeds Comparison for Case 2

4.3.1 Step 1: Generate Random Test Cases in PSCAD

The test cases (SLG phase A faults) to train and test the regression model has been generated in PSCAD. As mentioned earlier in this report, PSCAD captures the POW effects accurately and hence the SPIM stalling phenomenon, for severe SLG fault events such as FIDVR, would also be captured accurately. The schematic of the circuit used to generate these test cases are presented in Fig. 4.11.

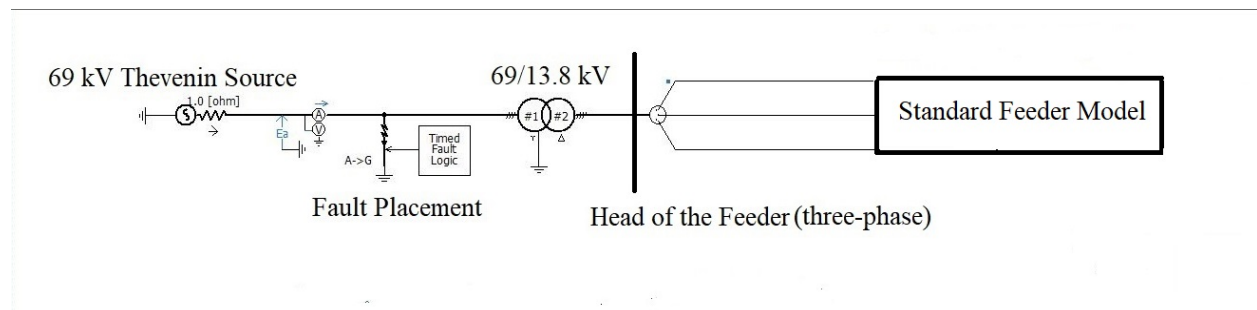


Figure 4.11: Circuit Schematic in PSCAD to Generate the Test Cases

It should be noted that the standard feeder model used in Fig. 4.11 is represented by the residential feeder and load model that is obtained, from Chapter 3 (for Case 1), after applying the optimization procedure to estimate the load composition and the load parameters.

The test cases in this work are generated by using a random sequence of following critical parameters of a SLG fault:

- Fault Resistance (R): This parameter directly impacts the voltage nadir at the location of the fault. For example, a high fault resistance would lead to a low voltage nadir and hence the system would be less impacted.
- Fault Duration (α): This parameter represents the duration in which the system is affected due to the fault.
- Point of initiation on the Sine wave (β): This parameter is useful to represent the impact of placing the fault on different points on a sine wave. For example: A fault placed at a voltage zero on the sine wave is a much more severe event than when it is placed on any other point on the sine wave.

In total, two different case sets have been generated depending on the location of the SLG fault as shown below:

- Case Set 1: Sub-transmission Faults (120 test cases)
- Case Set 2: Transmission Faults (120 test cases)

The primary difference between Case set 1 and Case set 2 is that the time required to clear the fault (α) is much faster in the latter case set.

It is also important to choose appropriate bounds on the critical parameters mentioned above to generate these test cases. The bounds chosen for these parameters have been presented in Table 4.1.

Table 4.1: Critical Parameters Bounds

Critical Parameter	Lower Bound	Upper Bound
β (point of fault initiation)	0 (voltage zero crossing)	0.00416 (Quarter cycle representing the voltage peak)
α_1 (duration of sub-transmission faults)	4 cycles	6 cycles
α_2 (duration of transmission faults)	2.5 cycles	5 cycles
R1 (fault resistance for sub-transmission faults)	0	0.7
R2 (fault resistance for transmission faults)	0	0.4

From Table 4.1, it should be noted that the bounds considered for the parameter β is appropriate because the sine wave is symmetric. Additionally, the reasoning behind choosing these bounds for the fault resistance for the two case sets has been presented below:

- R1 (fault resistance for sub-transmission faults)
 - Lower Bound (0 ohm) - At 4 cycle fault duration, the fault resistance is manually decreased until all three segment SPIMs are stalling.
 - Upper Bound (0.7 ohm) - At 6 cycle fault duration, the fault resistance is manually increased until all no segments of SPIMs are stalling.
- R2 (fault resistance for transmission faults)
 - Lower Bound (0 ohm) - At 2.5 cycle fault duration, the fault resistance is manually decreased until all three segment SPIMs are stalling.
 - Upper Bound (0.4 ohm) - At 5 cycle fault duration, the fault resistance is manually increased until all no segments of SPIMs are stalling.

4.3.2 Step 2: Data extraction from PSCAD

The following information has been extracted in this step:

- The three-phase voltages observed at the head of the feeder.

- Parameter ‘Y’ for each test case. Where $Y = 0$ (if none of the SPIMs are stalling), $Y = 1$ (if SPIMs on first segment are stalling), $Y = 2$ (if SPIMs on first two segments are stalling) and $Y = 3$ (if SPIMs on all three segments are stalling).
- Fault duration (α) in each test case.

4.3.3 Step 3: Positive sequence voltage generation in ‘Matlab’

The three-phase voltages obtained from Step 2 are transformed into their respective positive sequence voltages by calculating the d-q voltage components in ‘Matlab’. As mentioned earlier in this Chapter, a first order low pass filter has been used to remove the 120 Hz component in the final obtained positive sequence voltage outputs.

4.3.4 Step 4: Data Generation in PSLF

The final obtained positive sequence voltages are played-in to the aggregated feeder and load model, in PSLF, comprising of ‘Motorc’, ‘Motor1’ and ‘Blwsc’ models to represent the SPIMs, three-phase motor load and the resistive load respectively. The composition of this feeder model is shown below (to represent a residential feeder similar to the feeder and load model used in PSCAD to generate the test cases):

- ‘Motorc’ (72%)
- ‘Motor1’ (18%)
- ‘Blwsc’ (10%)

The circuit schematic used in PSLF is shown below in Fig. 4.12.

As expected for all the 240 cases (two case sets), the SPIMs in the feeder and load model in PSLF did not stall. Therefore, after playing-in all the test cases into this feeder model, the following information is extracted:

1. The nadir value of the played-in positive seq voltage per nominal voltage (λ) for each case.
2. The nadir value ($Sp1$) of the SPIM speed (the first segment).
3. The steady-state voltage of the played-in positive seq voltage per nominal voltage (ρ) for each case.

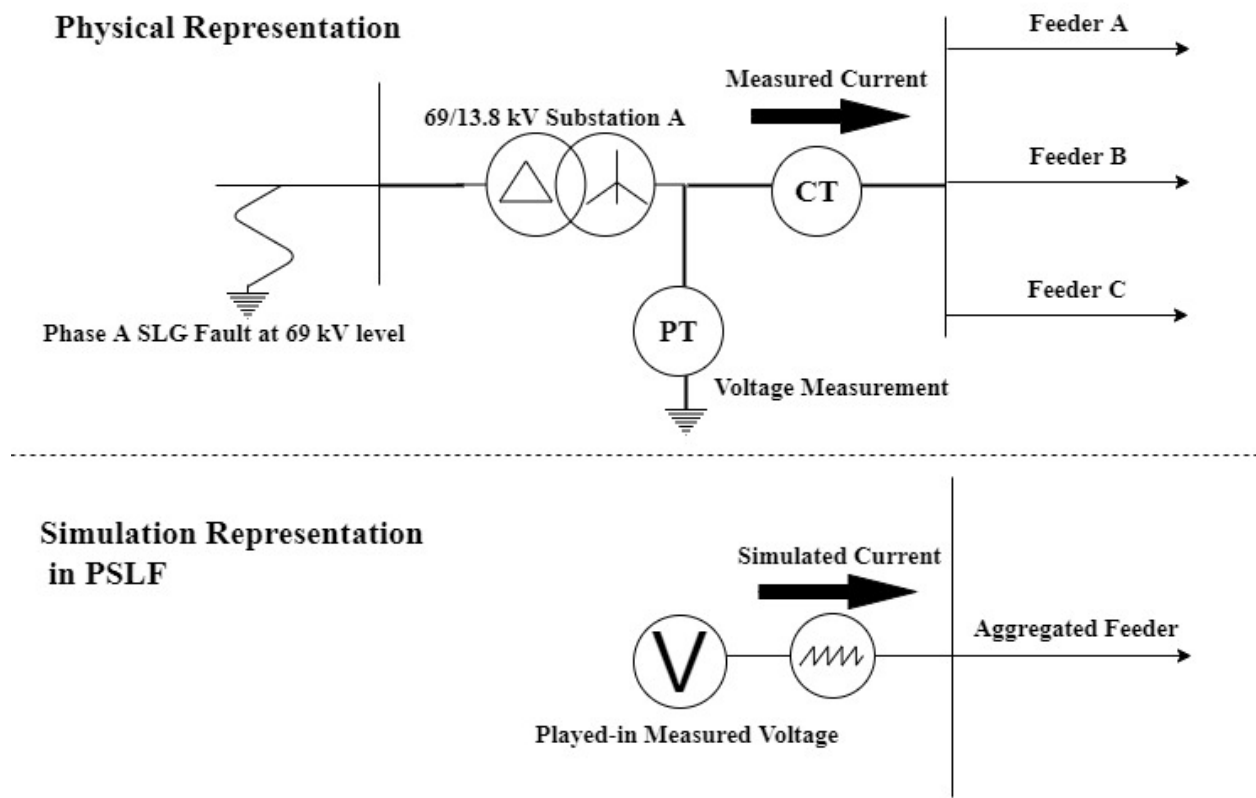


Figure 4.12: Circuit Schematic in PSLF

4.3.5 Step 5: Training the Regression Model

The first 60 test cases (in each case set) has been used to train the two regression models for sub-transmission fault cases and transmission fault cases respectively. The multi-variable linear regression model generated for each case is presented below (4.1):

$$Y = b_0 + b_1X_1 + b_2X_2 + b_3X_3 + b_4X_4 \quad (4.1)$$

Where,

- b_0, b_1, b_2, b_3 and b_4 are the coefficient estimates of the model.
- Y - represents number of SPIM segments in which SPIMs are stalling in PSCAD
- X_1 - represents α (fault duration)
- X_2 - represents λ (Played-in Pos Seq Voltage Nadir per nominal voltage)
- X_3 - represents ρ (post-fault steady-state voltage per nominal voltage obtained from PSLF)
- X_4 - represents Sp1 (Speed nadir of 'Motorc' model in PSLF per nominal speed in Segment1)

4.3.6 Step 6: Regression Model Output Interpretation

- It should be noted that the output obtained from the testing of the regression model will not be a perfect integer indicating the number of stalled SPIM segments. Therefore, the following bounds are used to define the regions in which different number of SPIM segments stall:
 - If $-0.5 < Y_{\text{estimated}} < 0.5$ (no SPIMs are stalled)
 - If $0.5 < Y_{\text{estimated}} < 1.5$ (one segment of SPIMs stalled)
 - If $1.5 < Y_{\text{estimated}} < 2.5$ (two segments of SPIMs stalled)
 - If $2.5 < Y_{\text{estimated}} < 3.5$ (all three segments of SPIMs stalled)

4.3.7 Step 7: Testing results of the regression model

As mentioned in Step 5, the first 60 test cases from both the case sets are used to train the two regression models. Therefore, the next 60 test cases from both the case sets are used to test the two regression models respectively.

The final coefficients obtained from the two regression models are provided in Table 4.2.

The accuracy of the regression models obtained from the testing results are presented below in Table 4.3.

Table 4.2: Final Coefficients obtained for the Regression Models

Coefficient	Obtained Value (Case Set 1)	Obtained Value (Case Set 2)
b₀	0.051	0.056
b₁	0.004	0.004
b₂	-0.018	-0.035
b₃	-0.041	-0.027
b₄	-0.044	-0.056

Table 4.3: Effectiveness of the Regression Models in the Testing

	Number of Test Cases	Accuracy	R² Fit (statistically goodness fit)
Case Set1 (Sub-transmission Faults)	60	93%	87%
Case Set2 (Transmission Faults)	60	97%	91%

From Table 4.3, it can be clearly seen that the obtained regression models are able to predict accurately the SPIM stalling in PSLF ‘Motorc’ model by more than 93% accuracy in both the case sets. Additionally, the R² value, which measures the goodness of the fit [14] of the linear regression model to the data statistically, is almost 90% which indicates the linear regression model used in this work is sufficient to fit the data accurately.

5. Conclusions and future work

5.1 Conclusions

Two approaches have been successfully implemented to obtain reasonably accurate feeder and load models in this work using PSCAD software. The load compositions and the load parameters for these models are modeled for two types of areas (residential and industrial/commercial) and in different conditions (summer and winter). This set of parameters and load compositions were modeled by studying the effects of events such as FIDVR and feeder pickup events. Finally, a multi-variable regression model has been developed to predict the motor stalling phenomenon accurately in PSLF.

The following conclusions can be made from the work presented in Chapter 2, Chapter 3, Chapter 4:

Conclusion1: Using a simple manual tuning approach, two standard feeder and load models (for a residential area – at substation A and for an industrial/commercial area - at substation B) comprising of single-phase motor load, three-phase motor load, impedance load is able to capture a good approximation of the measured current transient characteristics. This is validated by playing-in three-phase measured voltages (representing a fault at 69 kV level and a feeder pick-up event) into the models respectively. It is also observed that these feeder and load models gives good approximate current responses for both summer and winter conditions (for residential feeder and load model). This model represents a load composition of single-phase motor load (72%), three-phase motor load (18%), impedance load (10%) at residential loading conditions. Whereas, the model obtained for industrial/commercial areas represents a load composition of single-phase motor load (25%), three-phase motor load (65%) and impedance load (10%). It was also observed that the parameters of the motors has been obtained using the fault type event measurements whereas the parameters of the distribution transformers in the feeder and load model are obtained using a feeder pick-up event. This phenomenon is observed due to the transformer saturation that occurs during the feeder pick-up in which the load characteristics does not play a major role in the current transient seen at the head of the feeder. However, for a fault type event, the distribution transformers are already magnetized and hence the load characteristics (both composition and parameters) play a significant role in determining the transient response of the feeder and load model.

Conclusion2: The standard feeder and load models obtained using the manual tuning approach has served as a good starting point to implement the analytical approach (non-linear least squares Gauss-Newton optimization procedure) to estimate their motor load parameters and the load composition more accurately. This approach is applied for three cases – Case 1, Case2 (residential feeder and load model) and Case 4 (industrial feeder and load model). It was observed that this approach seems to have the most impact on the Case 4 feeder and load model (this was demonstrated both quantitatively and qualitatively). This is to be expected as the residential feeder and load model has already undergone through manual tuning and hence the improvement gained from using a new analytical approach was significantly smaller

a new analytical approach was significantly smaller (especially in the non-faulted phases). It is also observed that this approach seems to work well for cases in both types of loading conditions (Summer and Winter).

Conclusion3: Both ‘Motor1’ and ‘Motorc’ models seem to give a good match with the simulated P (active power) and Q (reactive power) responses with their corresponding measured responses at the head of the feeder for Case 1 and Case 2. However, it was also observed that, in Case 1 analysis, the post-fault simulation P, Q values do not match well with their corresponding measured values. This was because the motor stalling phenomenon is not captured accurately in PSLF as it doesn’t deal with the POW phenomenon during the transient. Two multi-variable linear regression models (based on the type of SLG faults – Sub-transmission faults and transmission faults) have been developed to overcome this issue. It was observed that these regression models predict the motor stalling in PSLF with more than 93% accuracy for 120 tested cases.

5.2 Future Work

The three-phase feeder and load models developed in this work do not deal with motor protection which plays a crucial role in determining the system response in a FIDVR type event. Therefore, it is important to develop a realistic contactor model [15] in EMTP environment such as PSCAD to study its impact on the feeder and load model response using the test cases utilized in this work.

The regression model obtained to predict motor stalling in PSLF is only useful if the voltage measurements are available from which the voltage nadir and the post-fault steady state voltage are known. Therefore, this type of regression model is useful to study (predict/estimate) the motor stalling phenomenon in the grid when the event has already occurred. However, this is not as much useful for planning studies where the measured voltages from an event are not available yet. Therefore, a more robust regression model needs to be developed to predict motor stalling in PSLF without the need for utilizing the information such as post-fault steady state voltage (whose information is available only if an event has already occurred).

References

- [1] M. Holt and N. Consultant, “Don’t Let Voltage Drop Get Your System Down,” *Electrical Construction & Maintenance*, vol. 1, 2004.
- [2] J. M. Undrill and R. E. Clayton, “Distribution line performance with imperfect grounding,” *IEEE transactions on industry applications*, vol. 24, no. 5, pp. 805–811, 1988, publisher: IEEE.
- [3] Manitoba HVDC, “PSCAD/EMTDC user manual,” Tech. Rep., 2016.
- [4] Y. Liu, V. Vittal, J. Undrill, and J. H. Eto, “Transient model of air-conditioner compressor single phase induction motor,” *IEEE Transactions on Power Systems*, vol. 28, no. 4, pp. 4528–4536, 2013, publisher: IEEE.
- [5] S. Nekkhalpu, “Standard Feeder and Load Model Synthesis Using Voltage and Current Measurements,” PhD Thesis, Arizona State University, 2018.
- [6] C. Carrander, “Magnetizing currents in power transformers: Measurements, simulations, and diagnostic methods,” PhD Thesis, KTH Royal Institute of Technology, 2017.
- [7] P. Mitra and V. Vittal, “Role of sensitivity analysis in load model parameter estimation,” in *2017 IEEE Power & Energy Society General Meeting*. IEEE, 2017, pp. 1–5.
- [8] Y. Enesi, T. Omokhafa, E. Agbachi, and A. James, “Advantage of double cage rotor over single cage rotor induction motor,” *Innovative Systems Design and Engineering*, vol. 6, no. 12, pp. 1–4, 2015.
- [9] J. Susanto and S. Islam, “Improved Parameter Estimation Techniques for Induction Motors using Hybrid Algorithms,” *arXiv preprint arXiv:1704.02424*, 2017.
- [10] L. Wang, J. Jatskevich, C. Wang, and P. Li, “A voltage-behind-reactance induction machine model for the EMTP-type solution,” *IEEE Transactions on Power Systems*, vol. 23, no. 3, pp. 1226–1238, 2008, publisher: IEEE.
- [11] X. Xu, M. F. Kandlawala, and M. Wu, “NERC TPL-001-4 transient voltage performance compliance study-criteria development, study methodology and case studies,” in *2016 IEEE Power and Energy Society General Meeting (PESGM)*. IEEE, 2016, pp. 1–5.
- [12] General Electric, “PSLF User’s Manual,” Tech. Rep., 2019.
- [13] PTI, “PSS®E 34.2 Program Operation Manual,” Tech. Rep., 2017.
- [14] J. Nazarko and W. Zalewski, “The fuzzy regression approach to peak load estimation in power distribution systems,” *IEEE Transactions on Power Systems*, vol. 14, no. 3, pp. 809–814, 1999, publisher: IEEE.
- [15] J.-R. R. Ruiz, A. G. Espinosa, and L. Romeral, “A computer model for teaching the dynamic behavior of AC contactors,” *IEEE Transactions on Education*, vol. 53, no. 2, pp. 248–256, 2009, publisher: IEEE.

Part II

Enhanced Transmission and Distribution System Operation and Planning with Improved Dynamic Load Modeling

Le Xie

Xinbo Geng, Graduate Student

Athindra Venkatraman, Graduate Student

Texas A&M University

For information about this project, contact

Le Xie
Texas A&M University
3128 TAMU
College, TX 77843
Phone: 979-845-7563
Email: le.xie@tamu.edu

Power Systems Engineering Research Center

The Power Systems Engineering Research Center (PSERC) is a multi-university Center conducting research on challenges facing the electric power industry and educating the next generation of power engineers. More information about PSERC can be found at the Center's website: <http://www.pserc.org>.

For additional information, contact:

Power Systems Engineering Research Center
Arizona State University
527 Engineering Research Center
Tempe, Arizona 85287-5706
Phone: 480-965-1643
Fax: 480-727-2052

Notice Concerning Copyright Material

PSERC members are given permission to copy without fee all or part of this publication for internal use if appropriate attribution is given to this document as the source material. This report is available for downloading from the PSERC website.

© 2021 Texas A&M University. All rights reserved.

Table of Contents

1. Robust Look-Ahead Phase Balancing	1
1.1 Introduction.....	1
1.2 Robust Optimization: Preliminaries.....	2
1.3 Formulations of Phase Balancing Problems	3
1.3.1 Nomenclature	3
1.3.2 Deterministic Phase Balancing	4
1.3.3 Robust Phase Balancing.....	5
1.3.4 Robust Look-ahead Phase Balancing.....	6
1.4 Case Study	9
1.4.1 Load Data.....	9
1.4.2 Construct Unvertainty Set.....	9
1.4.3 Simulation Results	10
1.5 Discussions	15
1.5.1 Uncertainty Sets	15
1.5.2 Approximation Algorithms.....	15
1.5.3 Multi-phase Loads	16
1.6 Concluding Remarks.....	16
1.7 Appendix: Equivalent Formulation of Robust Look-ahead Phase Balancing	16
2. Optimal Reactive Power Dispatch	18
2.1 Introduction.....	18
2.1.1 Background.....	18
2.1.2 Chance Constrained Programming	19
2.1.3 Chance-constrained Programs in Power Systems.....	19
2.2 Impacts of Win Uncertainties on Voltage Security	20
2.2.1 Wind Farm Modeling.....	20
2.2.2 A Linear Approximation.....	20
2.3 Big-M Approach to Solve CCPs.....	21
2.4 Chance-constrained Optimal Reactive Power Dispatch	21
2.4.1 Deterministic Optimal Reactive Power Dispatch	21
2.4.2 Chance-constrained Optimal Reactive Power Dispatch	23
2.4.3 Linearize cc-ORPD.....	25

2.5	Case Study	25
2.5.1	Settings.....	25
2.5.2	Simulation Results	26
2.6	Concluding Remarks.....	27
3.	Electricity as a Service.....	29
3.1	Introduction.....	29
3.2	Methodology and Data.....	31
3.2.1	Proposed Utility Business Model.....	31
3.2.2	Metrics causing Distribution Grid Investments	33
3.2.3	Peak Deman Indicator Function.....	33
3.2.4	Calculating the Grid Impact Factors W and V	34
3.2.5	Calculating the Final Bills	35
3.2.6	Data and Case Study System Description.....	36
3.3	Results and Discussion	37
3.3.1	Comparing the Performance of Two Homes in the Proposed Mechanism.....	37
3.3.2	Comparing the Current and Proposed Billing Mechanisms	31
3.3.3	The Effect of DER Penetration on TDU Charges Calculated under the Proposed Mechanism	38
3.3.4	Effect of Battery Storage on TDU Charges calculated under the Proposed Mechanism	39
3.3.5	Effect of Customer Aggregation on TDU Charges calculated under the Proposed Mechanism	40
3.3.6	Pros and Cons of the Proposed Mechanism.....	41
3.3.7	Policy Implications	44
4.	Concluding Remarks.....	46
	References.....	48

List of Figures

Figure 1.1 Illustration of the Look-ahead Operation Framework (every block represents the phase assignment of a load at each snapshot)	7
Figure 1.2 Modified Load Dataset "R1-1247-4"	11
Figure 1.3 Sorted between-phase kW differences	12
Figure 1.4 Display of Optimal Solutions (ABC phases are color-coded, red:phase A, blue:phase B, green:phase C).....	14
Figure 1.5 Phase Swapping Actions of Each Load (results of r-LAPB (s = 2) running for 150 days)	15
Figure 2.1 Impacts of Wind Uncertainties on Voltage Magnitudes	20
Figure 2.2 Voltage Magnitudes in the Normal Operating Condition	26
Figure 2.3 Violation Probabilities.....	27
Figure 3.1 Current vs. Proposed TDU Charges: Consumer Cost Curve	32
Figure 3.2 Peak Demand Indicator Function μ	34
Figure 3.3 System Demand Curve and Comparison of Demand between two homes over 1 week during Peak Time Slots	37
Figure 3.4 Comparison of Proposed and Existing Billing Mechanism for Homes	38
Figure 3.5 % Change in TDU Charges before and after 25% DER Penetration (Calculated under the Proposed Mechanism).....	39
Figure 3.6 % Change in TDU Charges (New Mechanism) after introducing Battery Storage in 25 PV Homes	40
Figure 3.7 Case Study: Aggregating a low- V_i EV customer and high- V_i PV customer	41

List of Tables

Table 1.1 Parameters.....	13
Table 1.2 Comparison of Solutions	13
Table 2.1 det-ORPD vs cc-ORPD	27
Table 3.1 Case Study: Comparing Impact and Total TDU Charges before and after Aggregation.....	43

1. Robust Look-ahead Three-phase Balancing of Uncertain Distribution Loads

Increasing penetration of highly variable components such as solar generation and electric vehicle charging loads pose significant challenges to keeping three-phase loads balanced in modern distribution systems. Failure to maintain balance across three phases would lead to asset deterioration and increasing delivery losses. Motivated by the real-world needs to automate and optimize the three-phase balancing decision making, this paper introduces a robust look-ahead optimization framework that pursues balanced phases in the presence of demand-side uncertainties. We show that look-ahead moving window optimization can reduce imbalances among phases at the cost of a limited number of phase swapping operations. Case studies quantify the improvements of the proposed methods compared with conventional deterministic phase balancing. Discussions on possible benefits of the proposed methods and extensions are presented.

1.1 Introduction

Increasing levels of distributed energy resources, together with more active participation of demand side programs, have introduced higher levels of uncertainties to distribution grid operations. One fundamental task for distribution system operators (DSOs) is to keep three phases as balanced as possible over a long period of time. However, the increasing variability coming from end users requires DSOs to revisit this old problem with modern techniques. Imbalanced three phases could lead to higher risks of equipment failures [1], increased delivery losses [2], potential relay malfunctioning [3], additional asset reinforcement costs [4], and issues related with voltage imbalances [5–8]. In particular, there is increasing need to develop solutions that can keep three phases balanced in the presence of high uncertainties from end users over a period of time (e.g. over the course of a day). In this paper, we provide a novel and scalable solution for addressing this problem.

From a DSO’s perspective, there are three levels of decisions that can be made to ensure reliable and efficient delivery of electricity to end-users during normal conditions. At the highest level, it can engage with transmission-level voltage/reactive power optimization routine to regulate its voltage level at the point of interconnection with the backbone grid [9, 10]. At the medium level, modern distribution operator could control various sectionalizers and tie switches in order to optimize the *topology* of a distribution system [11, 12]. At the lowest level, DSOs need to optimize the assignment of each load (or each cluster of loads) to appropriate phases in order to keep the three phase balanced during a wide range of operating conditions. This paper addresses the issue at the lowest level.

There is a large body of literature that addresses the issue of keeping three phases balanced in distribution systems. The phase balancing problem has been traditionally formulated as a mixed integer linear program (MILP) [1]. Due to the computational intractability of mixed integer programs, many optimization techniques and heuristics have been applied to phase balancing: simulated annealing [13], expert systems [14], particle swarm optimization [15], immune algorithm [3, 16] and dynamic programming [17]. These works [1, 3, 14–17] typically consider either a single

snapshot or use average loads over a long period of time. In [18, 19], the authors demonstrate the benefits of extending the phase balancing problem to multiple snapshots and utilizing daily load patterns. It is worth mentioning that [1, 3, 14–19] solve the deterministic phase balancing problem. *Uncertainties as well as inter-temporal variabilities* have not been taken into account in the problem of phase balancing. This is the key gap we attempt to bridge in this work.

The remainder of this paper is organized as follows: Section 1.2 introduces robust optimization; Section 1.3 first reviews the deterministic phase balancing problem, which is enhanced to a robust optimization problem in Section 1.3.3. The proposed robust look-ahead phase balancing problem is in Section 1.3.4. Case studies and discussions are presented in Section 1.4 and 1.5. Conclusions and future works are in Section 1.6.

1.2 Robust Optimization: Preliminaries

Broadly speaking, there are two approaches for decision making in uncertain environments: *stochastic* optimization (SO) and *robust* optimization (RO). SO relies on probabilistic models to explain the uncertainties in data and often results in solutions that are sensitive to these assumptions¹. On the other hand, RO incorporates a set-based deterministic model of the uncertainty such that the optimal solution protects against all realizations in the uncertainty set. Compared with SO, one significant advantage of RO is the computational tractability, which is important for the phase balancing problem to be applicable in real-world scenarios. Moreover, it has been observed that robust solutions are competitive with the deterministic solutions in terms of cost, while being more robust to unplanned uncertainties in the data. Robust optimization also does not need to assume any probabilistic information about the uncertain quantities [21].

We consider the following row-uncertain robust linear optimization problem, where the row vectors α_i are uncertain in each constraint:

$$\underset{x}{\text{minimize}} \quad \gamma^\top x \tag{1.1a}$$

$$\begin{aligned} \text{subject to} \quad & \alpha_i^\top x \leq \beta_i, \forall \alpha_i \in \mathcal{U}_i, \\ & i = 1, 2, \dots, m. \end{aligned} \tag{1.1b}$$

Formulation (1.1) seeks an optimal solution $x \in \mathbb{R}^n$ that is feasible to m linear uncertain constraints $\alpha_i^\top x \leq \beta_i$, in which the uncertain vector of parameters α_i can take any values from the uncertainty set \mathcal{U}_i . A common choice is the polyhedral uncertainty set defined as

$$\mathcal{U}_i := \{\alpha_i : H_i \alpha_i \leq h_i\}, i = 1, 2, \dots, m, \tag{1.2}$$

where $H_i \in \mathbb{R}^{k \times n}$ and $h_i \in \mathbb{R}^k$ depict k inequalities that define a polyhedron. Such uncertainty sets have been successful in capturing insights from probability theory to obtain more realistic models. For instance, if the data is generated independently from a probability distribution then the well-known central limit theorem states that the appropriately normalized average of variables tends to a normal distribution. The central limit theorem can be written as a polyhedral uncertainty

¹We refer an interested reader to [20] for a survey on stochastic modeling and techniques.

set that protects against all realizations of data that satisfy the central limit theorem [22]. Its parameters can be set such that if the data was generated via a given probability distribution, then the uncertainty set captures provably 95% – 99% of possible scenarios. This provides a clean way to incorporate probabilistic information. We refer the reader to [23] for a more detailed survey on robust optimization techniques.

In the definition of a polyhedral uncertainty set $\mathcal{U} = \{\alpha \in \mathbb{R}^n \mid H\alpha \leq h\}$ where $H \in \mathbb{R}^{k \times n}$, the constraint $\alpha^\top x \leq \beta \forall \alpha \in \mathcal{U}$ is equivalent to

$$b \geq \underset{\alpha}{\text{maximize}} \quad x^\top \alpha \quad (1.3a)$$

$$\text{subject to } H\alpha \leq h. \quad (1.3b)$$

Let $p \in \mathbb{R}_+^k$ be the dual variable for (1.3b). Then the dual linear program of (1.3) is:

$$\underset{p}{\text{minimize}} \quad h^\top p \quad (1.4a)$$

$$\text{subject to } H^\top p = x, \quad (1.4b)$$

$$p \geq 0. \quad (1.4c)$$

By weak duality, any feasible solution p of (1.4) for a given x provides a lower bound to (1.3), i.e. $h^\top p \leq^{(*)} \max_{\alpha \in \mathcal{U}} \alpha^\top x \leq b$, and the inequality (*) is tight for the optimal solution of the dual formulation in (1.4), by strong duality.

Therefore the uncertain constraints $\alpha_i^\top x \leq \beta_i \forall \alpha_i \in \mathcal{U}_i$ are equivalent to the following deterministic constraints:

$$h_i^\top p_i \leq \beta_i, \quad H_i^\top p_i = x, \quad p_i \geq 0,$$

where each $p_i \in \mathbb{R}_+^k$ is a vector of auxiliary variables corresponding to the i th constraint in (1.1). The robust formulation (1.1) with polyhedral uncertainty sets \mathcal{U}_i is then equivalent to the following linear program [24]:

$$\underset{x}{\text{minimize}} \quad \gamma^\top x \quad (1.5a)$$

$$\text{subject to } h_i^\top p_i \leq \beta_i, \quad (1.5b)$$

$$H_i^\top p_i = x, \quad (1.5c)$$

$$p_i \in \mathbb{R}_+^k, i = 1, 2, \dots, m. \quad (1.5d)$$

One major advantage of using a polyhedral uncertainty set is its computational tractability. The reformulation of the robust linear program (1.1) as the deterministic linear program (1.5) involves a few more variables and this does not increase the overall computational complexity [24].

1.3 Formulations of Phase Balancing Problems

1.3.1 Nomenclature

Time dependent variables are represented with $\cdot[t]$, e.g. $d[t]$ is the demand at time t . Matrices are represented using capital letters and uncertainty sets are in calligraphic font. $|\cdot|$ is the

absolute value function and \top denotes transpose of matrices or vectors. By $\mathbf{1}$, we mean the vector of all ones in the appropriate dimension (typically n in this paper, e.g. in (1.6b) $\mathbf{1} \in \mathbb{R}^n$).

1.3.2 Deterministic Phase Balancing

We briefly review the conventional formulation of phase balancing in this subsection. Formulation (1.6) presented below is a slight variation of the original one in [1].

$$\underset{a,b,c,u_a,u_b,u_c}{\text{minimize}} \quad \max\{u_a, u_b, u_c\} \quad (1.6a)$$

$$\text{subject to} \quad u_a = |d^\top(a - \frac{\mathbf{1}}{3})|, \quad (1.6b)$$

$$u_b = |d^\top(b - \frac{\mathbf{1}}{3})|, \quad (1.6c)$$

$$u_c = |d^\top(c - \frac{\mathbf{1}}{3})|, \quad (1.6d)$$

$$a + b + c = \mathbf{1}, \quad (1.6e)$$

$$a, b, c \in \{0, 1\}^n, \quad (1.6f)$$

$$u_a, u_b, u_c \in \mathbb{R}_+. \quad (1.6g)$$

Phase balancing aims at finding the most balanced assignment of n loads $d \in \mathbb{R}^n$ to three phases (A,B,C). Phase balancing commonly relies on phase swapping (or re-phasing) actions to reduce imbalances. Phase swapping typically happens at the feeder level, during maintenance or restoration periods [1]. Phase swapping actions are depicted by decision variables a , b and c , all of which are binary vectors with dimension equal to the number of loads, where $a_i = 1$ (similarly, $b_i, c_i = 1$) denotes load d_i is assigned to phase A (similarly, to phase B, C), and 0 indicates d_i is not assigned to that phase. Constraint (1.6e) ensures that each load must be assigned to exactly one phase². Variables u_a , u_b , u_c represent single-phase imbalances, namely the difference of load on phase A (B,C) from the uniformly balanced case $d^\top \mathbf{1}/3$. The objective (1.6a) is to minimize the largest imbalance amongst the three phases. The original formulation in [1] minimizes the largest differences between any two phases, i.e.

$$\underset{a,b,c \in \{0,1\}^n}{\text{minimize}} \quad \max\{|d^\top(b - a)|, |d^\top(b - c)|, |d^\top(a - c)|\}. \quad (1.7)$$

These two formulations are closely related in the following sense. Let the total loads assigned to phases A, B and C be x , y and z respectively, and let the total overall load be $x + y + z = d^\top \mathbf{1}$. Without loss of generality, let $x \leq y \leq z$ which implies $x \leq d^\top \mathbf{1}/3 \leq z$. So, the objective value of (1.7) will be $z - x$ whereas the objective value of (1.6) for such an assignment will be $\max\{d^\top \mathbf{1}/3 - x, z - d^\top \mathbf{1}/3\}$, but note that $z - x \leq 2 \max\{d^\top \mathbf{1}/3 - x, z - d^\top \mathbf{1}/3\}$. Therefore, the optimal solution of (1.7) will be at most twice the optimal solution of (1.6) (and similarly, optimal solution of (1.7) is at least the optimal solution of (1.6)). Further, we believe that our formulation in (1.6) meets the intuitive notion of phase balancing better than (1.7). To see this, consider a total given demand of 21 kW. Formulation (1.7) does not differentiate between the assignments 2,9,10

²For simplicity, we only consider single-phase loads in this paper. Extensions to multi-phase loads are in Section 1.5.3.

kW and 3,7,11 kW on each phase. For either assignment, the maximum difference between the assigned loads is 8 kW. However, our formulation (1.6) would prefer 3,7,11 as a solution since it minimizes the maximum deviation from the average. The absolute value constraints (1.6b), (1.6c) and (1.6d) can be reformulated to obtain an equivalent mixed integer linear program [25]:

$$\underset{a,b,c,u}{\text{minimize}} \quad u \quad (1.8a)$$

$$\text{subject to} \quad -u \leq d^\top \left(a - \frac{\mathbf{1}}{3} \right) \leq u, \quad (1.8b)$$

$$-u \leq d^\top \left(b - \frac{\mathbf{1}}{3} \right) \leq u, \quad (1.8c)$$

$$-u \leq d^\top \left(c - \frac{\mathbf{1}}{3} \right) \leq u, \quad (1.8d)$$

$$a + b + c = \mathbf{1}, \quad (1.8e)$$

$$a, b, c \in \{0, 1\}^n, u \in \mathbb{R}_+. \quad (1.8f)$$

1.3.3 Robust Phase Balancing

In deterministic phase balancing problem (1.6), load vector d represents the average load level during a long period, without any uncertainties. Motivated by the rapid growth of highly variable resources in distribution systems, we connect conventional phase balancing with robust optimization and formulate the following robust phase balancing problem:

$$\underset{u,a,b,c}{\text{minimize}} \quad u \quad (1.9a)$$

$$\text{subject to} \quad -u \leq d^\top \left(a - \frac{\mathbf{1}}{3} \right) \leq u, \forall d \in \mathcal{D}, \quad (1.9b)$$

$$-u \leq d^\top \left(b - \frac{\mathbf{1}}{3} \right) \leq u, \forall d \in \mathcal{D}, \quad (1.9c)$$

$$-u \leq d^\top \left(c - \frac{\mathbf{1}}{3} \right) \leq u, \forall d \in \mathcal{D}, \quad (1.9d)$$

$$a + b + c = \mathbf{1}, \quad (1.9e)$$

$$a, b, c \in \{0, 1\}^n, u \in \mathbb{R}_+. \quad (1.9f)$$

The major difference between robust phase balancing (1.9) and the deterministic version (1.8) is that: instead of seeking solutions (a, b, c) that are feasible for the average or expected load vector d , (1.9) seeks solutions robust to all realizations of d in an uncertainty set \mathcal{D} . The uncertainty set \mathcal{D} can be constructed using historical data or approximated with prior knowledge.

Similar to Section 1.2, formulation (1.9) with polyhedral uncertainty set $\mathcal{D} = \{d : Hd \leq h\}$ can

be rewritten as an MILP (1.10).

$$\begin{array}{ll} \text{minimize} & u \\ & p, q, a, b, c, u \end{array} \quad (1.10a)$$

$$\text{subject to} \quad h^\top p_a \leq u, \quad H^\top p_a = a - \frac{\mathbf{1}}{3}, \quad (1.10b)$$

$$h^\top q_a \leq u, \quad H^\top q_a = \frac{\mathbf{1}}{3} - a, \quad (1.10c)$$

$$h^\top p_b \leq u, \quad H^\top p_b = b - \frac{\mathbf{1}}{3}, \quad (1.10d)$$

$$h^\top q_b \leq u, \quad H^\top q_b = \frac{\mathbf{1}}{3} - b, \quad (1.10e)$$

$$h^\top p_c \leq u, \quad H^\top p_c = c - \frac{\mathbf{1}}{3}, \quad (1.10f)$$

$$h^\top q_c \leq u, \quad H^\top q_c = \frac{\mathbf{1}}{3} - c, \quad (1.10g)$$

$$a + b + c = \mathbf{1}, \quad (1.10h)$$

$$a, b, c \in \{0, 1\}^n, u \in \mathbb{R}_+, \quad (1.10i)$$

$$p_a, p_b, p_c, q_a, q_b, q_c \in \mathbb{R}_+^k \quad (1.10j)$$

where p_a, p_b, p_c and q_a, q_b, q_c are auxiliary variables.

1.3.4 Robust Look-ahead Phase Balancing

The problem formulated in Section 1.3.3 considers only a single snapshot (e.g. one hour) decision making for robust phase balancing. However, one key component of costs comes from frequent phase swapping actions of loads. Therefore, it is important to consider the phase balancing problem in a multi-time-horizon setting. We formulate it as a robust look-ahead phase balancing problem, much like the usual practices in [26, 27].

In the following formulation (1.11), we consider a two-period moving horizon phase balancing decision making. For example, each snapshot (i.e., t) could signify two hours in the day, a period $1, \dots, T_1$ (i.e. a day) consists of 12 snapshots, and the moving horizon might consist of two days. The objective function (i.e., phase imbalances) is defined over the two periods combined. However, *the decisions are only implemented for the first period*. The reason for doing so is justified by the engineering insight that information gets more accurate as we get closer to real-time operations. Therefore, the decision made for period two is only advisory but not implemented.

An illustrative example with 4 loads over 10 intervals is provided in Figure 1.1. A robust look-ahead phase balancing problem is solved for intervals 1 to 10 given initial load assignments at interval 0. Two phase swaps are implemented in the illustrated solution (top of Figure 1.1: load 2 is swapped to phase B at the beginning of interval 2, load 3 is swapped to phase C at the beginning of interval 4. At the end of interval 5, uncertainty sets for interval 6 to 15 are constructed using updated load forecast and another robust look-ahead phase balancing problem is solved for intervals 6 to 10. The solution implemented performs three phase swaps in intervals 6 to 10, as shown at the bottom of Figure 1.1.

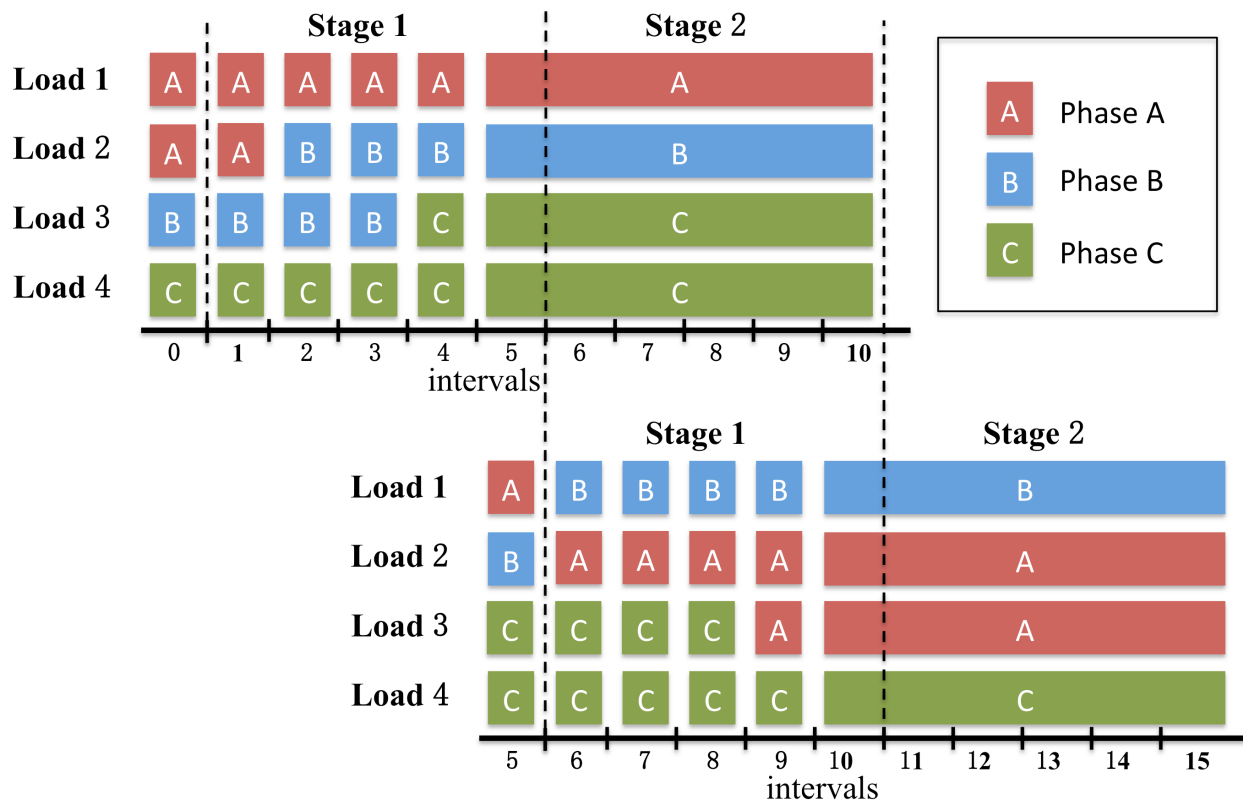


Figure 1.1: Illustration of the Look-ahead Operation Framework (every block represents the phase assignment of a load at each snapshot)

We next provide a mixed integer formulation to solve the two-period moving horizon phase balancing problem.

$$\text{minimize } u + \lambda v \tag{1.11a}$$

$$\text{subject to } -u \leq (d[t])^\top (a[t] - \frac{\mathbf{1}}{3}) \leq u, \forall d[t] \in \mathcal{D}_t, \tag{1.11b}$$

$$-u \leq (d[t])^\top (b[t] - \frac{\mathbf{1}}{3}) \leq u, \forall d[t] \in \mathcal{D}_t, \tag{1.11c}$$

$$-u \leq (d[t])^\top (c[t] - \frac{\mathbf{1}}{3}) \leq u, \forall d[t] \in \mathcal{D}_t, \tag{1.11d}$$

$$t = 1, 2, \dots, T_1$$

$$-v \leq (d[t])^\top (a[T_1] - \frac{\mathbf{1}}{3}) \leq v, \forall d[t] \in \mathcal{D}_t, \tag{1.11e}$$

$$-v \leq (d[t])^\top (b[T_1] - \frac{\mathbf{1}}{3}) \leq v, \forall d[t] \in \mathcal{D}_t, \tag{1.11f}$$

$$-v \leq (d[t])^\top (c[T_1] - \frac{\mathbf{1}}{3}) \leq v, \forall d[t] \in \mathcal{D}_t, \tag{1.11g}$$

$$t = T_1 + 1, T_1 + 2, \dots, T_2$$

$$\sum_{t=1}^{T_1} \left(\mathbf{1}^\top |a[t] - a[t-1]| + \mathbf{1}^\top |b[t] - b[t-1]| + \mathbf{1}^\top |c[t] - c[t-1]| \right) \leq 2s, \tag{1.11h}$$

$$a[t] + b[t] + c[t] = \mathbf{1}, \tag{1.11i}$$

$$a[t], b[t], c[t] \in \{0, 1\}^n, u, v \in \mathbb{R}_+, \tag{1.11j}$$

$$t = 1, 2, \dots, T_1.$$

In the above formulation (1.11), the first period consists of T_1 snapshots ($t = 1, 2, \dots, T_1$). It determines the phase swapping actions to be implemented. Similar to previous formulations, $a_i[t] = 1$ indicates load $d_i[t]$ is assigned to phase A at time t ($t = 1, 2, \dots, T_1$). (1.11b)-(1.11d) are robust constraints for period 1. It is worth noting that each snapshot has its own uncertainty set $d[t] \in \mathcal{D}_t$. This allows (1.11) to take advantage of the temporal patterns of uncertain loads. As illustrated in Figure 1.1, no phase swapping actions are considered for period 2. Formulation (1.11) seeks *fixed* load assignments with small phase imbalances for period 2. The decision variables of the second period are $a[T_1]$, $b[T_1]$ and $c[T_1]$. Constraints (1.11e)-(1.11g) relate to decisions in period 2.

We do not allow phase swapping actions in the second period of (1.11) for two important reasons:(a) uncertainties for the second period could be significantly larger than in the first one, over-optimization with large uncertainties might lead to conservative solutions; (b) the problem size will be twice larger if we consider phase swapping in both periods thus hurting performance. Recall that phase balancing is an MILP, the computational burden could be prohibitive³

³We actually tested the case in which phase swapping is considered in both periods. Gurobi [28] took 12 hours to

Variables u and v denote the largest single-phase imbalance that occurs in the two periods, respectively. Choosing a proper value of parameter $\lambda \in \mathbb{R}_+$ could achieve a balance between the optimality in short term and long term.

Given current industrial practice, swapping loads from one phase to another typically requires manual operations, which incurs extra costs on human resources, maintenance expenses and planned outage duration [1]. Constraint (1.11h) limits the maximum number of phase swapping actions in the first period. Parameter s denotes the budget of swapping actions. Without constraint (1.11h), a large amount of phase swapping actions could be recommended, which is not affordable for utility companies [1].

For each snapshot $t = 1, 2, \dots, T_2$, the polyhedral uncertainty set is defined as

$$\mathcal{D}_t = \{d[t] : H_t d[t] \leq h_t\} \quad (1.12)$$

By introducing auxiliary variables, (1.11) is equivalent to an MILP (1.15).

It is worth mentioning that a recent paper [29] proposes a related but different approach with stochastic optimization. It minimizes the expected loss function over a time horizon with respect to uncertainties from loads and electricity prices. While its decision variables denote the charging and discharging rates of energy storages, load assignments remain unchanged and no phase swapping actions are considered.

1.4 Case Study

1.4.1 Load Data

The load profiles are from dataset “R1-12.47-4” of [30]. It models a heavily populated suburban area composed mainly of single family homes and heavy commercial loads [31]. The dataset “R1-12.47-4” is populated with hourly averaged load data from a utility company in the West Coast of the United States [30]. The original dataset is publicly available on catalog.data.gov. The dataset contains 74 hourly load profiles of 365 days. We use the first 30 days and scale them randomly to avoid identical load profiles.

Figure 1.2 visualizes the modified dataset.

1.4.2 Construct Uncertainty Set

In order to demonstrate the benefits of robustification, we use the following polyhedral uncertainty sets for the robust Phase Balancing (r-PB) and robust Look-ahead Phase Balancing (r-LAPB) problems:

$$\mathcal{D} = \{d \in \mathbb{R}^n : \hat{d} \leq d - \bar{d} \leq \hat{d}\} \quad (1.13)$$

converge and the solution was comparable to the current formulation in (1.11).

$$\mathcal{D}_t = \{d[t] \in \mathbb{R}^n : (1 - \rho_t)\overline{d[t]} \leq d[t] \leq (1 + \rho_t)\overline{d[t]}\} \quad (1.14)$$

where $d \in \mathbb{R}^n$ or $d[t] \in \mathbb{R}^n$ represent the average load or forecast value, and $\hat{d} \in \mathbb{R}^n$ denotes the largest deviation of load d . Problem \mathfrak{r} -PB (1.9) with $\hat{d} = 0$ is equivalent with deterministic Phase Balancing (d-PB) (1.6). Values of d , $d[t]$ and \hat{d} are estimated from the modified ‘‘R1-1247-4’’ dataset. These uncertainty sets can be viewed as simple relaxations of the central limit theorem based sets (which can risk the solution being too conservative), but they already show a significant improvement in our experiments compared to deterministic solutions.

For r-LAPB, the level of robustness ρ_t depends on the forecast accuracy or confidence. Larger ρ_t indicates lower forecast accuracy. Definition of \mathcal{D}_t in (1.13)-(1.14) assumes that the load forecast is unbiased and bounded by ρ_t . For r-LAPB, ρ_t in the first period (i.e. 24 hours) is set to be 10% ($t = 1, 2, \dots, 24$) and $\rho_t = 30\%$ for the second period ($t = 25, 26, \dots, 48$).

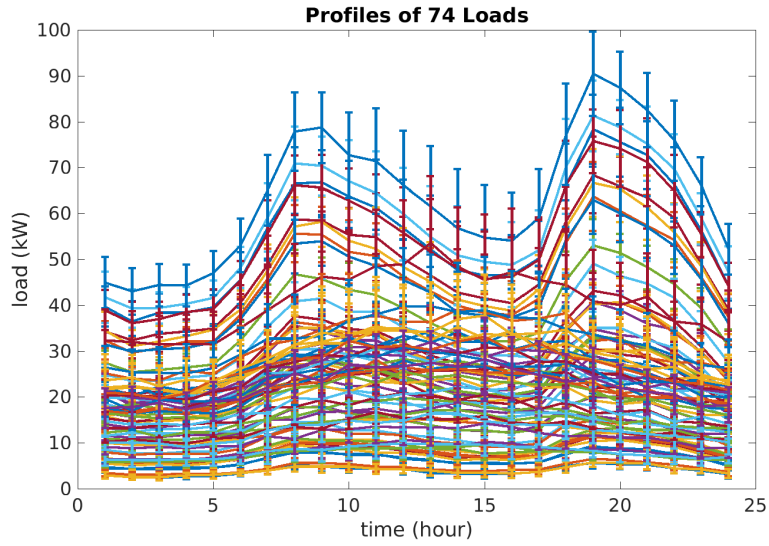
For d-PB (1.6), load vector d is the average hourly load of 30 days. There is no uncertainty associated.

1.4.3 Simulation Results

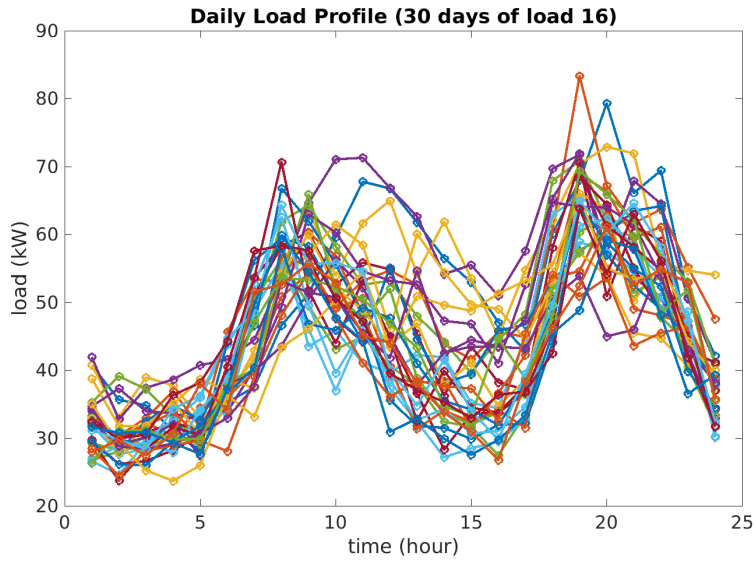
Simulations are performed on a desktop with Intel i7-2600 8-core CPU@3.40GHz and 16GB memory. The phase balancing problems are solved using YALMIP [32, 33] and Gurobi [28]. The optimality gap of every solution is smaller than 0.1%. Key results are presented in Figure 1.3 and Table 1.2.

The performance of three formulations are evaluated using three metrics: between-phase kW difference ω , single-phase kW difference ν and single-phase percentage difference ν , which are defined below:

$$\begin{aligned} \omega &:= \max\{|d^\top(a - b)|, |d^\top(a - c)|, |d^\top(b - c)|\}, \\ \nu &:= \max\{|d^\top(a - \mathbf{1}/3)|, |d^\top(b - \mathbf{1}/3)|, |d^\top(c - \mathbf{1}/3)|\}, \\ \nu &:= \max\{|1 - \frac{3d^\top a}{d^\top \mathbf{1}}|, |1 - \frac{3d^\top b}{d^\top \mathbf{1}}|, |1 - \frac{3d^\top c}{d^\top \mathbf{1}}|\}. \end{aligned}$$



(a) average daily load profiles with standard deviations (each color represents one load)



(b) profiles of load 16 (different colors represent different days)

Figure 1.2: Modified Load Dataset “R1-1247-4”

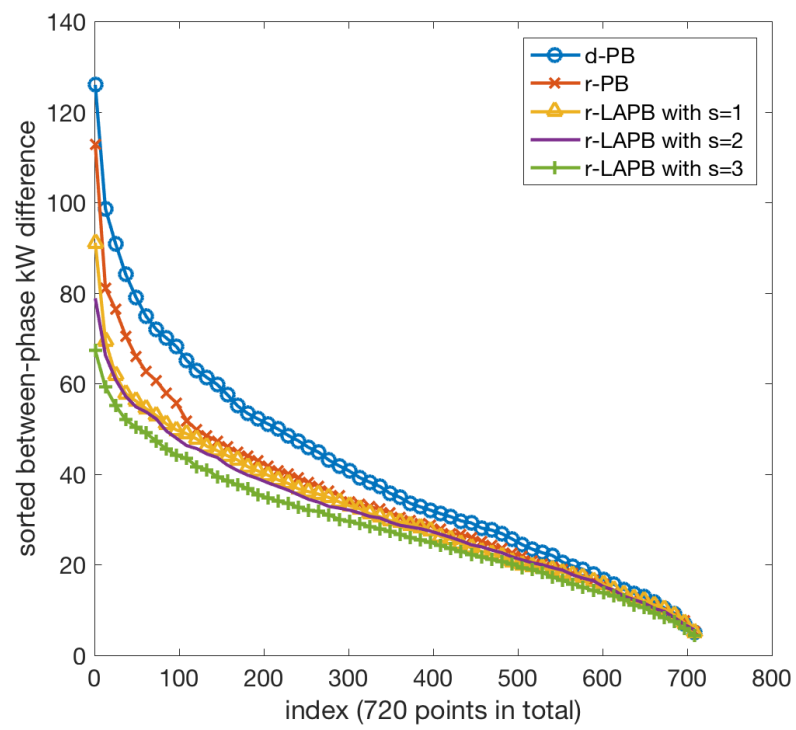


Figure 1.3: Sorted between-phase kW differences

Table 1.1: Parameters

n	T_1	T_2	λ	ρ_t (period1)	ρ_t (period2)
74	24	48	1/3	10%	30%

Table 1.2: Comparison of Solutions

Method	between-phase (kW)			single-phase (kW)			single-phase (%)			runtime (s)		
	max	avg	std	max	avg	std	max	avg	std	max	avg	std
d-PB	125.97	39.71	23.45	71.63	22.91	13.36	10.93	4.03	2.13	-	15.8	-
r-PB	112.79	33.55	18.78	63.66	19.27	10.87	10.56	3.44	1.87	-	1.3	-
r-LAPB _(s=1)	91.09	31.12	15.81	49.19	17.91	9.11	10.62	3.25	1.69	109.0	56.2	18.3
r-LAPB _(s=2)	78.83	30.39	15.02	45.84	17.45	8.60	9.71	3.20	1.69	1317.0	285.2	246.7
r-LAPB _(s=3)	67.28	27.77	13.74	40.69	16.00	7.93	8.59	2.97	1.65	7756.6	2380.5	1321.2

Compared with d-PB, robust phase balancing (r-PB) reduces both between-phase and single-phase imbalances by around 11%, the standard deviations of imbalances are reduced by more than 20%. It is also worth mentioning that the time to solve r-PB is significantly reduced due to more restricted search space since the robust solutions must be feasible for all demand realizations.

Table 1.2 shows that the imbalances could be significantly reduced by incorporating look-ahead operations. For example, r-LAPB with 3 swapping actions per day reduces both between-phase and single-phase kW differences by 30% on average.

Figure 1.3 and Table 1.2 also demonstrate the trade-off between performance and computation complexity. In general, more frequent phase swapping operations lead to less imbalances among phases, while the time of solving r-LAPB grows exponentially⁴. Figure 1.3 clearly shows the major improvement of performance happens at the stage of applying r-PB and r-LAPB with one swapping per day. Improvements of allowing more swapping actions are marginal at the cost of higher computational burden and possible extra cost on human resources and maintenance.

We also examine the optimal solution of r-PB and r-LAPB (Figure 1.4). When allowing one swapping per day, all 28 switchings in 30 days happen on 18 out of 74 loads (Figure 1.4b). Many loads remain unchanged and some loads have more frequent phase swapping operations than others. Figure 1.5 demonstrates the case where two swapping actions are allowed per day, fives loads are swapped much more frequently than the others (17.3% of 299 actions in 150 days, whereas the remaining 69 loads are switched only 3-4 times in 150 days on average.). Automatic phase swapping devices could be installed at these locations for more efficient and frequent responses.

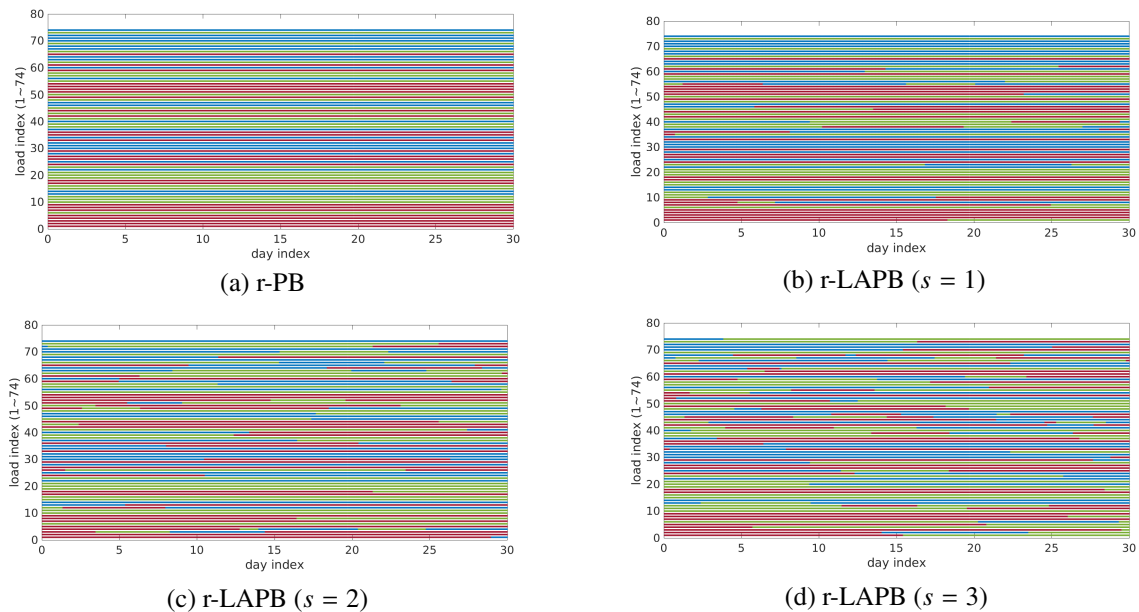


Figure 1.4: Display of Optimal Solutions (ABC phases are color-coded, red:phase A, blue:phase B, green:phase C)

⁴The r-LAPB with $s = 4$ typically requires around 10 ~ 12 hours to solve one instance.

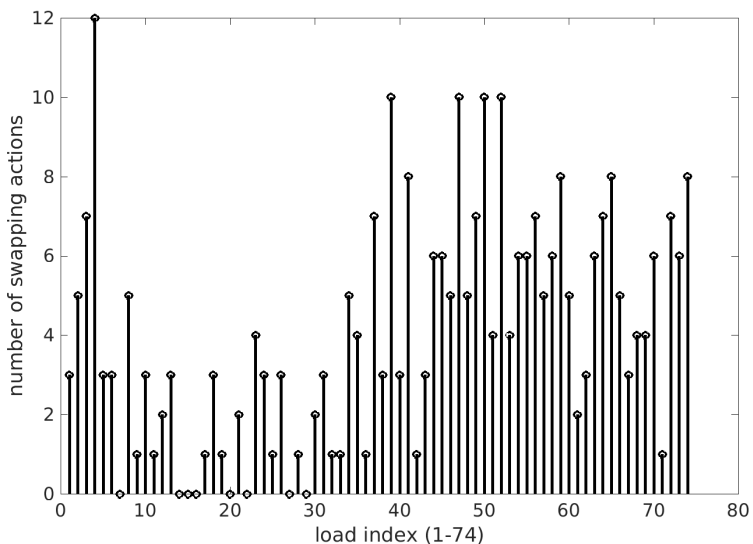


Figure 1.5: Phase Swapping Actions of Each Load (results of r-LAPB ($s = 2$) running for 150 days)

1.5 Discussions

1.5.1 Uncertainty Sets

In this paper, the uncertainty sets (1.13)-(1.14) we use are a special case of polyhedral uncertainty sets. We do not capture yet potential correlations among different loads, as shown in Figure 1.2a. Other choices of uncertainty sets might outperform current ones and reduce conservativeness, e.g. central limit theorem based polyhedral sets [22], ellipsoidal uncertainty sets [34], cardinality constrained uncertainty sets [35], and constructing polyhedral uncertainty sets from data [36].

1.5.2 Approximation Algorithms

All our formulations of phase balancing problems are mixed integer programs, which are in general computationally intractable. One of the classical problems in combinatorial optimization is *minimum makespan scheduling* that attempts to run a given set of jobs on a fixed number of parallel machines such that total time, i.e. the makespan, to complete jobs on any machine is minimized [37]. Minimizing the maximum total load on any phase can then be viewed as makespan scheduling where the given set of jobs is simply the various loads, and the three parallel identical machines are the three phase lines. It is an open question to adapt known approximation algorithms for the minimum makespan scheduling problem (or to develop new methods) to the robust framework while incorporating switching costs. Deterministic phase balancing (d-PB) can also be seen as the optimization version of the k -partition problem [38], that attempts to divide n integers into k subsets such that the total sum of each subset is close to each other. This problem is a generalization of the three phase balancing problem, and might provide useful insights as well.

1.5.3 Multi-phase Loads

It is easy to extend current phase balancing problems for the consideration of multi-phase loads. For deterministic phase balancing (1.6), we could define variable $a^{(1)}$, $b^{(1)}$ and $c^{(1)}$ for single phase loads, $a^{(2)}$, $b^{(2)}$ and $c^{(2)}$ for two-phase loads, $a^{(3)}$, $b^{(3)}$ and $c^{(3)}$ for loads connecting to all three phases. Instead of constraint (1.6e), we have the following constraints:

$$\begin{aligned} a^{(1)} + b^{(1)} + c^{(1)} &= \mathbf{1}, \\ a^{(2)} + b^{(2)} + c^{(2)} &= 2 \cdot \mathbf{1}, \quad \text{and} \\ a^{(3)} + b^{(3)} + c^{(3)} &= 3 \cdot \mathbf{1}. \end{aligned}$$

1.6 Concluding Remarks

In this paper, we advance the conventional phase balancing problem to a robust look-ahead optimization framework that pursuits balanced phases in the presence of uncertainties. It is shown that imbalances among phases could be significantly reduced at the cost of a limit number of phase swapping operations. Many interesting directions are open for future research. For example, choosing different uncertainty sets for r-LAPB could take advantage of strong correlation among some loads. Future works also include designing approximation algorithms with optimality guarantees and exploring the benefits of controlling distributed generations [39–41], electric vehicles [42–44], energy storage [29, 45–47] and demand response [48–51].

Acknowledgement

This work was supported in part by Power Systems Engineering Research Center (PSERC) and in part by the Simons Institute for the Theory of Computing. This work was partially done while the authors were visiting the Simons Institute for the Theory of Computing, UC Berkeley, and we would like to acknowledge the Gordon and Betty Moore Foundation for their generous support.

1.7 Appendix: Equivalent Formulation of Robust Look-ahead Phase Balancing

Formulation (1.11) is equivalent with the following:

$$\text{minimize } u + \lambda v \tag{1.15a}$$

$$\text{subject to } h_t^\top p_a[t] \leq u, \quad H_t^\top p_a[t] = a[t] - \frac{\mathbf{1}}{3}, \tag{1.15b}$$

$$h_t^\top q_a[t] \leq u, \quad H_t^\top q_a[t] = \frac{\mathbf{1}}{3} - a[t], \tag{1.15c}$$

$$h_t^\top p_b[t] \leq u, \quad H_t^\top p_b[t] = b[t] - \frac{\mathbf{1}}{3}, \tag{1.15d}$$

$$h_t^\top q_b[t] \leq u, \quad H_t^\top q_b[t] = \frac{\mathbf{1}}{3} - b[t], \tag{1.15e}$$

$$h_t^\top p_c[t] \leq u, \quad H_t^\top p_c[t] = c[t] - \frac{\mathbf{1}}{3}, \quad (1.15f)$$

$$h_t^\top q_c[t] \leq u, \quad H_t^\top q_c[t] = \frac{\mathbf{1}}{3} - c[t], \quad (1.15g)$$

$$t = 1, 2, \dots, T_1,$$

$$h_t^\top p_a[t] \leq v, \quad H_t^\top p_a[t] = a[T_1] - \frac{\mathbf{1}}{3}, \quad (1.15h)$$

$$h_t^\top q_a[t] \leq v, \quad H_t^\top q_a[t] = \frac{\mathbf{1}}{3} - a[T_1], \quad (1.15i)$$

$$h_t^\top p_b[t] \leq v, \quad H_t^\top p_b[t] = b[T_1] - \frac{\mathbf{1}}{3}, \quad (1.15j)$$

$$h_t^\top q_b[t] \leq v, \quad H_t^\top q_b[t] = \frac{\mathbf{1}}{3} - b[T_1], \quad (1.15k)$$

$$h_t^\top p_c[t] \leq v, \quad H_t^\top p_c[t] = c[T_1] - \frac{\mathbf{1}}{3}, \quad (1.15l)$$

$$h_t^\top q_c[t] \leq v, \quad H_t^\top q_c[t] = \frac{\mathbf{1}}{3} - c[T_1], \quad (1.15m)$$

$$t = T_1 + 1, T_1 + 2, \dots, T_2,$$

$$-w_a[t] \leq a[t] - a[t-1] \leq w_a[t], \quad (1.15n)$$

$$-w_b[t] \leq b[t] - b[t-1] \leq w_b[t], \quad (1.15o)$$

$$-w_c[t] \leq c[t] - c[t-1] \leq w_c[t], \quad (1.15p)$$

$$\sum_{t=1}^{T_1} (\mathbf{1}^\top w_a[t] + \mathbf{1}^\top w_b[t] + \mathbf{1}^\top w_c[t]) \leq 2s, \quad (1.15q)$$

$$a[t] + b[t] + c[t] = \mathbf{1}, \quad (1.15r)$$

$$a[t], b[t], c[t] \in \{0, 1\}^n, u, v \in \mathbb{R}_+, \quad (1.15s)$$

$$w_a[t], w_b[t], w_c[t] \in \mathbb{R}_+^n \quad (1.15t)$$

$$t = 1, 2, \dots, T_1,$$

$$p_a[t], p_b[t], p_c[t], q_a[t], q_b[t], q_c[t] \in \mathbb{R}_+^k, \quad (1.15u)$$

$$t = 1, 2, \dots, T_2.$$

2. Chance-Constrained Optimal Reactive Power Dispatch

The uncertainties from deepening penetration of renewable energy resources have already shown to impact not only the market operations, but also the physical operations in large power systems. It is demonstrated that deterministic modeling of wind would lead to voltage insecurity in the reality where wind fluctuates. This could render deterministic control of reactive power ineffective. As an alternative, we propose a chance-constrained formulation of optimal reactive power dispatch which considers the uncertainties from both renewables and contingencies. This formulation of a chance constrained optimal reactive power dispatch (cc-ORPD) offers system operators an effective tool to schedule voltage support devices such that the system voltage security can be ensured with quantifiable level of risk. The cc-ORPD problem is a Mixed-Integer Non-Linear Programming (MINLP) problem with a joint chance constraint and is extremely challenging to solve. Using the Big-M approach and linearized power flow equations, the original cc-ORPD problem is approximated as a Mixed-Integer Linear Programming (MILP) problem, which is efficiently solvable. Case studies are conducted on a modified IEEE 24-bus system to investigate the optimal operating schedule under uncertainties and the out-of-sample violation probability.

2.1 Introduction

2.1.1 Background

The high variability and limited predictability of renewables impose new challenges on the secure and reliable operation of power systems. There has been a substantial amount of literatures showing that deep penetration of renewables could jeopardize the security and reliability of power systems [52–54]. For example, the rapid increase and stochastic nature of renewables might lead to voltage issues, which could be severe when a stressed system is lack of reactive support. An Optimal Reactive Power Dispatch (ORPD) problem is often formulated for better voltage profiles [52–54]. The ORPD problem aims at finding optimal settings of current installed Reactive Power Support Devices (RPSDs) such as SVCs and Capacitor Banks to ensure system voltage constraints [55]. Although numerous papers have studied the ORPD problem, most of them adopt a deterministic formulation and uncertainties from wind are ignored.

In this paper, we propose a framework for optimal reactive power dispatch considering joint uncertainties from wind and contingencies. The proposed framework is built upon chance-constrained programming, which is a natural and efficient tool for decision making in an uncertain environment.

2.1.2 Chance Constrained Programming

Problem (2.1) is the typical form of a single-stage chance-constrained program (CCP):

$$\min_x c^\top x \quad (2.1a)$$

$$\text{s.t. } Ax \geq b \quad (2.1b)$$

$$\mathbb{P}_\omega \left(\begin{array}{l} G(\omega)x \leq h(\omega) \\ x \in \mathbb{R}^n \end{array} \right) \geq 1 - \epsilon \quad (2.1c)$$

Problem (2.1) aims at finding a cost-minimizing strategy while satisfying a set of deterministic and probabilistic constraints. Without loss of generality [56], we assume the objective takes linear form $c^\top x$. Decision variables are denoted by x , and Eqn. (2.1b) is the *deterministic* constraint on x . Uncertainties appear as variable $\omega \in \mathbb{R}^m$, and the chance constraint Eqn. (2.1c) requires the inner constraint $G(\omega)x \leq h(\omega)$ to be satisfied with probability at least $1 - \epsilon$.

CCPs are often challenging to solve for the following two reasons: (1) the feasible region of a CCP is usually non-convex [25]; and (2) it is NP-hard to accurately calculate the probability in the chance-constraint [57]. There are four typical methods to get approximately optimal solutions to CCPs: (1) deriving a *deterministic equivalent* optimization problem [58, 59]; (2) *convex approximation* [25]; (3) *scenario approach* [56]; and (4) *Big-M approach* [60–62]. Because the cc-ORPD problem is a MINLP problem, the Big-M approach, which is a favorable choice to handle integer variables in CCPs, is selected to solve cc-ORPD in this paper. More details on the Big-M approach is provided in Section 2.3.

2.1.3 Chance-constrained Programs in Power Systems

There are many applications of CCPs on power system problems: chance-constrained DCOPF (cc-DCOPF) [51, 63–66], chance-constrained Unit Commitment (cc-UC) [67, 68], using chance-constrained programming to handle contingencies in power systems [69, 70]. In this paper, we formulate a chance-constrained Optimal Reactive Power Dispatch (cc-ORPD) problem to address the voltage security issue induced by the deep penetration of renewables and potential contingencies. The cc-ORPD problem is unique in the following three aspects: (1) It is built upon a more accurate model of power system (i.e. AC power flow) rather than the simplified DC power flow model, which appears in most of literatures [63, 64, 67–69]. (2) The cc-ORPD problem considers the optimal operation of both continuous and discrete state voltage support devices. While in [71], only continuous-state devices (e.g. SVCs) are being considered. (3) The cc-ORPD problem ensures voltage security with respect to the joint distribution of contingencies and wind uncertainties. Whereas most literatures handling contingencies via CCPs [68–70] are based on DC power flow model. As a result, they are fundamentally incapable of addressing voltage-related issues.

The remainder of this paper is organized as follows: Section 2.2 discusses the impacts of wind uncertainties on voltage security. Section 2.3 introduces the Big-M approach to solve CCPs. Motivated by the discussion in Section 2.2, we formulate a cc-ORPD problem in

Section 2.4. Section 2.4 also elaborates how to derive a computationally tractable form of the cc-ORPD problem via the Big-M approach. Case studies and concluding remarks are presented in Section 2.5 and Section 2.6, respectively.

2.2 Impacts of Wind Uncertainties on Voltage Security

2.2.1 Wind Farm Modeling

The wind farm is often modeled as a negative real load or pure real power generator in most literatures. While at most Independent System Operators (ISOs) in the US, wind farms are required to provide some reactive support to reduce voltage issues. In this paper, the wind farm is modeled as a negative load with constant power factor 0.95. Let $P_W \in \mathbb{R}^{|\mathcal{W}|}$ and $Q_W \in \mathbb{R}^{|\mathcal{W}|}$ denote the forecast value of a set of wind farms \mathcal{W} . And $\xi \in \mathbb{R}^{|\mathcal{W}|}$ represents the forecast errors of wind farms, $\xi \in \Xi$ is a random variable with underlying distribution Ξ . The actual output of wind farm w is $(P_{W,w} + jQ_{W,w})(1 + \xi_w), \forall w \in \mathcal{W}$ and also random. In this paper, we assume the underlying distribution Ξ is unknown but fixed. We also assume that the power factor is maintained at 0.95 for any wind fluctuations.

2.2.2 A Linear Approximation

Reference [9] shows that the voltage magnitudes of PQ buses become uncertain with wind fluctuations ξ . Fig. 2.1 presents the voltage magnitudes with respect to wind uncertainties in a modified IEEE 24-bus system [9]. The blue curve in Fig. 2.1 is obtained by solving a series of power flow

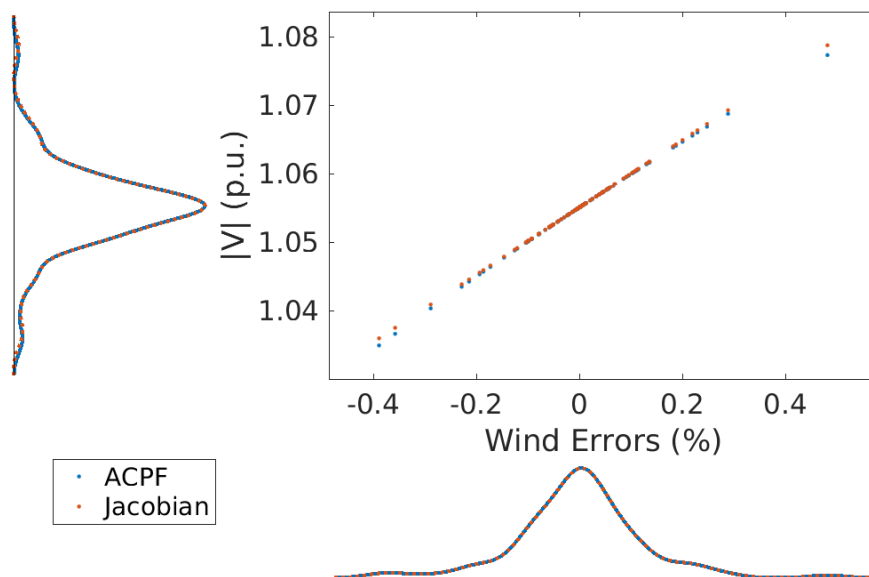


Figure 2.1: Impacts of Wind Uncertainties on Voltage Magnitudes.

equations, which is computationally expensive. Reference [9] proposes an approximation method using power flow Jacobian matrix to estimate the voltage magnitude changes to wind fluctuations. The red curve in Fig. 2.1 is calculated using the approximation method in [9]. Although the relationship between voltage magnitudes and wind fluctuation is fundamentally non-linear, Fig. 2.1 shows that we can get satisfying approximation using linearized power flow equations.

2.3 Big-M Approach to Solve CCPs

Given a two-stage chance-constrained program:

$$\min_{x, y(\omega)} c^\top x + F[y(\omega)] \quad (2.2a)$$

$$\text{s.t. } Ax \geq b \quad (2.2b)$$

$$\mathbb{P}_\omega \left(G(\omega)x + L(\omega)y(\omega) \leq h(\omega) \right) \geq 1 - \epsilon \quad (2.2c)$$

$$x \in \mathbb{R}_+^{n_1} \times \mathbb{Z}_+^{n_2}, y(\omega) \in \mathbb{R}_+^{n_3}$$

The first stage variable x could take both continuous and integer values. Notice that the second stage variable y depends on the realization of variable ω , thus it is denoted by $y(\omega)$.

With the well-known ‘‘Big-M’’ approach [60–62], Problem (2.2) could be reformulated as a *deterministic* Big-M Mixed 0 – 1 Integer Program:

$$\min_{x, y^k, z_k} c^\top x + F[y^k] \quad (2.3a)$$

$$\text{s.t. } Ax \geq b \quad (2.3b)$$

$$G(\omega^k)x + L(\omega^k)y^k - Mz_k \leq h^k \quad (2.3c)$$

$$\sum_{k=1}^N \pi^k z_k \leq \epsilon \quad (2.3d)$$

$$x \in \mathbb{R}_+^{n_1} \times \mathbb{Z}_+^{n_2}, y(\omega^k) \in \mathbb{R}_+^{n_3}, z^k \in \{0, 1\}$$

M is a sufficiently large coefficient and N scenarios are drawn from Ω : $\omega^1, \omega^2, \dots, \omega^N \in \Omega$. The key idea of the Big-M approach is quite simple: for scenario ω^k , if $z_k = 0$, then Eqn. (2.3c) becomes $G(\omega^k)x + L(\omega^k)y^k \leq h^k$; if $z_k = 1$, then Eqn. (2.3c) becomes $-M \leq h^k$, which is always true if M is large enough. In essence, $z_k = 0$ indicates the constraint is retained and $z_k = 1$ indicates violations are allowed for scenario ω^k . The chance constraint $\mathbb{P}_\omega(\dots) \geq 1 - \epsilon$ is approximated by Eqn. (2.3d).

2.4 Chance-constrained Optimal Reactive Power Dispatch

2.4.1 Deterministic Optimal Reactive Power Dispatch

Our previous work [9] solved a look-ahead (deterministic) optimal reactive power dispatch (LA-det-ORPD) problem with voltage security constraints. Problem (2.4) is a simplified version (only one snapshot) of the LA-det-ORPD problem in [9].

$$\min \quad h_B(Q_B) + h_C(Q_C) + \lambda \sum_{c=0}^{n_c} \gamma^c P_L^c \quad (2.4a)$$

$$\text{s.t. } P^c = A_G^c(P_G + \eta^c P_\delta^c) + A_W P_W - A_D P_D, \forall c \quad (2.4b)$$

$$Q^c = A_G^c Q_G^c + A_C Q_C + A_B Q_B - A_D Q_D, \forall c \quad (2.4c)$$

$$P_\delta^c = \mathbf{1}^\top (A_D P_D - A_G^c P_G - A_W P_W), \forall c \quad (2.4d)$$

$$P_i^c = \sum_{j=1}^{n_b} |V_i^c| |V_j^c| |Y_{ij}| \cos(\theta_i^c - \theta_j^c - \phi_{ij}), \forall c, i \quad (2.4e)$$

$$Q_i^c = \sum_{j=1}^{n_b} |V_i^c| |V_j^c| |Y_{ij}| \sin(\theta_i^c - \theta_j^c - \phi_{ij}), \forall c, i \quad (2.4f)$$

$$P_L^c = \sum_{l=1, l: i \sim j}^{n_l} g_l (|V_i^c|^2 + |V_j^c|^2 - 2|V_i^c| |V_j^c| \cos(\theta_i^c - \theta_j^c)), \forall c \quad (2.4g)$$

$$|V^c|^- \leq |V^c| \leq |V^c|^+ \quad (2.4h)$$

$$Q_B \in \{0, Q_B^+\}, \quad Q_C^- \leq Q_C \leq Q_C^+ \quad (2.4i)$$

$$Q_G^- \leq Q_G^c \leq Q_G^+ \quad (2.4j)$$

$$i, j = 1, 2, \dots, n_b, \quad c = 0, 1, 2, \dots, n_c$$

The objective of Problem (2.4) is to minimize the operation costs of RPSDs and transmission losses while ensuring voltage security in n_c contingency scenarios. All variables with superscript c belong to contingency scenario c ¹. In this paper, we focus on the $N - 1$ contingency of losing generators², which are modeled by the adjacency matrix of generators A_G^c . Let A_G^0 be the adjacency matrix in the normal operating condition (i.e. no contingency), A_G^c is obtained by setting the c th column of A_G^0 to zeros.

The decision variables in Problem (2.4) include the operating states of *discrete* RPSDs Q_B (e.g. shunt capacitors), those of *continuous* RPSDs Q_C (e.g. SVCs) and the voltage set-points of generators (i.e. voltage magnitudes $|V^c|$ of PV buses). Eqn. (2.4e) and Eqn. (2.4f) are the nodal power balance constraints, P^c (Q^c) is the nodal real (reactive) power injection into the network.

$A_B \in \mathbb{R}^{n_b \times n_B}$, $A_C \in \mathbb{R}^{n_b \times n_C}$, $A_D \in \mathbb{R}^{n_b \times n_D}$, $A_G^c \in \mathbb{R}^{n_b \times n_g}$ and $A_W \in \mathbb{R}^{n_b \times n_W}$ are adjacency matrices of related components. If component k is connected with bus i , then $A(i, k) = 1$, otherwise $A(i, k) = 0$. Alternating Current (AC) power flow equations are depicted in Eqn. (2.4e) and Eqn.(2.4f). $Y_{ij} \angle \phi_{ij} \in \mathbb{C}$ is associated with line (i, j) (from bus i to bus j) in the admittance matrix Y . Losing generators causes significant real power imbalance P_δ^c , we adopt the *affine control* [63] scheme to proportionally allocate P_δ^c to each generator (i.e. $P_G + \eta^c P_\delta^c$). This guarantees the balance of real power after contingency [9, 63].

¹For simplicity, the normal operating condition is denoted by $c = 0$.

²Since transmission line failures change the system topology thus the Y matrix in Eqn. (2.4e) and Eqn. (2.4f), we could simply modify the Y matrix to be Y^c to model the cases of losing transmission lines. For simplicity, we only focus on generator contingencies in this paper.

Eqn. (2.4g) calculates the real power losses and Eqn. (2.4h) is the *voltage security* constraints, which typically require the voltage magnitudes within desired ranges under a set of plausible contingency scenarios [72]. In this paper, we use [0.95, 1.05] for normal operation analysis ($c = 0$) and [0.9, 1.1] for contingency analysis ($c = 1, 2, \dots, n_c$). Eqn. (2.4i) and Eqn. (2.4j) are the capacity constraints for RPSDs and generators.

2.4.2 Chance-constrained Optimal Reactive Power Dispatch

Motivated by the discussion in Section 2.2, we formulate a chance-constrained Optimal Reactive Power Dispatch (cc-ORPD) problem to ensure the voltage security of the system with respect to wind uncertainties $\xi \in \Xi$ and contingencies $A \in C$. The cc-ORPD problem (Problem (2.5)) enhances the det-ORPD problem by adding a *joint* chance constraint Eqn. (2.5e). The violation probability in Eqn. (2.5e) *explicitly* quantifies the potential risk of voltage insecurity given the joint distribution of wind and contingencies $C \times \Xi$.

$$\min h_B(Q_B) + h_C(Q_C) + \lambda \mathbb{E}_{C \times \Xi} [P_L(c, \xi)] \quad (2.5a)$$

$$\text{s.t. } P = A_G(c)P_G - A_G(c)\eta(c)P_\delta - A_D P_D + A_W \text{diag}(P_W)(1 + \xi) \quad (2.5b)$$

$$Q = A_G(c)Q_G + A_C Q_C + A_B Q_B - A_D Q_D + A_W \text{diag}(Q_W)(1 + \xi) \quad (2.5c)$$

$$\text{Power Flow Equations: Eqn. (2.4e), (2.4f), (2.4g)} \quad (2.5d)$$

$$\mathbb{P}_{C \times \Xi} \left(|V(c)|^- \leq |V(c, \xi)| \leq |V(c)|^+ \text{ for PQ buses} \right. \\ \left. \text{and } Q_G^- \leq Q_G(c, \xi) \leq Q_G^+ \right) \geq 1 - \epsilon \quad (2.5e)$$

$$|V(c)|^- \leq |V| \leq |V(c)|^+ \text{ for PV buses} \quad (2.5f)$$

$$Q_B \in \{0, Q_B^+\}, \quad Q_C^- \leq Q_C \leq Q_C^+ \quad (2.5g)$$

$$i, j = 1, 2, \dots, n_b, \quad c = 0, 1, 2, \dots, n_c$$

The cc-ORPD problem is a two-stage chance-constrained programming problem. The *first-stage* variables are the operating states of RPSDs (Q_B and A_C) and the voltage set points of generators (i.e. voltage magnitudes of PV buses). The *second-stage* variables include the nodal injection (P and A), power imbalance P_δ , total line losses P_L , reactive generation A_G , as well as the voltage magnitudes and angles of PQ buses ($|V|$ and \angle). Since the parameters A_G^c and η^c depend on the contingency c , we change the notation to $A_G(c)$ and $\eta(c)$ for better understanding. Please notice that Eqn. (2.5b)-(2.5d) are equality constraints associated with random variable c and ξ , therefore the second-stage variables (e.g. P and P_L) also become random variables³.

The cc-ORPD problem is very challenging to solve for the following three reasons: (1) some decision variables are binary, thus the feasible region of cc-ORPD is naturally non-convex;

³More rigorous notations should denote the second-stage variables are functions of c and ξ (e.g. $P(c, \xi)$ and $P_L(c, \xi)$). To avoid verbose notations, we only emphasize this in the chance constraint Eqn. (2.5e).

(2) the power flow equations are non-linear equations, which further increase the difficulty of solving cc-ORPD; and (3) the chance constraint Eqn. (2.5e) induces computationally intractable issues as discussed in Section 2.1.2.

The third difficulty could be handled via the Big-M approach introduced in Section 2.3. Given a set of scenarios $s^1, s^2, \dots, s^{|S|}$, where $S = C \times \Xi$ and each scenario $s^i = (c, \xi)^i \in S$. We introduce binary variables $z^i \in \{0, 1\}$ for each scenario $s^i = (c, \xi)^i$. The chance-constraint in cc-ORPD could be re-written as a set of *deterministic* inequality constraints with binary variables z^i . Because we want to ensure the voltage security for all contingency scenarios C , instead of drawing scenarios $(c, \xi)^i$ from $C \times \Xi$, we draw samples ξ^1, ξ^2, \dots only from Ξ , and combine them with n_c contingency scenarios utilizing the fact that the generator contingency c and wind uncertainties ξ are independent. More specifically, let π_c denote the probability that contingency c happens, and ξ^k ($k = 1, 2, \dots, N$) are the wind scenarios. The cc-ORPD problem is reformulated as Problem (2.6), where variables with superscripts c,k are associated with contingency c and wind scenario ξ^k .

$$\min \quad h_B(Q_B) + h_C(Q_C) + \lambda \sum_{c=0}^{n_c} \gamma^{c,k} \frac{1}{N} \sum_{s=1}^N P_L^{c,k}(P_W^s) \quad (2.6a)$$

$$\text{s.t. } P^{c,k} = A_G^c P_G - A_G^c \eta^c P_\delta^{c,k} - A_D P_D + A_W \text{diag}(P_W)(1 + \xi^k), \forall c, k \quad (2.6b)$$

$$Q^{c,k} = A_G^c Q_G^{c,k} + A_C Q_C + A_B Q_B - A_D Q_D + A_W \text{diag}(Q_W)(1 + \xi^k), \forall c, k \quad (2.6c)$$

$$P_\delta^{c,k} = \mathbf{1}^\top A_G^c P_G - \mathbf{1}^\top \overline{P_G} + P_W^\top \xi^k, \forall c, k \quad (2.6d)$$

$$P_i^{c,k} = \sum_{j=1}^{n_b} |V_i^{c,k}| |V_j^{c,k}| |Y_{ij}| \cos(\theta_i^{c,k} - \theta_j^{c,k} - \phi_{ij}), \forall c, s, i \quad (2.6e)$$

$$Q_i^{c,k} = \sum_{j=1}^{n_b} |V_i^{c,k}| |V_j^{c,k}| |Y_{ij}| \sin(\theta_i^{c,k} - \theta_j^{c,k} - \phi_{ij}), \forall c, s, i \quad (2.6f)$$

$$P_L^{c,k} = \sum_{l=1}^{n_l} g_l (|V_i^{c,k}|^2 + |V_j^{c,k}|^2 - 2|V_i^{c,k}| |V_j^{c,k}| \cos(\theta_i^{c,k} - \theta_j^{c,k})), \forall c, k \quad (2.6g)$$

$$|V^{c,k}| - M z_{c,k} \leq |V^{c,k}|^+, \forall c, k \quad (2.6h)$$

$$|V^{c,k}| + M z_{c,k} \geq |V^{c,k}|^-, \forall c, k \quad (2.6i)$$

$$Q_G^{c,k} - M z_{c,k} \leq Q_G^+, \forall c, k \quad (2.6j)$$

$$Q_G^{c,k} + M z_{c,k} \geq Q_G^-, \forall c, k \quad (2.6k)$$

$$Q_B \in \{0, Q_B^+\}, \quad Q_C^- \leq Q_C \leq Q_C^+ \quad (2.6l)$$

$$\sum_{k=1}^N \frac{1}{N} \sum_{c=0}^{n_c} \pi_c z_{c,k} \leq \epsilon \quad (2.6m)$$

$$i, j = 1, 2, \dots, n_b, \quad c = 0, 1, 2, \dots, n_c, k = 1, 2, \dots, N$$

2.4.3 Linearized cc-ORPD

Problem (2.6) is a Mixed Integer Non-Linear Programming (MINLP) problem, which is still computationally intractable. But the major difficulty here comes from the non-linear power flow equations. As shown in Section 2.2.2, we could obtain satisfying approximations via linearized power flow equations. Thus Eqn. (2.6e) and (2.6f) are linearized with respect to a known operating point (e.g. power flow solutions of a previous snapshot). Our future works include exploring other possible approaches to handle non-linearity of power flow equations (e.g. convex relaxation). Problem (2.9) is obtained by replacing Eqn. (2.6e)-(2.6f) with Eqn. (2.7). It is a Mixed Integer Linear Programming problem and is reliably solvable with commercial solvers.

$$\begin{bmatrix} P - \bar{P} \\ Q - \bar{Q} \end{bmatrix} \approx \begin{bmatrix} \frac{\partial P}{\partial \theta} & \frac{\partial P}{\partial |V|} \\ \frac{\partial Q}{\partial \theta} & \frac{\partial Q}{\partial |V|} \end{bmatrix}_{\bar{P}, \bar{Q}, |\bar{V}|, \bar{\theta}} \times \begin{bmatrix} \theta - \bar{\theta} \\ |V| - |\bar{V}| \end{bmatrix} \quad (2.7)$$

$$P_L - \bar{P}_L \approx \left[\frac{\partial P_L}{\partial \theta} \quad \frac{\partial P_L}{\partial |V|} \right]_{\bar{P}, \bar{Q}, |\bar{V}|, \bar{\theta}} \times \begin{bmatrix} \theta - \bar{\theta} \\ |V| - |\bar{V}| \end{bmatrix} \quad (2.8)$$

$$\min \quad h_B(Q_B) + h_C(Q_C) + \lambda \sum_{c=0}^{n_c} \gamma^{c,k} \sum_{s=1}^N P_L^{c,k}(P_W^s) \quad (2.9a)$$

$$\text{s.t. Eqn. (2.6b), (2.6c), (2.6d)} \quad (2.9b)$$

$$\text{Eqn. (2.7), (2.8)} \quad (2.9c)$$

$$\text{Eqn. (2.6h), (2.6i), (2.6j), (2.6k), (2.6l), (2.6m)}$$

$$\Delta|V|^- \leq |V^{c,k}| - |\bar{V}| \leq \Delta|V|^+ \quad (2.9d)$$

$$\Delta|\theta|^- \leq |\theta^{c,k}| - |\bar{\theta}| \leq \Delta|\theta|^+ \quad (2.9e)$$

$$i, j = 1, 2, \dots, n_b, \quad c = 0, 1, 2, \dots, n_c$$

2.5 Case Study

2.5.1 Settings

Case studies are conducted on a modified IEEE 24-bus system [9]. There are 38 contingencies considered in the case study, each one represents the scenario of losing one generator at a PV bus⁴. We assume the probability of the normal operating condition is $\pi_0 = 90\%$, and each contingency happens with equal probability, i.e. $\pi_c = 10\%/38 = 0.26\%$. By tuning the probabilities π_c s and ϵ , we could achieve a balance between a more economic system and a more secure system. The wind uncertainty ξ is assumed to be Gaussian $\xi \sim \mathcal{N}(0, 5\%)$, from which 100 scenarios ξ^k are drawn and plugged in Problem (2.9). It is worth mentioning that solving Problem (2.9) solely relies on the scenarios ξ^k , it does not require any prior knowledge on the underlying distribution.

⁴If there is only one generator at the PV bus, losing the generator will make it to a PQ bus. For simplicity, we replace it with two generators with half capacities.

2.5.2 Simulation Results

Problem (2.9) was solved via Matlab2016b and Gurobi 7.5 on a Desktop with Intel i7-2600 8-core CPU@3.40GHz and 16GB RAM memory. Gurobi found the optimal solution with 0.0% gap in 330 seconds. The optimal objective value is \$1668.13. Fig. 2.2 demonstrates the optimal voltage set points of generators and the voltage magnitudes of PQ buses in the normal operating condition. The voltage magnitudes of bus 4 and bus 14 are fluctuating due to wind uncertainties, while some buses (e.g. bus 17, 19 and 20) remain almost the same voltage magnitudes.

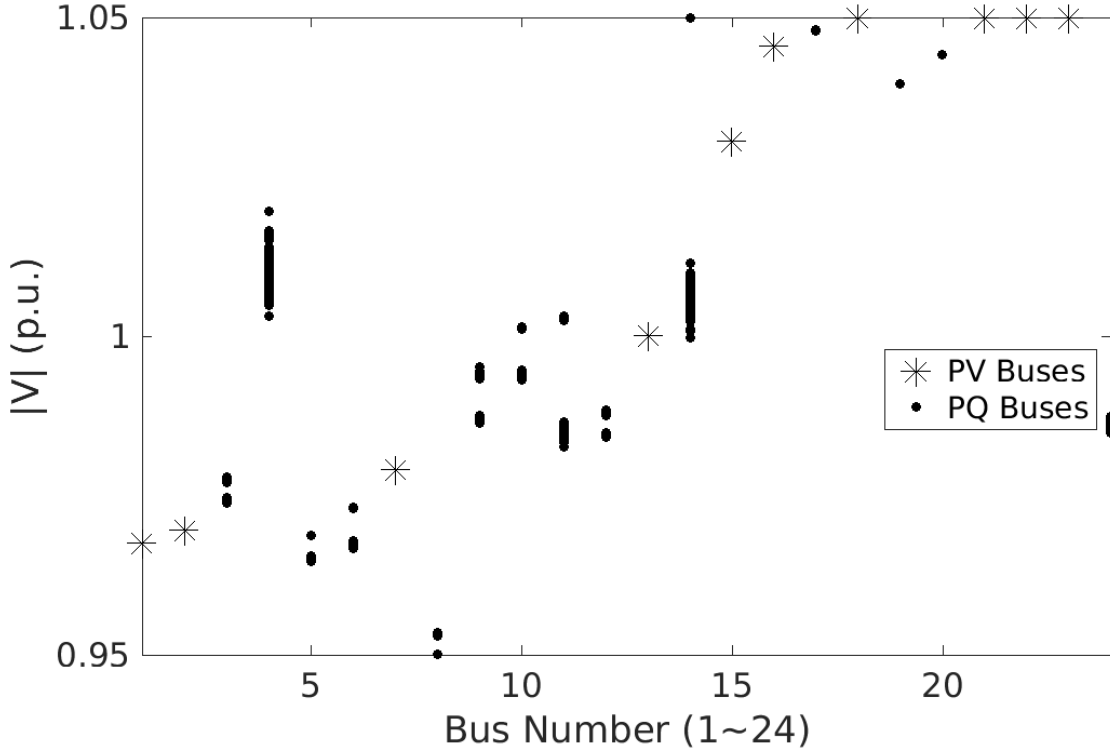


Figure 2.2: Voltage Magnitudes in the Normal Operating Condition.

Besides the optimal solution to the cc-ORPD problem, we are also interested in the actual violation probability $\hat{\epsilon}$. Let $\bar{\epsilon}$ denote the expected violation probability: $\bar{\epsilon} := \sum_{k=1}^{\hat{N}} \frac{1}{\hat{N}} \sum_{c=0}^{n_c} \pi_c z_{c,k}^*$, where $z_{c,k}^*$ is from the optimal solution to Problem (2.9). It is obvious that $\bar{\epsilon} \leq \epsilon$. Let $\hat{\epsilon}$ denote the actual “out-of-sample” violation probability:

$$\hat{\epsilon} := \sum_{k=1}^{\hat{N}} \frac{1}{\hat{N}} \sum_{c=0}^{n_c} \pi_c \mathbf{1}_{Q_G^{c,k} \notin [Q_G^-, Q_G^+] \text{ or } |V^{c,k}| \notin [|V^c|, |V^c|+]} \quad (2.10)$$

where $\mathbf{1}_{\text{conditions}}$ is the indicator function. We generate an independent set of \hat{N} scenarios and calculate the voltage magnitudes and reactive power generations using linearized power flow equations [9] or solving the power flow equations.

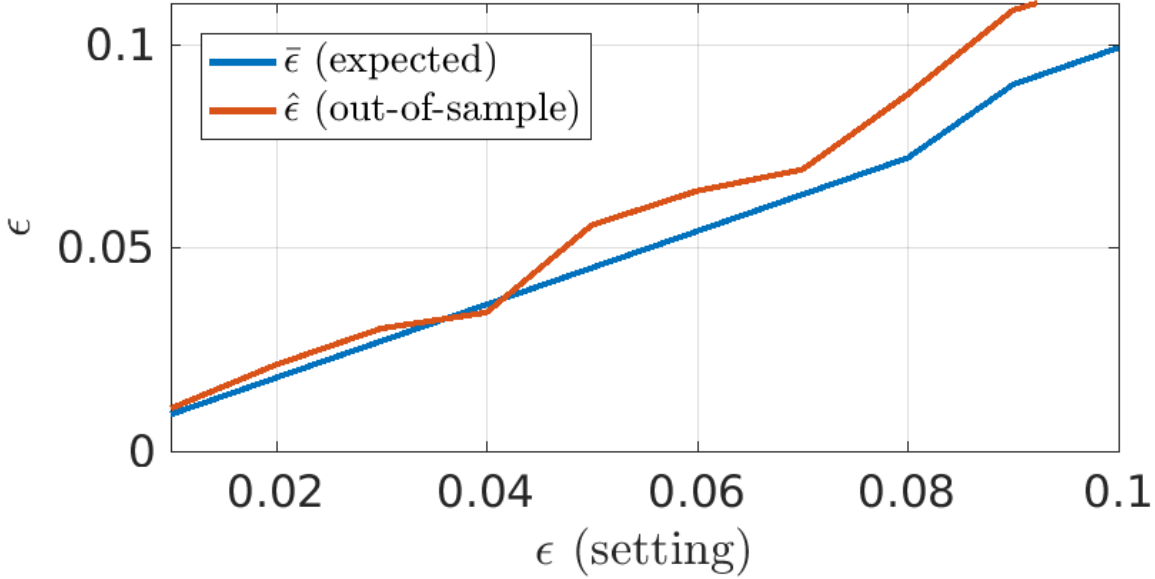


Figure 2.3: Violation Probabilities.

The blue curve in Fig. 2.3 is the expected violation probability $\bar{\epsilon}$ from the optimal solution z^* . And the red line $\hat{\epsilon}$ is calculated on $\hat{N} = 100$ scenarios using linearized power flow equations [9]. The out-of-sample violation probability $\hat{\epsilon}$ is very close to $\bar{\epsilon}$. With a larger number of scenarios embedded in Problem (2.9), the expected $\bar{\epsilon}$ and actual $\hat{\epsilon}$ will be closed to the violation probability ϵ in the chance constraint.

We also compare the results of cc-ORPD (Problem (2.9)) with det-ORPD (Problem (2.4)). With a little sacrifice on the total cost, the cc-ORPD could ensure voltage security with probability 98.8%. While the results of det-ORPD lead to voltage magnitudes lower than the desired lower bound $|V^c|^-$. In the results of det-ORPD, we even observe undesirable low voltage magnitudes in the normal operating condition, which results in the large violation probability in Table 2.1.

Table 2.1: det-ORPD vs cc-ORPD

	det-ORPD	cc-ORPD ($\epsilon = 0.01$)
Objective	1610.2	1668.1
$\hat{\epsilon}$	52.1%	1.2%

2.6 Concluding Remarks

In this paper, we propose a chance-constrained formulation of optimal power reactive dispatch to schedule RPSDs considering uncertainties from wind and contingencies. The cc-ORPD problem is reformulated as a computationally solvable form using the Big-M approach and linearized power flow equations. Case studies demonstrate the effectiveness of the proposed cc-ORPD framework. Future works include investigating convex relaxations of power flow equations

and utilizing improved versions of the Big-M approach [61, 62].

3. Electricity as a Service: Cost Causation-based Utility Rate Model for the Future Distribution Grid

Distribution grids across the world are undergoing profound changes due to advances in energy technologies. Electrification of the transportation sector and the integration of Distributed Energy Resources (DERs) such as photo-voltaic panels and energy storage devices has gained substantial momentum, especially at the edge of the grid. However, the massive transformation in the technological aspects of the grid could directly conflict with existing utility business models and tariff structures applied to retail customers. This paper proposes a restructured business model where the implementation of these grid-edge technologies is aligned with the interest of all stakeholders involved in the electricity ecosystem. This envisions a shift from treating electricity as a commodity where the users are charged based on their volumetric consumption, to treating it as a service provided to the end-user by the utility company based on the principle of cost-causation. The proposed rate structure considers the impact of individual customers on the distribution grid by calculating metrics that contribute directly to the costs incurred by the transmission and distribution utilities (TDUs), namely magnitude and variability of the demand.

3.1 Introduction

Distributed energy resources (DERs) have been integrated to the electric grid edge at an accelerated pace over the past decade. The levelized costs of photo-voltaic (PV) panels and energy storage have dropped significantly and are projected to continue this trend [73]. Behind-The-Meter (BTM) technologies are estimated to make up over 50% of the US energy storage market by 2021, with the deployed energy storage expected to reach 2 GW by then [74].

Despite the fact that end-use demand is projected to increase in the next few decades both in the residential and commercial sectors, there is a significant projected reduction in energy intensity [75]. Further, projections indicate that the growth rate of electricity sales will be diminished due to the significant increase in generation from rooftop PV systems, from both residential and commercial buildings [76]. The adoption of Electric Vehicles (EVs) is also on the rise, with the number of EVs on the road in the US reaching 1.1 million by the end of 2018 [77]. With increased installation of these technologies many consumers are turning into prosumers, thus eroding the revenue stream of the utilities [78].

The rise in DER penetration in markets around the globe makes the following question extremely relevant - are the existing utility business models poised to handle the accelerated pace of DER deployment at the grid edge? This paper addresses customer rate models of Transmission and Distribution Utilities (TDUs) i.e. how they recover their costs from customers. TDUs need to be compensated for their investments and the grid maintenance costs they incur to ensure reliable power supply to all customers. Their compensation is akin to a toll fee for using the TDU's grid infrastructure. This paper focuses on the proper determination and allocation of grid access costs to retail customers, and does not deal with the variable production costs for delivered power (the 'Energy Charge').

Existing TDU charges are a combination of a small portion of fixed charge, coupled with a larger volumetric g/kWh charge - the dotted line in Fig. 3.1 represents the cost curve to consumers of this rate structure [79]. The revenue earned by TDUs is directly proportional to the volume of electricity in kWh that is consumed by the end-users. This rate structure incentivizes TDUs to maximize sales and makes them dependent on the volumetric charge for the bulk of their revenue [80]. With increasing deployment of grid-edge DERs the current rate design could be insufficient since it does not fully account for the rising fixed costs faced by the TDUs [81]. Grid-edge DERs pose a threat to the revenue stream of utility companies in a few different ways. Firstly, the increase in solar PV penetration directly results in reduction of kWh demand from the grid. This reduces the customer's utility bill, even though the utility offers the service of access to the grid at all times, which the PV customer will require when the sun goes down. Secondly, the expansion of participation in net metering has resulted in utilities providing financial compensation for electricity injections from PV to the grid [82]. Costello [83] argues that there are a number of issues with net metering, including that it is inefficient and an unfair cross-subsidy.

The proliferation of Advanced Metering Infrastructure (AMI) technologies provides an enabling platform for retail rate innovations that could improve upon the current volumetric rate structure.

There has been a number of case studies devoted to examining the impact of high DER penetration on regulatory, technological and economic aspects in the distribution grid. The resulting need for utilities to update their business models, and a rebalancing of costs on the electricity value chain from the grid side to behind the meter has been discussed in [84] and [85] respectively. Baak [86] and Pelegry [87] explore the regulatory framework in different parts of the world, and the restructuring that may be required to enable an accelerated transformation towards grid modernization, while Gellings [88] argues that the existing regulatory measures may be adequate to accommodate even a transformed future. Laws et al. [89] indicates that residential PV penetration could reach a substantial number over the next decade. But, they argue that utilities have ample time to change their business model in order to avoid the death spiral. Darghouth et al. [90] shows how various rate design choices can impact the long term cumulative distributed PV deployment.

Burger and Luke [91] provides a comprehensive review of the various business models that exist for various categories of DER technologies. Bird et al. [92] provides an analysis of how different rate structures, namely fixed charges, minimum bills and higher demand rates impact the bills of residential customers in a number of states across the US. Baatz [93] provides a summary of a number of recent studies on various rate structures such as Time-of-Use (TOU), Critical Peak Pricing (CPP) etc. Schwartz [94] presents the pros and cons of various rate designs. Namely, raising fixed charges for all customers may disproportionately impact low-income customers. Minimum bills do not necessarily fix the utility revenue problem. Demand charges are usually applied to the customer's peak demand regardless of whether it is coincident with distribution system demand. Revesz and Unel [95] reviews the net-metering related tariff changes in a number of jurisdictions in the US. They also argue for an approach that values clean distributed energy for its social impacts such as environmental benefits and reduced losses. Faruqui et al. [80] suggests transitioning residential customers to three-part rates, comprising of a monthly fixed charge, a volumetric charge, and a demand charge. In [96] an analysis of BTM storage adoption under a storage-friendly rate is presented.

In [97], a Distribution Network Use-of-System (DNUoS) charge has been proposed, which aids in accurate recovery of distribution utility costs, by capturing the contribution of each user on the network to the system's costs. This paper applies a similar line of thought, by billing the customers based on their individual contributions to system costs.

In view of the above, the key contributions of this paper are as follows:

- A methodology to quantify the impact of individual customers on the grid based on demand magnitude and variability metrics has been proposed
- A novel utility rate mechanism has been formulated, which calculates TDU charges for individual customers based on the cost causation principle
- Numerical case studies have been developed using data from real residential customers with a high penetration of EVs and Solar PVs, to simulate the effect of the proposed rate mechanism
- The deployment of battery storage has been simulated to assess its effect on the grid impact of customers

The rest of the paper is organized as follows: Section 3.2 highlights the deficiencies in the existing utility business model, and describes the design details and mathematical formulation of the proposed billing mechanism. Section 3.3 is a critical comparison of the existing and proposed new utility business models, supported by a case study using real residential customer data. Section 3.4 summarizes the key learnings and the most significant policy implications of the proposed utility business model.

3.2 Methodology and Data

3.2.1 Proposed Utility Business Model

The proposed TDU charge features the introduction of a single grid-access fee, replacing the existing distribution utility charges, which are typically structured as a small fixed charge combined with a large volumetric (\$/kWh) charge. ¹ The uniqueness of this idea lies in how these grid-access fees would be customer-specific; calculated for each customer by taking into account some key parameters that define the impact of said customer to the grid. This impact is quantified through a combination of weighting factors called Grid Impact Factors.

This concept is analogous to an insurance rate model or a credit score, where each customer's rate/credit limit is considered to accurately reflect the risk level taken up by the insurance company / bank by entering into business with said customer. An example of providing appropriate incentives in electricity wholesale markets is FERC Order 755 [98]. Prior to this Order, most ISO markets in the US had a single capacity payment for regulation. Regulation payments were not tied to resource performance. As a result of this rule a two-part payment was

¹Here we consider a deregulated utility in which the variable production costs (Energy Charges) are passed through to the customer, and these are separate from the proposed grid-access fee.

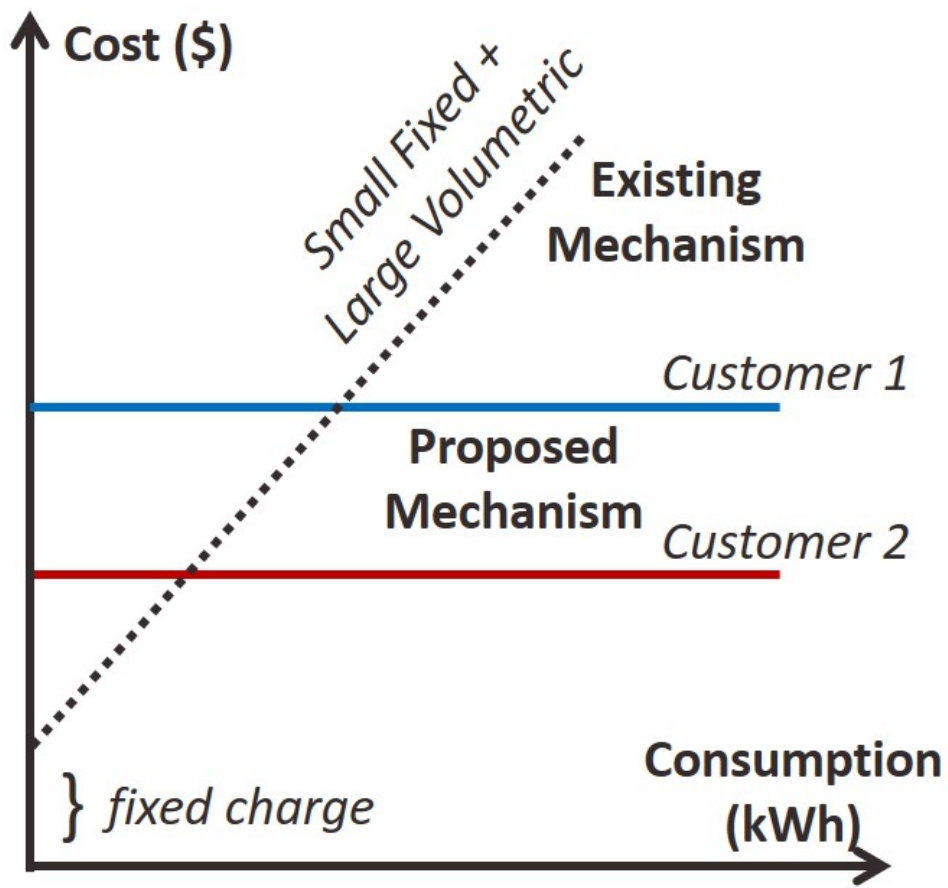


Figure 3.1: Current vs. Proposed TDU Charges: Consumer Cost Curve

enacted, which added a mileage based component that accounts for the performance of the resource, in addition to the capacity based payment.

As is evident from Fig. 3.1, TDU does not have revenue assurance i.e. they have to hope that consumers use more kWh, thus driving up their revenue. However, under the proposed approach the TDU has a steady and assured income from each consumer via the fixed Grid Access Fees. In the figure, Customer 2 has a lower grid impact than Customer 1, and thus is charged a lower Grid Access Fee.

3.2.2 Metrics causing Distribution Grid Investments

In the context of a distribution grid, the installed capacity of the system is a key parameter - it determines how much load can be served. Depending on changing load patterns this limit also dictates the need for capital investment. System capacity requirements are directly dependent on the system Peak Demand to be supplied to the customers. Thus, the "Peak Demand Time Slots" are a critical time for the system. To account for this, a Demand Magnitude Impact Factor W is introduced, that measures the demand impact factor of each home during the peak demand time slots.

$$\begin{aligned} &\text{Demand Impact Factor of Home } i \text{ (} W_i \text{)} \\ &= \text{Total Demand of Home } i \text{ during Peak Slots} \end{aligned} \tag{3.1}$$

Another key concern for the distribution grid is the health of the existing infrastructure. This directly impacts the capital investment and maintenance costs that the TDU incurs. The health of grid infrastructure is correlated to its loading conditions and the fluctuations in demand. These fluctuations are measured using the Demand Variability Impact Factor V , which is the normalized correlation between the variability of individual customers and the variability of total system demand.

$$\begin{aligned} &\text{Variability Impact Factor of Home } i \text{ (} V_i \text{)} \\ &= \text{Normalized Correlation between} \\ &\text{Variability of Home } i \text{ and Total System Variability} \end{aligned} \tag{3.2}$$

3.2.3 Peak Demand Indicator Function

With the objective of making the rate structure as flexible and general as possible, a Peak Indicator Function for Demand has been introduced. This takes as input the present system conditions, the peak threshold for the system conditions, and a strictness parameter k , to deliver an indication of whether the system condition at that time t is considered to be a peak slot or not. When k is very small, the Peak is considered based on a very strict cut-off, whereas if k is larger, the function also begins to consider those time slots where System Demand (S^t) is almost equal to the peak threshold, thus reducing the importance and emphasis placed on an inherently arbitrary definition of peak threshold.

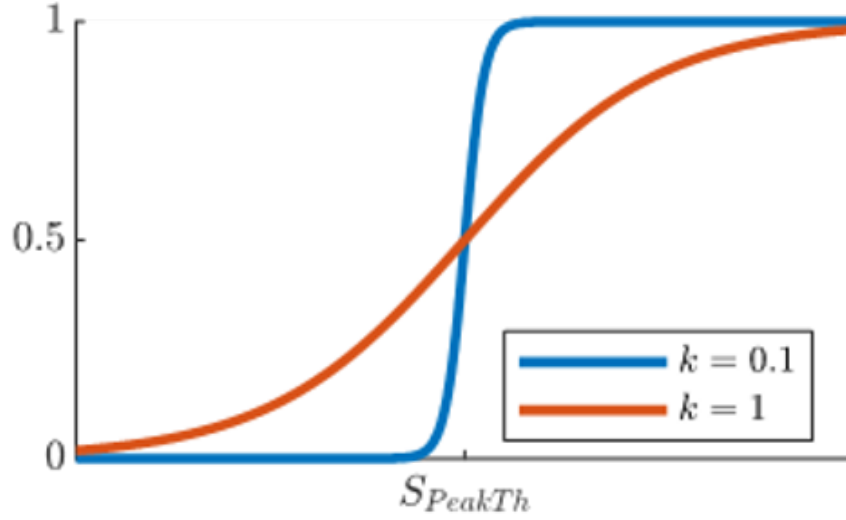


Figure 3.2: Peak Demand Indicator Function μ

Distribution grids have diverse load profiles, even between different feeders within the same TDU service territory. The proposed mechanism provides the TDU the option to use their engineering judgment to select peak thresholds and k values that are best suited for their system conditions.

The Peak Indicator Function has been defined for Peak Demand Magnitude as μ . This is described below.

Peak Demand Indicator Function μ

This function is designed similar to a logistic function, and is centered around the System Peak Threshold value S_{PeakTh} . S_{PeakTh} is calculated based on a percentile value that is set by the TDU. If the peak threshold percentage is set as 15%, then $S_{PeakTh} = 85^{th}$ percentile of System load curve. This means that a given time slot t is defined as a peak demand time slot when $S^t \geq S_{PeakTh}$. In essence, this function returns 1 if it is a peak slot, and 0 if not (Fig 3.2). For a given time t , μ is described as follows:

$$\mu^t = \frac{1}{1 + e^{\frac{-(S^t - S_{PeakTh})}{k}}}$$

3.2.4 Calculating the Grid Impact Factors W and V

Let $X_i^t =$ Demand of user i at time t

$dX_i^t =$ Change in Demand (Variability) of user i between time t and $t - 1$

i.e. $dX_i^t = X_i^t - X_i^{t-1}$

Demand Magnitude Impact Factor W

Demand Magnitude Impact Factor for Customer i (W_i) is the total demand of Customer i during peak demand time slots (defined in Section 3.2.3). The Peak Indicator Function μ is used to determine whether time-step t is a peak or not.

Element-Wise Multiplication

$$W_i^t = X_i^t \cdot \mu^t W_i = \sum_t W_i^t \quad (3.3)$$

Matrix Multiplication

$$W_{N \times 1} = X_{N \times T} \cdot \mu_{T \times 1} N \text{ homes, } T \text{ timesteps} \quad (3.4)$$

Demand Variability Impact Factor V

The Demand Variability Impact Factor for customer i (V_i) is the normalized correlation between the variability of customer i (dX_i) and the variability of total system demand β .

$$V_i = \frac{\sum_t (dX_i^t - \overline{dX_i})(\beta^t - \overline{\beta})}{\sqrt{\sum_t (dX_i^t - \overline{dX_i}) \sum_t (\beta^t - \overline{\beta})}} \quad (3.5)$$

Relative Factor (% Allocation) for each Customer i

$$W_{\text{share } i} = \frac{W_i}{\sum_{j=1}^N W_j} \quad V_{\text{share } i} = \frac{V_i}{\sum_{j=1}^N V_j} \quad (3.6)$$

3.2.5 Calculating the Final Bills

Let $B_{i \text{ total}}^{\text{old}} \rightarrow$ Total TDU Charge of home i calculated in the current method, and $B_{i \text{ total}}^{\text{new}} \rightarrow$ Total TDU Charge of home i calculated in the proposed method.

To calculate TDU Charges for each home under the **current mechanism**, we consider a standard volumetric rate formula for TDU Charges defined below (5 ¢per kWh) ($X_i^t > 0$):

$$B_i^{\text{old}} = \$0.05 \times X_i^t \quad (3.7)$$

In case a home generates more than it consumes at any point in time, i.e. $X_i^t < 0$, the excess electricity is sold back to the grid at a discounted rate of 2 ¢per kWh (Net Metering).

$$B_i^{\text{old}} = -\$0.02 \times X_i^t \quad (3.8)$$

So, the total TDU Charges in the current mechanism for the full 2 year period is calculated as follows.

$$B_{i \text{ total}}^{\text{old}} = \sum_t (B_i^t \text{ old}) \quad (3.9)$$

In the **proposed rate calculation mechanism**, customers are charged a fixed monthly charge based on their Grid Impact Factors. This fixed charge is calculated by starting from the total target revenue for the TDU. This is the reverse approach of the existing mechanism, thus a stark difference from the procedure followed in the current scheme, where the individual customer's rate is based on a fixed formula, and an aggregation of all customers' payments gives the total revenue for the TDU.

It is assumed that the \$/kWh rate is derived from the total target revenue of the system, which is obtained as a result of the current rate case process. This rate case is determined by a joint effort between the TDU and regulator, to ensure accuracy and fairness to TDU and customer alike.

For simplicity, the work in this paper operates under the assumption that the total target revenue is calculated for the full period of assessment - in the case study described in the paper, this period of assessment is 2 years. Further, to make a fair and direct comparison of the current and proposed mechanisms, this total target revenue for the TDU has been fixed as the $B_{i \text{ total}}^{\text{old}}$ value, i.e.,

$$\sum_{i=1}^N B_{i \text{ total}}^{\text{old}} = \sum_{i=1}^N B_{i \text{ total}}^{\text{new}} \quad (3.10)$$

This essentially results in a redistribution of the same final cost among the customers. This is a fair assumption to make because the total target revenue for the current mechanism is calculated through the rate case process, which is assumed to be an accurate reflection of system costs.

Since the new mechanism has to account for two contributing grid impact factors W and V , the importance of these respective weighting factors are determined by the allocation percentage parameters Π_V and Π_W (also determined by the TDU and regulator), defined as follows:

$\Pi_W = \% \text{ Allocation of Total Target Revenue for } W$
 $\Pi_V = \% \text{ Allocation of Total Target Revenue for } V$

And so, finally, the total TDU Charges for each home i as per the new scheme is calculated as a linear combination of the weighting factors scaled with their respective allocation percentage parameters, as follows:

$$B_{i \text{ total}}^{\text{new}} = W_{\text{share } i} \times \Pi_W + V_{\text{share } i} \times \Pi_V \quad (3.11)$$

3.2.6 Data and Case Study System Description

The data used for the results discussed in Section 3.3 is the instantaneous kW demand for 200 residential customers, measured at a resolution of 1-minute. The dataset spanning a period

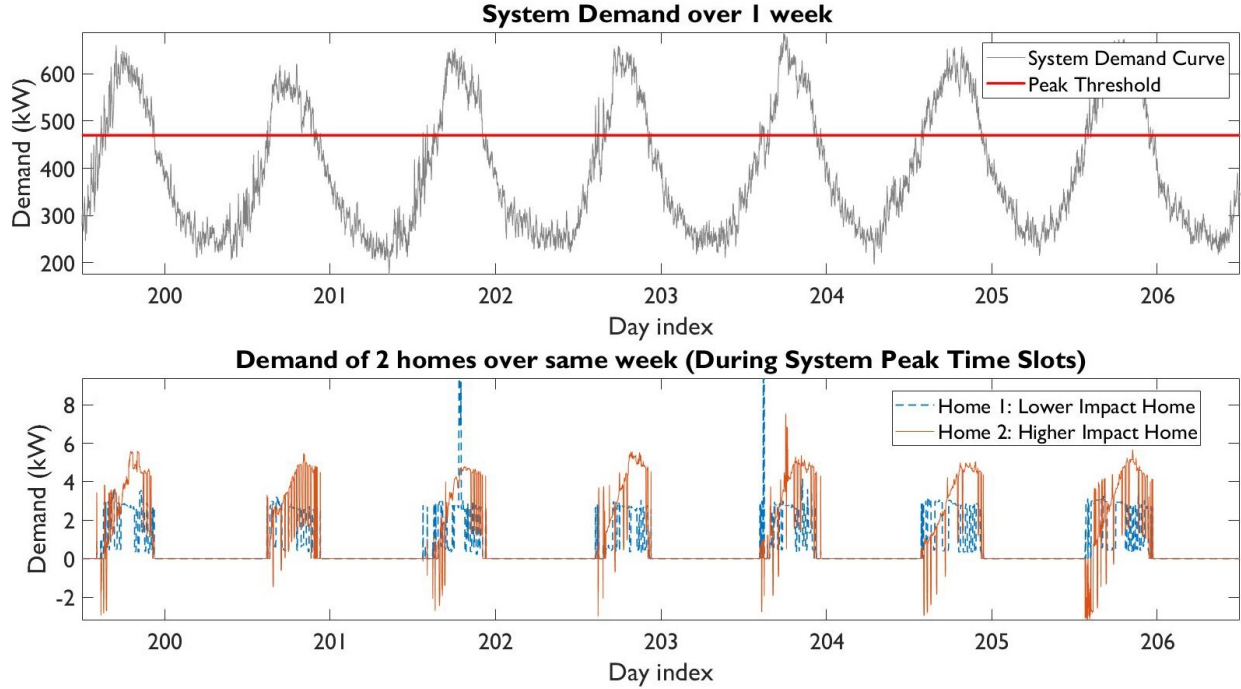


Figure 3.3: System Demand Curve and Comparison of Demand between two homes over 1 week during Peak Time Slots

of two years (from 01-01-2016 to 12-31-2017) was obtained from Pecan Street Dataport [99].

3.3 Results and Discussion

To thoroughly examine the effects of the new billing mechanism, we calculate the TDU Charges for each home in a system of 200 residential demand profiles, with 25% penetration of EVs and PVs each, i.e. 50 EV homes and 50 PV homes among the 200 total homes.

For the purpose of this example, we set the S_{PeakTh} at the 75th percentile of total system demand. Also, the % Allocations of Total Target Revenue Π_W and Π_V are set as 75% and 25% respectively.

3.3.1 Comparing the Performance of Two Homes in the Proposed Mechanism

To illustrate the effects of the proposed scheme, we examine two homes which have a similar TDU Charge in the existing scheme but a significant difference in TDU Charges in the proposed scheme.

In Fig. 3.3 (top), the system demand curve has been plotted along with the Peak Threshold line (red), indicating which intervals are considered to be peak time slots. Fig. 3.3 (bottom) depicts the individual demand of the higher impact and lower impact homes during the system peak time slots, and is assumed to be zero for non-peak time slots.

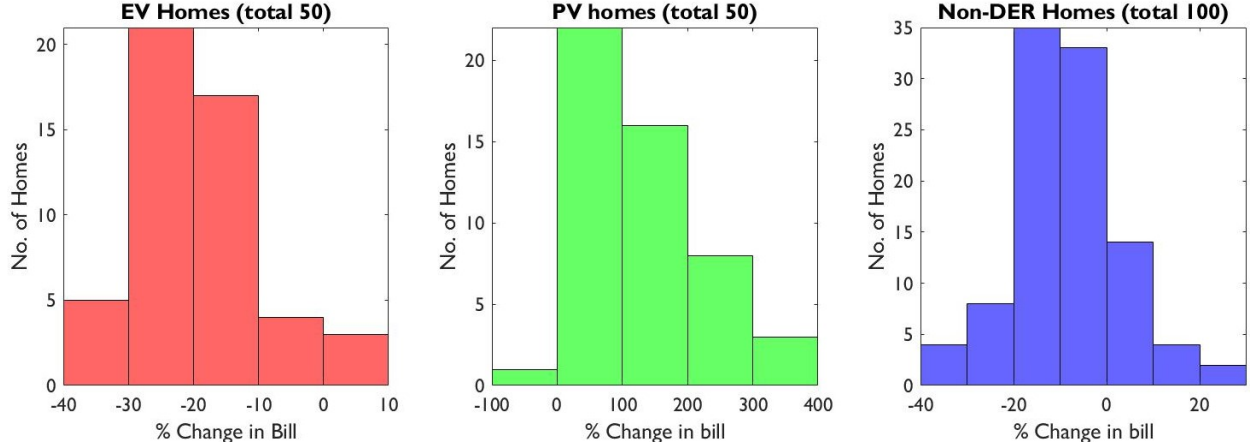


Figure 3.4: Comparison of Proposed and Existing Billing Mechanism for Homes

Despite having a few spikes of demand, the demand of Home 1 during the peak time slots is, for the most part, less than that of Home 2. Furthermore, Home 2 has a negative demand for several time periods each day i.e. it is generating more power than it consumes, indicating that it is a solar PV home. The fact that this home is a higher impact home can be explained by the benefit given to solar PV homes in the current scheme due to net metering. In the proposed scheme, such demand variability is penalized through the V parameter.

3.3.2 Comparing the Current and Proposed Billing Mechanisms

Fig. 3.4 describes the effect of the proposed billing mechanism for each subset of homes. This effect is quantified by evaluating the **percentage change** between the proposed bill and the current bill, i.e. $B_{i \text{ total}}^{\text{new}} - B_{i \text{ total}}^{\text{old}}$ for each home. The distribution of this range has been plotted, categorized based on the type of home: EV Homes, PV Homes, and non-DER Homes.

In the case of EV homes, most homes have a negative % change of $B_{i \text{ total}}^{\text{new}} - B_{i \text{ total}}^{\text{old}}$. This means that almost all homes have a lower TDU Charge in the proposed mechanism than they do in the current mechanism. As a result, it seems that the proposed billing mechanism is favorable for EVs. This follows intuition, because in the current billing mechanism, all that matters for billing is how much kWh volume is consumed by the home. Whereas in the proposed billing algorithm, the impact of the user is calculated during the peak time slots of demand, where the distribution system is under the most stress. Thus, under the proposed billing mechanism, there is great potential for smart scheduling of EV charging during the non-peak periods, which could lead to significant savings for those homes. As a result, the interests of both the TDU and the user are aligned.

When we observe the trend for PV homes, most homes have a positive % change $B_{i \text{ total}}^{\text{new}} - B_{i \text{ total}}^{\text{old}}$ means that almost all PV homes have a significant increase in their TDU Charge when evaluated under the proposed mechanism. While this observation seems to suggest that the proposed mechanism is unfavorable to PV homes, it can be argued that the proposed mechanism is capturing the true costs of PV that were previously (unfairly) being borne by non-PV homes.

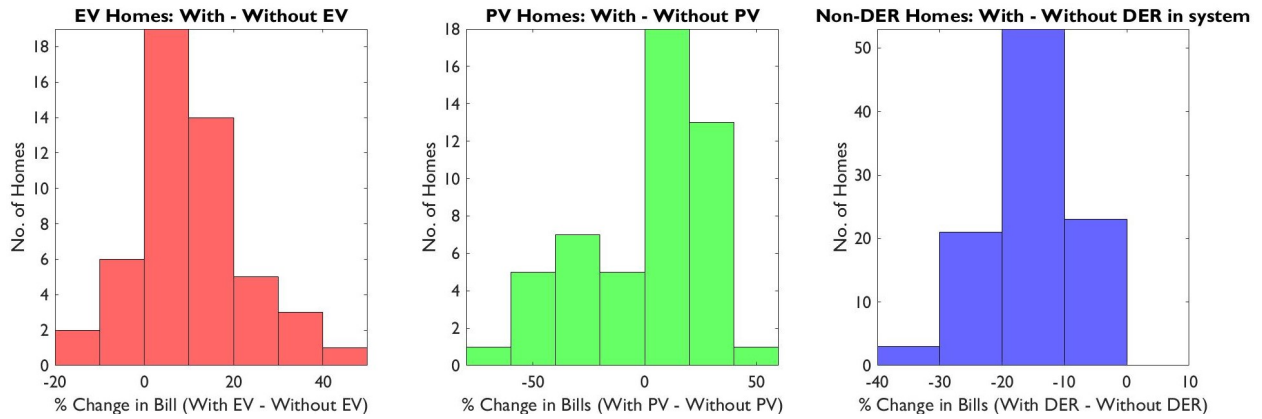


Figure 3.5: % Change in TDU Charges before and after 25% DER Penetration (Calculated under the Proposed Mechanism)

Despite the fact that the kWh volume of consumption for PV homes is less, the sudden ramping of PV during the late evening causes significant strain on the distribution grid. This aspect is captured in the new billing scheme through the Variability impact factor V .

Let us now consider the case of non-DER homes. Most homes have a negative percentage change value for $B_{i, total}^{new} - B_{i, total}^{old}$. More specifically, of the 100 non-DER homes, over 80 have a negative $B_{i, total}^{new} - B_{i, total}^{old}$, with almost 70 homes having a slightly negative change (0-20% reduction in bill). This indicates that most non-DER homes are being benefited by the proposed billing mechanism. This addresses one of the key drawbacks of the existing billing scheme, where in many cases, costs incurred by the TDUs in their PV-incentive programs such as net metering or other subsidies would be recovered from the non-PV customers via increase in the fixed charges. With the proposed mechanism, the trend of penalizing non-PV customers is reversed, bringing the distribution of TDU Charges back to balance.

3.3.3 The Effect of DER Penetration on TDU Charges Calculated under the Proposed Mechanism

Fig. 3.5 describes the effect of penetration of individual DERs (EV and PV) on each subset of homes. In the default system, there is a DER penetration of 25% EV and 25% PV (50 homes each). In the system without EV, the DER penetration is 0% EV (0 homes) and 25% PV (50 homes). Similarly in the system without PV, the DER penetration is 25% EV (50 EV homes) and 0% PV (0 PV Homes). In the system without DERs, the DER penetration is 0%, i.e. 0% EV and 0% PV. The left figure compares the TDU Charges of the EV Homes calculated in the default system vs the system without EVs. The middle figure compares TDU Charges of PV homes calculated in the default system vs the system without PV generation. The right figure shows the effect on TDU Charges of non-DER homes due to DER penetration in the system, by comparing the TDU Charges calculated in the default system vs the system with 0% DER penetration.

When considering the effect of EV penetration on EV homes, it is observed that most homes have a positive % change between with and without EV cases, thus following the expected trend of having higher electricity bills due to the presence of an EV.

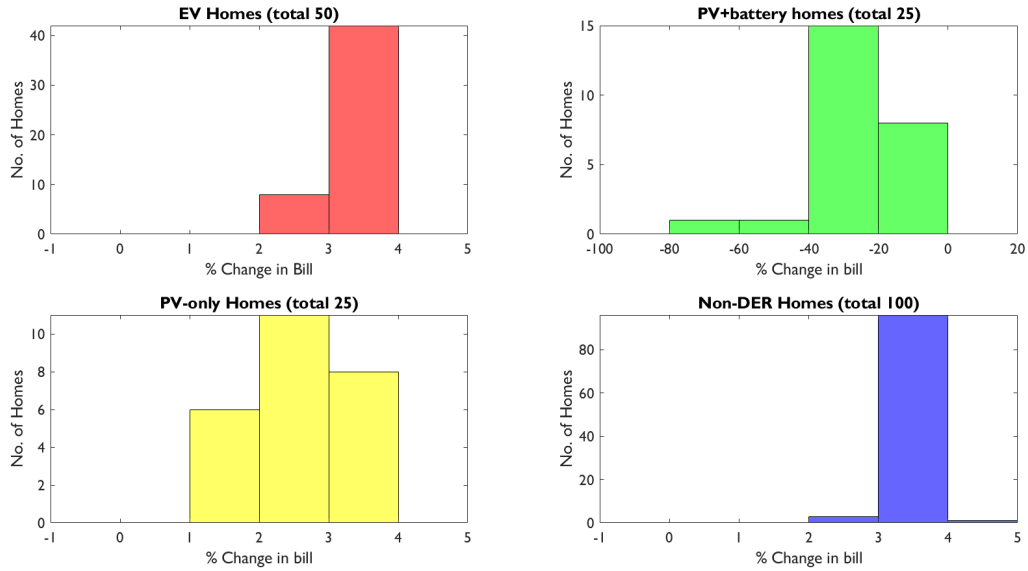


Figure 3.6: % Change in TDU Charges (New Mechanism) after introducing Battery Storage in 25 PV Homes

With PV however, the story is different. Some PV homes seem to benefit with the introduction of PV (around 30 homes), but the rest have a higher TDU Charge with the introduction of PV. One factor could be explained by the variability index V accounting for 25% of the total revenue, and that the PV homes have the highest variability impact factors. Another issue could be that PVs are pulling down the system conditions below peak threshold when the sun is shining, and shifting peak slots to different times. This leads to a very interesting thought: the application of solar + storage technology combined with smart scheduling for maximizing usage during system non-peak conditions could be the optimal strategy in the proposed billing scheme. This has been explored in the case study discussed in Section 3.3.4.

Looking at the effect of DER penetration on non-DER homes, it is noted that every single non-DER home has seen a reduction in their TDU Charges due to the penetration of DER. While this seems like the proposed mechanism rewards customers for not investing in DER, it is more accurate to view this as evidence that a fair cost recovery from DER homes is happening because of DER homes having an increase in their grid impact, due to the penetration of DERs.

3.3.4 Effect of Battery Storage on TDU Charges calculated under the Proposed Mechanism

Fig. 3.6 shows the effect of penetration of battery storage in the system on the TDU Charges calculated under the proposed rate mechanism. In this case study, half of the PV homes (25 out of 50) are given a battery storage unit, that operates under a brute force algorithm, charging during non-peak hours (1AM - 3AM), and discharging during typical peak hours (5PM - 7PM), with a rate of 2 kW for both charge and discharge cycles. Essentially, this is meant to reduce impact on grid by discharging during peak time slots, and charging during non-peak time slots.

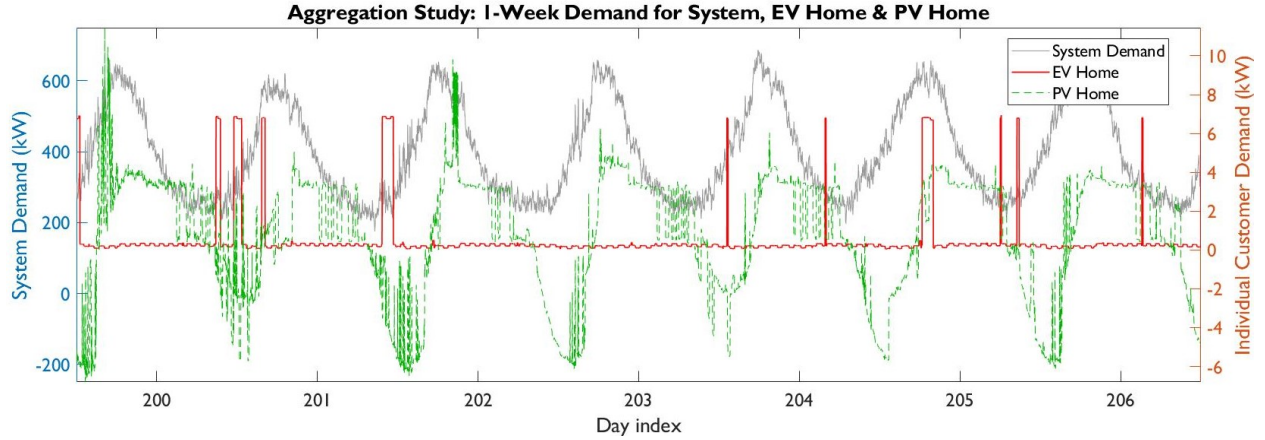


Figure 3.7: Case Study: Aggregating a low- V_i EV customer and a high- V_i PV customer

Fig. 3.6 (top-right) shows that every single 'PV+battery' home has experienced a reduction in TDU Charge due to the introduction of battery storage. This reduction has been observed despite the fact that a brute force charging-discharging schedule was implemented. This result could be further improved if the battery storage devices are operated under a smart-scheduling algorithm, that not only reduces impact during peak time slots, but also counteracts spikes in variability of the system, thus earning rewards for positive contributions to grid conditions.

The other 3 sub-figures in Fig. 3.6 show the effects of the introduction of battery systems in 25 PV homes on the other categories of homes. Homes in all of these categories see minor increases in their bills, so it could be argued that the proposed mechanism provides the most rewards for customers having PV + battery storage, who are more likely to be richer customers, at the expense of non-DER customers, who may be less affluent and cannot afford PVs and battery storage. However, when comparing the TDU Charges of these non-DER customers under the proposed and current schemes, it is clear that these homes will still be better off than they are under the current scheme.

3.3.5 Effect of Customer Aggregation on TDU Charges calculated under the Proposed Mechanism

Consider the case of customer aggregation, where a group of customers come together to form an aggregated customer group, which is essentially treated as a singular customer entity by the TDU. It is desirable for customers within this group to complement each other's variability V_i^t such that there is a reduction in the net variability impact of the aggregated customer group. If net variability impact of a group reduces, the total impact on the system reduces. Such aggregated customer groups could potentially be governed by an internal smart control algorithm such that the group minimizes their net impact on the system. A good billing mechanism should reflect rewards for such desirable reduction in system impact.

In the existing billing mechanism, there would be no change in the total TDU Charge of

these aggregated customers, since the total kWh consumption remains the same. However, the proposed mechanism considers variability of power demand as a key parameter for evaluating the impact of customers. Thus, such aggregated customer groups will have a net reduction in aggregate customer bill, compared to the sum of TDU Charges of the same customers treated as individuals.

Fig 3.7 is a case study performed with two customers to illustrate the effect of aggregation on TDU Charges calculated in the proposed mechanism. Here, a low- V_i EV customer is aggregated with a high- V_i PV customer. No smart control algorithm has been implemented to change the behavior of either customer; this case study is conducted to illustrate the potential of customer aggregation for TDU Charge reduction. Fig 3.7 shows the demand of the System, EV customer, and PV customer over one week. Clearly, these homes oppose each other's variability quite regularly, especially when the the EV customer's EV is charging and the PV customer's solar panel is generating power.(note the multiple 6.6 kW spikes seen in the EV customer's demand curve, and the intermittent spiking of the PV customer's demand curve). We expect a net reduction in variability impact when these customers are aggregated, thus resulting in a lower TDU Charge for the aggregated customer group compared to the sum of the two individual bills. The results of this case study are shown in Table 3.1.

It is clearly observed that customer aggregation can have the desirable effect of further incentivizing variability impact reductions, which can be harnessed by smart control algorithms governing the behavior of customers within such aggregated customer groups.

Evaluation Metric	Individual Customers		If same customers were Aggregated
	PV Customer	EV Customer	
% Share of Variability Impact using Normalized Correlation	2.11%	0.27%	1.85%
Total Bill over full 2-year period (\$)	\$1913	\$622	\$2234
	Total = \$2535		\$301 (11.87%) saved through aggregation

Table 3.1: Case Study: Comparing Impact and Total TDU Charges before and after Aggregation

3.3.6 Pros and Cons of the Proposed Mechanism

Pros

Revenue Decoupling The mechanism introduced in this work effectively decouples utility revenue and customer bills from volumetric consumption. This is important to the long-term stability of utility revenues, since due to the growing penetration of DERs, volumetric charge based revenue could decline in the future.

Recovers Utility Costs Accurately and Effectively The proposed mechanism is more representative of the true costs inflicted upon the distribution grid by the customers, due to the usage of kW rather than kWh as a defining metric. The major driver for investment costs in equipment is the consumer demand during peak periods. Thus, the proposed approach provides better alignment between the revenue and costs as compared to the volumetric charge. The introduction of 'Variability' is also a novel approach. The variable nature of renewable resources adversely impacts the efficient operation of the grid and as such should be accounted for in the cost recovery mechanism.

Utility Revenue Targets are Assured to Be Met There is a key and prominent distinction between the proposed mechanism and the current model - rather than expecting a total revenue for the TDU depending on several variables, the proposed mechanism offers the TDU the opportunity to ensure a stable and assured revenue. This is because the total target revenue is first set, and then the proposed mechanism allocates the costs to all customers appropriately. Another advantage is that this form of rate-making could require less frequent rate cases, which is a time-consuming and expensive process.

Reduces Unfair Cross-Subsidy Both the current volumetric charge and the net-metering policies result in TDUs over-recovering costs from non-PV customers while under-recovering them from PV customers. Further, there is a high likelihood that non-PV customers fall in the low-income category, while PV customer fall in the high-income category. Thus the proposed mechanism mitigates against the existing unfair and regressive cross-subsidy. Further, the proposed approach is consistent for all types of DERs. This is important to incentivize technologies such as energy storage.

Retains Efficiency Incentive Under the current volumetric mechanism increasing efficiency reduces electricity sales and therefore profits [100]. The proposed billing mechanism retains the incentive for the TDU to be efficient. Since the total revenue target is controlled under this structure, the TDU is incentivized to take action to improve system efficiency so as to get higher profits. Regulators could also include explicit performance bonuses for TDUs improving their efficiency.

Rewards Smart Customer Aggregation As illustrated in Section 3.3.5 and Fig 3.7, aggregation could potentially lower TDU Charges for those customers who form sub-groups that have lower aggregate variability. Apart from potentially, this also opens up a whole new market for the Electricity Service of Customer Aggregation. Providers of Customer Aggregation could run local energy markets, create Demand Response based incentive programs, and perform smart automatic control of their customer groups to minimize group impact, thus resulting in a reduced TDU Charge for that sub-group compared to the sum of their TDU Charges if they remained discrete customers.

Cons

Peak Threshold Calculation Unfair to Solar PV? As mentioned earlier, the introduction of PV could cause the total system demand to go below the peak threshold in some time slots, thus converting those time slots from peak slots to non-peak slots. However, this also shifts the peak slots to a different time, because of the fact that peak slots are defined on a percentile basis, rather than absolute. There will always be a top $x\%$ set of values; it does not matter whether that range is small or large. As a result, the new system peak time slots would be those times when perhaps the sun does not shine. The appliance usage of a PV home is not offset when the sun is not shining, therefore these new shifted peak slots could be when the PV homes stop generating, and demand power from the grid, thus contributing to increase in the system demand. These slots are now the peak slots, and PV homes along with all other homes contribute to their W and V impact factors significantly during this time. Thus, it could lead to the situation where non-PV homes get away with 'bad' usage patterns when the sun is shining, because PV homes are generating enough power to reduce the stress on the system below the system peak threshold. Essentially, some non-PV homes escape penalization due to their behavior being covered or compensated for by the PV homes.

This problem could be easily dealt with when rolling out the proposed mechanism in practice: peak thresholds could potentially be selected by TDUs based on distribution feeder capacity, for the feeders on which this algorithm is being implemented. This would make the thresholds absolute, rather than relative.

Solar PV ancillary benefits It could be argued that Solar PV is not being rewarded for the various benefits it brings to the grid or indeed its societal benefit in terms of reducing pollution. Distributed PV systems likely provide ancillary benefits such as reducing distribution system losses by generating close to the point of consumption, and in the future also might offer frequency and voltage support services through the use of smart inverters [101].

Rate simplicity Clarity and simplicity is a consideration for rate design. In this respect the volumetric rate has an advantage since customers have become accustomed to it. On the other hand it could be argued that customers are also familiar with the concept of credit scores, and being subject to different interest rates relative to other customers, based on their individual risk to the lender.

3.3.7 Policy Implications

The current volumetric rate structure has some clear drawbacks, the first being that the TDU is not assured of sufficient revenues, and the second that there is effectively an unfair cross-subsidy from non-PV customers to PV customers. Since with declining revenues the TDU would be forced to raise the rates for everyone. The proposed approach provides long-term stability to the TDU. PV customers could face higher bills, but this could be considered appropriate given that the energy they contribute may not be coincident with peak demand, which is a large driver of distribution system costs. Moreover, if such customers also had optimally operating storage, their TDU Charges could be reduced.

With the introduction of metrics such as peak thresholds and % Allocation, the TDU has far greater flexibility to modify the billing mechanism based on the true costs they incur, customized for their system conditions.

Regulators should be careful not to favor a particular technology and rate designs should be based on the true value of energy provided by DER assets.

4. Concluding Remarks

With the increasing penetration of DER technologies, utilities are likely to face challenges associated with the current volumetric rate design. Regulators should consider alternative rate designs that are better aligned with the cost-causation principle.

This paper introduces an algorithm to calculate a fixed, customer-specific grid access fee, based on metrics that contribute directly to the true costs incurred by the TDU in providing electric power to their customers. As a result, the volumetric throughput incentive is eliminated, thus aligning the interests of both the TDU as well as the end-users towards a future distribution grid with higher DER penetration. This has been accomplished through a shift in philosophy, from treating electricity as a commodity to Electricity as a Service.

Future work will investigate some key questions: further insight needs to be gained on how to calculate the actual Total Target Revenue, such that it recovers the costs incurred by utilities under different system conditions. The effect of smart-scheduling algorithms that respond to real-time signals of system performance needs to be tested. Applying this on the aggregation of solar and storage could be transformative, and thus needs to be explored. Further, the proposed rate structure incentivizes customer aggregation, where groups of customers form such that these customers' consumption patterns are negatively correlated with each other. This could reduce the group impact on the grid, thus reducing their TDU Charge as part of a group, compared to their TDU Charge when considered as individual customers. Smart scheduling and real-time adaptive consumption patterns could be leveraged in such aggregation mechanisms to negate the spikes of other customers in the group.

References

- [1] J. Zhu, M.-Y. Chow, and F. Zhang, "Phase balancing using mixed-integer programming [distribution feeders]," *IEEE transactions on power systems*, vol. 13, no. 4, pp. 1487–1492, 1998.
- [2] L. F. Ochoa, R. M. Ciric, A. Padilha-Feltrin, and G. P. Harrison, "Evaluation of distribution system losses due to load unbalance," in *15th PSCC*, vol. 6, 2005, pp. 1–4.
- [3] T.-H. Chen and J.-T. Cherng, "Optimal phase arrangement of distribution transformers connected to a primary feeder for system unbalance improvement and loss reduction using a genetic algorithm," in *Power Industry Computer Applications, 1999. PICA'99. Proceedings of the 21st 1999 IEEE International Conference*. IEEE, 1999.
- [4] K. Ma, R. Li, and F. Li, "Quantification of additional asset reinforcement cost from 3-phase imbalance," *IEEE Transactions on Power Systems*, vol. 31, no. 4, pp. 2885–2891, 2016.
- [5] R. Yan and T. K. Saha, "Investigation of voltage imbalance due to distribution network unbalanced line configurations and load levels," *IEEE Transactions on Power Systems*, vol. 28, no. 2, pp. 1829–1838, 2013.
- [6] F. Shahnia, P. J. Wolfs, and A. Ghosh, "Voltage unbalance reduction in low voltage feeders by dynamic switching of residential customers among three phases," *IEEE Transactions on Smart Grid*, vol. 5, no. 3, pp. 1318–1327, 2014.
- [7] M. S. Modarresi, T. Huang, H. Ming, and L. Xie, "Robust phase detection in distribution systems," in *Power and Energy Conference (TPEC), IEEE Texas*. IEEE, 2017, pp. 1–5.
- [8] H. Xu, A. D. Domínguez-García, and P. W. Sauer, "A data-driven voltage control framework for power distribution systems," in *In Proceedings of 2018 Power and Energy Society General Meeting (PESGM)*. IEEE, 2018.
- [9] X. Geng, L. Xie, and D. Obadina, "Voltage Security Constrained Look-ahead Coordination of Reactive Power Support Devices with High Renewables," in *Proceedings of the 19th International Conference on Intelligent System Applications to Power Systems*, 2017.
- [10] Xinbo Geng, Le Xie, and Diran Obadina, "Chance-constrained Optimal Reactive Power Dispatch," in *In Proceedings of 2018 Power and Energy Society General Meeting (PESGM)*. IEEE, 2018.
- [11] A. Khodabakhsh, G. Yang, S. Basu, E. Nikolova, M. C. Caramanis, T. Lianeas, and E. Pountourakis, "A Submodular Approach for Electricity Distribution Network Reconfiguration," in *Proceedings of the 36th Annual Hawaii International Conference on System Sciences, 2017*, 2017.
- [12] S. Civanlar, J. Grainger, H. Yin, and S. Lee, "Distribution feeder reconfiguration for loss reduction," *IEEE Transactions on Power Delivery*, vol. 3, no. 3, pp. 1217–1223, 1988.

- [13] J. Zhu, G. Bilbro, and M.-Y. Chow, "Phase balancing using simulated annealing," *IEEE Transactions on Power Systems*, vol. 14, no. 4, pp. 1508–1513, 1999.
- [14] C.-H. Lin, C.-S. Chen, H.-J. Chuang, M.-Y. Huang, and C.-W. Huang, "An expert system for three-phase balancing of distribution feeders," *IEEE Transactions on Power Systems*, vol. 23, no. 3, pp. 1488–1496, 2008.
- [15] R. A. Hooshmand and S. Soltani, "Fuzzy optimal phase balancing of radial and meshed distribution networks using BF-PSO algorithm," *IEEE Transactions on Power Systems*, vol. 27, no. 1, pp. 47–57, 2012.
- [16] C. Lin, C. Chen, M. Huang, H. Chuang, M. Kang, C. Ho, and C. Huang, "Optimal phase arrangement of distribution feeders using immune algorithm," in *Intelligent Systems Applications to Power Systems, 2007. ISAP 2007. International Conference on*. IEEE, 2007, pp. 1–6.
- [17] K. Wang, S. Skiena, and T. G. Robertazzi, "Phase balancing algorithms," *Electric Power Systems Research*, vol. 96, pp. 218–224, 2013.
- [18] M. Dilek, R. P. Broadwater, J. C. Thompson, and R. Seqiun, "Simultaneous phase balancing at substations and switches with time-varying load patterns," *IEEE Transactions on Power Systems*, vol. 16, no. 4, pp. 922–928, 2001.
- [19] C.-H. Lin, C.-S. Chen, H.-J. Chuang, and C.-Y. Ho, "Heuristic rule-based phase balancing of distribution systems by considering customer load patterns," *IEEE Transactions on Power Systems*, vol. 20, no. 2, pp. 709–716, 2005.
- [20] J. R. Birge and F. Louveaux, *Introduction to stochastic programming*. Springer Science & Business Media.
- [21] D. Bertsimas and M. Sim, "The price of robustness," *Operations research*, vol. 52, no. 1, pp. 35–53, 2004.
- [22] C. Bandi and D. Bertsimas, "Tractable stochastic analysis in high dimensions via robust optimization," *Mathematical programming*, 2012.
- [23] A. Ben-Tal, L. El Ghaoui, and A. Nemirovski, *Robust optimization*. Princeton University Press, 2009.
- [24] D. Bertsimas, D. B. Brown, and C. Caramanis, "Theory and applications of robust optimization," *SIAM review*, vol. 53, no. 3, pp. 464–501, 2011.
- [25] A. Ben-Tal, L. El Ghaoui, and A. Nemirovski, *Robust optimization*. Princeton University Press, 2009.
- [26] A. A. Thatte, X. A. Sun, and L. Xie, "Robust optimization based economic dispatch for managing system ramp requirement," in *System Sciences (HICSS), 2014 47th Hawaii International Conference on*. IEEE, 2014, pp. 2344–2352.

- [27] L. Xie, Y. Gu, X. Zhu, and M. G. Genton, “Short-term spatio-temporal wind power forecast in robust look-ahead power system dispatch,” *IEEE Transactions on Smart Grid*, vol. 5, no. 1, pp. 511–520, 2014.
- [28] I. Gurobi Optimization, *Gurobi Optimizer Reference Manual*, 2016. [Online]. Available: <http://www.gurobi.com>
- [29] S. Sun, B. Liang, M. Dong, and J. A. Taylor, “Phase balancing using energy storage in power grids under uncertainty,” *IEEE Transactions on Power Systems*, vol. 31, no. 5, pp. 3891–3903, 2016.
- [30] A. Hoke, R. Butler, J. Hambrick, and B. Kroposki, “Steady-state analysis of maximum photo-voltaic penetration levels on typical distribution feeders,” *IEEE Transactions on Sustainable Energy*, vol. 4, no. 2, pp. 350–357, 2013.
- [31] K. P. Schneider, Y. Chen, D. P. Chassin, R. G. Pratt, D. W. Engel, and S. E. Thompson, “Modern grid initiative distribution taxonomy final report,” Pacific Northwest National Laboratory (PNNL), Richland, WA (US), Tech. Rep., 2008.
- [32] J. Löfberg, “Automatic robust convex programming,” *Optimization methods and software*, 2012.
- [33] —, “YALMIP : A Toolbox for Modeling and Optimization in MATLAB,” in *In Proceedings of the CACSD Conference*, Taipei, Taiwan, 2004.
- [34] A. Ben-Tal and A. Nemirovski, “Robust solutions of uncertain linear programs,” *Operations research letters*, vol. 25, no. 1, pp. 1–13, 1999.
- [35] D. Bertsimas and M. Sim, “Robust discrete optimization and network flows,” *Mathematical programming*, vol. 98, no. 1-3, pp. 49–71, 2003.
- [36] D. Bertsimas, V. Gupta, and N. Kallus, “Data-driven robust optimization,” *Mathematical Programming*, 2018.
- [37] J. K. Lenstra, D. B. Shmoys, and E. Tardos, “Approximation algorithms for scheduling unrelated parallel machines,” *Mathematical programming*, vol. 46, no. 1-3, pp. 259–271, 1990.
- [38] S. Sahni and T. Gonzalez, “P-complete approximation problems,” *Journal of the ACM (JACM)*, 1976.
- [39] H. Xu, A. D. Domínguez-García, and P. W. Sauer, “Adaptive coordination of distributed energy resources in lossy power distribution systems,” *arXiv preprint arXiv:1711.04157*, 2017.
- [40] H. Xu, A. D. Domínguez-García, and P. W. Sauer, “Adaptive coordination of distributed energy resources in lossy power distribution systems,” in *In Proceedings of 2018 Power and Energy Society General Meeting*. Portland, OR: IEEE, 2018.

- [41] H. Zhang, Z. Hu, E. Munsing, S. J. Moura, and Y. Song, “Data-driven chance-constrained regulation capacity offering for distributed energy resources,” *IEEE Transactions on Smart Grid*, 2018.
- [42] H. Zhang, Z. Hu, Z. Xu, and Y. Song, “Evaluation of achievable vehicle-to-grid capacity using aggregate pev model,” *IEEE Transactions on Power Systems*, vol. 32, no. 1, pp. 784–794, 2017.
- [43] H. Zhang, S. J. Moura, Z. Hu, W. Qi, and Y. Song, “Joint pev charging network and distributed pv generation planning based on accelerated generalized benders decomposition,” *IEEE Transactions on Transportation Electrification*, 2018.
- [44] X. Chen, H. Zhang, Z. Xu, C. P. Nielsen, M. B. McElroy, and J. Lv, “Impacts of fleet types and charging modes for electric vehicles on emissions under different penetrations of wind power,” *Nature Energy*, 2018.
- [45] C. J. Bennett, R. A. Stewart, and J. W. Lu, “Development of a three-phase battery energy storage scheduling and operation system for low voltage distribution networks,” *Applied Energy*, vol. 146, pp. 122–134, 2015.
- [46] B. Xu, Y. Shi, D. S. Kirschen, and B. Zhang, “Optimal battery participation in frequency regulation markets,” *IEEE Transactions on Power Systems*, 2018.
- [47] B. Xu, J. Zhao, T. Zheng, E. Litvinov, and D. S. Kirschen, “Factoring the cycle aging cost of batteries participating in electricity markets,” *IEEE Transactions on Power Systems*, vol. 33, no. 2, pp. 2248–2259, 2018.
- [48] A. Haider, X. Geng, G. Sharma, L. Xie, and P. Kumar, “A control system framework for privacy preserving demand response of thermal inertial loads,” in *2015 IEEE International Conference on Smart Grid Communications (SmartGridComm)*. IEEE, 2015, pp. 181–186.
- [49] A. Halder, X. Geng, P. Kumar, and L. Xie, “Architecture and Algorithms for Privacy Pre-serving Thermal Inertial Load Management by A Load Serving Entity,” *IEEE Transactions on Power Systems*, 2016.
- [50] B. Xia, H. Ming, K.-Y. Lee, Y. Li, Y. Zhou, S. Bansal, S. Shakkottai, and L. Xie, “Energy-coupon: A case study on incentive-based demand response in smart grid,” in *Proceedings of the Eighth International Conference on Future Energy Systems*. ACM, 2017, pp. 80–90.
- [51] Hao Ming, Le Xie, Marco Campi, Simone Garatti, and P.R. Kumar, “Scenario-based Economic Dispatch with Uncertain Demand Response,” *accepted by IEEE Transactions on Smart Grid*, 2017.
- [52] F. Dong, B. H. Chowdhury, M. L. Crow, and L. Acar, “Improving voltage stability by reactive power reserve management,” *IEEE transactions on Power Systems*, vol. 20, no. 1, pp. 338–345, 2005.

- [53] W. D. Rosehart, C. A. Canizares, and V. H. Quintana, “Multiobjective optimal power flows to evaluate voltage security costs in power networks,” *IEEE Transactions on power systems*, 2003.
- [54] X. Wang, G. Ejebe, J. Tong, and J. Waight, “Preventive/corrective control for voltage stability using direct interior point method,” *IEEE Transactions on Power Systems*, vol. 13, no. 3, pp. 878–883, 1998.
- [55] A. Rabiee and M. Parniani, “Voltage security constrained multi-period optimal reactive power flow using benders and optimality condition decompositions,” *IEEE Transactions on Power Systems*, 2013.
- [56] G. C. Calafiore and M. C. Campi, “The scenario approach to robust control design,” *IEEE Transactions on automatic control*, vol. 51, no. 5, pp. 742–753, 2006.
- [57] L. Khachiyan, “The problem of calculating the volume of a polyhedron is enumerably hard,” *Russian Mathematical Surveys*, 1989.
- [58] A. Charnes and W. W. Cooper, “Deterministic equivalents for optimizing and satisficing under chance constraints,” *Operations research*, 1963.
- [59] A. Prékopa, *Stochastic programming*. Springer Science & Business Media, 2013, vol. 324.
- [60] D. R. Morgan, J. W. Eheart, and A. J. Valocchi, “Aquifer remediation design under uncertainty using a new chance constrained programming technique,” *Water resources research*, vol. 29, no. 3, pp. 551–561, 1993.
- [61] M. W. Tanner and L. Ntaimo, “IIS branch-and-cut for joint chance-constrained stochastic programs and application to optimal vaccine allocation,” *European Journal of Operational Research*, 2010.
- [62] B. Zeng, Y. An, and L. Kuznia, “Chance constrained mixed integer program: Bilinear and linear formulations, and Benders decomposition,” *Mathematical Programming*, 2017.
- [63] D. Bienstock, M. Chertkov, and S. Harnett, “Chance-constrained optimal power flow: Risk-aware network control under uncertainty,” *SIAM Review*, vol. 56, no. 3, pp. 461–495, 2014.
- [64] M. Vrakopoulou, J. L. Mathieu, and G. Andersson, “Stochastic optimal power flow with uncertain reserves from demand response,” in *Hawaii International Conference on System Sciences (HICSS)*, 2014.
- [65] M. S. Modarresi, L. Xie, and C. Singh, “Reserves from Controllable Swimming Pool Pumps: Reliability Assessment and Operational Planning,” in *Hawaii International Conference on System Sciences (HICSS)*, 2018.
- [66] M. S. Modarresi, L. Xie, A. A. Thatte, M. C. Campi, S. Garatti, and P. Kumar, “Scenario-based Economic Dispatch with Adaptable Level of Risk: Theory and Case Studies,” *invited to be submitted in IEEE Transactions on Power Systems*, 2018.

- [67] T. Summers, J. Warrington, M. Morari, and J. Lygeros, “Stochastic optimal power flow based on convex approximations of chance constraints,” in *Power Systems Computation Conference (PSCC)*. IEEE, 2014.
- [68] R. Fernández-Blanco, Y. Dvorkin, and M. A. Ortega-Vazquez, “Probabilistic security-constrained unit commitment with generation and transmission contingencies,” *IEEE Transactions on Power Systems*, 2017.
- [69] Y. Zhang, J. Wang, B. Zeng, and Z. Hu, “Chance-Constrained Two-Stage Unit Commitment under Uncertain Load and Wind Power Output Using Bilinear Benders Decomposition,” *IEEE Trans on Power Systems*, 2017.
- [70] M. Vrakopoulou, K. Margellos, J. Lygeros, and G. Andersson, “A probabilistic framework for reserve scheduling and security assessment of systems with high wind power penetration,” *IEEE Transactions on Power Systems*, vol. 28, no. 4, pp. 3885–3896, 2013.
- [71] Z. Hu, X. Wang, and G. Taylor, “Stochastic optimal reactive power dispatch: Formulation and solution method,” *International Journal of Electrical Power & Energy Systems*, 2010.
- [72] O. Obadina and G. Berg, “Var planning for power system security,” *IEEE Transactions on Power Systems*, 1989.
- [73] R. Fu, D. J. Feldman, and R. M. Margolis, “Us solar photovoltaic system cost benchmark: Q1 2018,” National Renewable Energy Lab.(NREL), Golden, CO (United States), Tech. Rep., 2018.
- [74] P. Maloney, “How behind-the-meter storage could make up 50%of the u.s. market by 2021,” 2019, <https://www.utilitydive.com/news/how-behind-the-meter-storage-could-make-up-50-of-the-us-market-by-2021/434882/>.
- [75] D. J. Hostick, D. B. Belzer, S. W. Hadley, T. Markel, C. Marnay, and M. C. W. Kintner-Meyer, “Projecting electricity demand in 2050,” Pacific Northwest National Lab (PNNL), Richland, WA (United States), Tech. Rep., 2014.
- [76] U.S. Energy Information Administration (EIA), *Annual Energy Outlook*, 2019, <https://www.eia.gov/outlooks/aeo/>.
- [77] P. IEA, “Global ev outlook 2019,” 2019, www.iea.org/publications/reports/globalevoutlook2019/.
- [78] K. Kotilainen, *Energy Prosumers’ Role in the Sustainable Energy System*. Cham: Springer International Publishing, 2019, pp. 1–14. [Online]. Available: https://doi.org/10.1007/978-3-319-71057-0_11-1
- [79] Pennsylvania State University: College of Earth and Mineral Sciences, “Introduction to electricity markets,” Class notes, 2020. [Online]. Available: <https://www.e-education.psu.edu/ebf483/node/624>

- [80] A. Faruqui, W. Davis, J. Duh, and C. Warner, “Curating the future of rate design for residential customers,” *Electricity Policy*, July 2016, pp. 1–25, 2016.
- [81] B. Houghton, J. Salovaara, and H. Tai, *Solving the rate puzzle: The future of electricity rate design*, 2019, <https://www.mckinsey.com/industries/electric-power-and-natural-gas/our-insights/solving-the-rate-puzzle-the-future-of-electricity-rate-design>.
- [82] A. J. Lawson, “Net metering: In brief,” Congressional Research Service, Tech. Rep. R46010, Nov. 2019.
- [83] K. W. Costello, “Major challenges of distributed generation for state utility regulators,” *The Electricity Journal*, vol. 28, no. 3, pp. 8–25, 2015.
- [84] S. Woodhouse and S. Bradbury, “Chapter 2 - innovation, disruption, and the survival of the fittest,” in *Innovation and Disruption at the Grid’s Edge*, F. P. Sioshansi, Ed. Academic Press, 2017, pp. 25 – 39. [Online]. Available: <http://www.sciencedirect.com/science/article/pii/B9780128117583000024>
- [85] R. Smith and I. MacGill, “Chapter 3 - the great rebalancing: Rattling the electricity value chain from behind the meter,” in *Innovation and Disruption at the Grid’s Edge*, F. P. Sioshansi, Ed. Academic Press, 2017, pp. 41 – 64. [Online]. Available: <http://www.sciencedirect.com/science/article/pii/B9780128117583000036>
- [86] J. Baak, “Chapter 9 - bringing der into the mainstream: Regulations, innovation, and disruption on the grid’s edge,” in *Innovation and Disruption at the Grid’s Edge*, F. P. Sioshansi, Ed. Academic Press, 2017, pp. 167 – 186. [Online]. Available: <http://www.sciencedirect.com/science/article/pii/B9780128117583000097>
- [87] E. Álvarez Pelegry, “Chapter 7 - regulations, barriers, and opportunities to the growth of ders in the spanish power sector,” in *Innovation and Disruption at the Grid’s Edge*, F. P. Sioshansi, Ed. Academic Press, 2017, pp. 123 – 146. [Online]. Available: <http://www.sciencedirect.com/science/article/pii/B9780128117583000073>
- [88] C. W. Gellings, “Chapter 11 - we don’t need a new business model: “it ain’t broke and it don’t need fixin’,” in *Innovation and Disruption at the Grid’s Edge*, F. P. Sioshansi, Ed. Academic Press, 2017, pp. 207 – 220. [Online]. Available: <http://www.sciencedirect.com/science/article/pii/B9780128117583000115>
- [89] N. D. Laws, B. P. Epps, S. O. Peterson, M. S. Laser, and G. K. Wanjiru, “On the utility death spiral and the impact of utility rate structures on the adoption of residential solar photovoltaics and energy storage,” *Applied energy*, vol. 185, pp. 627–641, 2017.
- [90] N. R. Darghouth, R. H. Wiser, G. Barbose, and A. D. Mills, “Net metering and market feedback loops: Exploring the impact of retail rate design on distributed pv deployment,” *Applied Energy*, vol. 162, pp. 713–722, 2016.
- [91] S. P. Burger and M. Luke, “Business models for distributed energy resources: A review and empirical analysis,” *Energy Policy*, vol. 109, pp. 230 – 248, 2017. [Online]. Available: <http://www.sciencedirect.com/science/article/pii/S030142151730438X>

- [92] L. Bird, C. Davidson, J. McLaren, and J. Miller, “Impact of rate design alternatives on residential solar customer bills. increased fixed charges, minimum bills and demand-based rates,” National Renewable Energy Lab (NREL), Golden, CO (United States), Tech. Rep., 2015.
- [93] B. Baatz, “Rate design matters: The intersection of residential rate design and energy efficiency.” American Council for an Energy-Efficient Economy, 2017.
- [94] L. C. Schwartz, “Rate design: Trends and perspectives,” Presentation, Berkeley Lab, Electricity Markets and Policy Group, Aug. 2016.
- [95] R. L. Revesz and B. Unel, “Managing the future of the electricity grid,” *Harv. Envtl. L. Rev.*, vol. 41, p. 43, 2017.
- [96] R. Hledik, J. Zahniser-Word, and J. Cohen, “Storage-oriented rate design: Stacked benefits or the next death spiral?” *The Electricity Journal*, vol. 31, no. 8, pp. 23–27, 2018.
- [97] A. Bharatkumar, “Distribution network use-of-system charges under high penetration of distributed energy resources,” Master’s thesis, Massachusetts Institute of Technology, Department of Electrical Engineering and Computer Science, 2015.
- [98] FERC Order No 755, ““Frequency Regulation Compensation in the Organized Wholesale Power Markets,” Issued October 20, 2011,” 2011.
- [99] Pecan Street Inc., *Pecan Street Dataport*, 2019, <https://www.pecanstreet.org/dataport/>.
- [100] V. Jensen, “Aligning utility incentives with investment in energy efficiency: A product of the national action plan for energy efficiency,” *ICF International*, 2007.
- [101] F. Ding, A. Nagarajan, S. Chakraborty, M. Baggu, A. Nguyen, S. Walinga, M. McCarty, and F. Bell, “Photovoltaic impact assessment of smart inverter volt-var control on distribution system conservation voltage reduction and power quality,” National Renewable Energy Lab.(NREL), Golden, CO (United States), Tech. Rep., 2016.